The Hong Kong Polytechnic University

Department of Health Technology and Informatics

Development of DICOM-Based Computer-Aided System and Conformity Index for Evaluation of Intensity Modulated Radiation Therapy Plans for Head-and-Neck Cancer

Cheung Wai Kwan, Fion

A thesis submitted in partial fulfillment of the requirements for the

Degree of Doctor of Philosophy

October 2011

CERTIFICATE OF ORIGINALITY

I hereby declare that this thesis is my own work and that, to the best of my knowledge and belief, it reproduces no material previously published or written, nor material that has been accepted for the award of any other degree or diploma, except where due acknowledgement has been made in the text.

_____ (Signed)

CHEUNG WAI KWAN, FION (Name of student)

Abstract of thesis entitled "Development of DICOM-based computer-aided system and conformity index for evaluation of intensity modulated radiation therapy plans for head-and-neck cancer"
submitted by Cheung Wai Kwan, Fion
for the degree of Doctor of Philosophy
at the Hong Kong Polytechnic University in October 2011.

Introduction: Intensity modulated radiation therapy (IMRT) has gained popularity in the treatment of cancers. Due to its complex anatomy, manual evaluation of IMRT plans for head-and-neck cancer has been especially challenging necessitating efficient and objective assessment tools. Thus, the aim of this study was to develop a computer-aided evaluation (CAE) system and a personalized target conformity index (CI) for automatic evaluation of IMRT plans for head-and-neck cancer.

Methodology: The CAE and a personalized target CI were developed based on the four-phase spiral model. Utilizing the MATLAB program language, a set of routines was written to parse key data from the Digital Imaging and Communications in Medicine for radiation therapy (DICOM RT) objects. After data reconstruction, an algorithm for detection of violations was developed to extract the overdose and underdose regions. Thirty IMRT plans for nasopharyngeal carcinoma were collected for evaluation of CAE system performance. Normalized root mean square deviation (NRMSD) was computed for comparison between manually extracted and CAE-extracted data. To assess the plan quality discerning power of the personalized target CI, three computed tomography data sets of nasopharyngeal carcinoma patients were collected. Ten

IMRT plans were generated from each data set. They were ranked and compared with different conformity indices. The coefficient of variance was calculated for each data set to compare the degree of variation from personalized target CI to other existing indices. Mixed-design analysis of variance (ANOVA) was performed to explore the impact of use of CAE system with personalized target CIs on plan evaluation time.

Results: The CAE and a personalized target CI for automatic evaluation of IMRT plans for head-and-neck cancer was developed. Three major graphical user interfaces (GUIs) were created to intelligently lead the planners through the steps of plan evaluation process. The CAE-computed dose volume histogram (DVH) results were in good agreement with the manually extracted data with a NRMSD of less than 0.05%. With the aid of the CAE system, the per-region detection performance for small-size spots was greatly improved by 2.36-fold and 3.99-fold for experienced and inexperienced planners, respectively. Compared with other commonly used indices, the personalized target CIs resulted in the largest coefficient of variance among 10 IMRT plans for each data set, indicating that its discerning power was the best among the indices being compared. The ANOVA results indicated that the evaluation time with the aid of CAE system was significantly shortened by 1.88-fold than that without using the CAE system, regardless of the level of experience.

Conclusion: The CAE system with personalized target CI demonstrated good applicability of DICOM RT objects in data mining. The use of CAE system with personalized target CI could eliminate human errors, provide plan quality control and enhance efficiency in evaluating IMRT plans for head-and-neck cancer. By

taking individual tumor geometry into account, the superiority of personalized target CI in plan discerning power was demonstrated. As an effective data mining tool, the CAE system with personalized target CI could be adopted in the evaluation of treatment plans other than IMRT.

Publications arising from the thesis

1. Cheung, F.W.K. and Law, M.Y.Y. DICOM-based computer-aided evaluation of intensity modulated radiotherapy treatment plans. Proceedings of the SPIE (Society of Photo-Optical Instrumentation Engineers) Medical Imaging Conference 2011 (Vol.7967, p.1-10), 12-17 Feb 2011, Orlando, U.S.A.
2. Cheung, F.W.K., Le, A. and Law, M.Y.Y., DICOM-based electronic patient record system with computer-aided evaluation of intensity modulated radiation therapy plans. 2011 Joint American Association of Physicists in Medicine (AAPM) / Canadian Organization of Medical Physicists (COMP) Meeting, 31 July – 4 August, Vancouver, Canada; Poster Presentation.
3. Cheung, F.W.K. and Law, M.Y.Y., A personalized target conformity index for IMRT plan comparison, ASTRO (American Society for Therapeutic Radiology and Oncology) 53rd Annual Meeting, October 2-6, 2011, Miami, USA; Poster presentation.
4. Le, A. and Cheung, F.W.K., Automatic treatment plan evaluation using a web-based electronic patient record system and a computer-aided evaluation for intensity modulated radiation therapy plans. RSNA (Radiological Society of North America) 2011, 27 November – 2 December 2011; Poster Presentation.
5. Cheung, F.W.K. and Law, M.Y.Y., A novel conformity index for intensity modulated radiation therapy plan evaluation. Medical Physics. (submitted and being revised)

6. Cheung, F.W.K., Law, M.Y.Y. and Fung, C., Development of a mobile cloud computer-aided evaluation system in radiotherapy. 2012 Radiological Society of North America (RSNA) Meeting, 25 November – 30 November, Chicago, USA; Poster presentation. (submitted)

Acknowledgements

First and foremost, I owe my deepest gratitude to my supervisor, Dr. Maria Y.Y. Law for her inspiring guidance, expert advice and inexhaustible patience throughout my study years at the Hong Kong Polytechnic University. Dr. Law is not only an excellent scholar, but also my most respected mentor who selflessly share her broad knowledge, extensive experience and great wisdom with me. It has been an honor being her Ph.D student. Without her untiring encouragement and warm support, this thesis would not have been possible.

A special acknowledgement is forwarded to Prof. Yong-Ping Zheng for his valuable comments and suggestions. My sincere thanks also go to Prof. Bernie H.K. Huang for kindly giving me the opportunity of visiting the Image Processing and Informatics Laboratory of University of Southern California. Professor Huang has impressed me greatly with his boundless energy, enthusiasm and intense dedication to the development of imaging informatics technology. I am immensely grateful to Dr. Brent Liu and Dr. Anh Le for their kind assistance and advice.

Grateful thanks are extended to Dr. Douglas Ng for his generous help and technical consultation. My sincere thanks also go to my family for their irreplaceable love, incessant care and unfailing encouragement through all these years. Besides all, I thank the Almighty God for endowing me with the strength and courage to finish this work.

List of Figures

List of Tables

List of Abbreviations

3DCRT	three-dimensional conformal radiotherapy
AAPM	American Association of Physicists in Medicine
ANOVA	analysis of variance
CAD	computer-aided detection
CAE	computer-aided evaluation
CI	conformity index
CI_{DD}	two-dimensional conformity index with dose and distance incorporated
CI_{RTOG}	conformity index suggested by RTOG
CN	conformation number
COIN	conformity index proposed by Baltas
COSI	critical organ scoring index
CT	computed tomography
CTV	clinical target volume
DICOM	Digital Imaging and Communications in Medicine
DICOM RT	Digital Imaging and Communications in Medicine for radiation therapy
DVH	dose volume histogram
EUD	equivalent uniform dose
GTV	gross tumor volume
GTV_n	nodal gross tumor volume
GTV_{np}	nasopharyngeal gross tumor volume
GUI	graphical user interface
HTCI	healthy tissues conformity index

ICRU	International Commission on Radiation Units and Measurements
IMAT	intensity modulated arc therapy
IMRT	intensity modulated radiation therapy
IOD	information object definition
ISO	International Organization for Standardization
MLC	multileaf collimator
NP	nasopharyngeal region
NRMSD	normalized root-mean-square deviation
NTCP	normal tissue complication probability
NTSI	normal tissue sparing index
OAR	organ at risk
PACS	Picture Archiving and Communication System
P_{PTV}	target penalty function
PRV	planning organ at risk volume
PTV	planning target volume
ROI	region of interest
RT	radiotherapy
RTOG	Radiation Therapy Oncology Group
SMART	simultaneous modulated accelerated radiation therapy
TCI	target conformity index
TCP	tumor control probability
TV	target volume
TV_{RI}	target volume covered by the reference isodose
VMAT	volumetric modulated arc therapy
V_{RI}	reference isodose volume

Table of Contents

Chapter 1 Introduction

Radiotherapy is the mainstay treatment for head-and-neck cancer. Intensity-modulated radiotherapy (IMRT) is a precise form of radiotherapy which can conform radiation closely to the three-dimensional shape of tumor. Because of the close proximity of tumor and sensitive normal tissues in the head-and-neck regions, IMRT has gradually evolved as the standard of care for head-and-neck cancer. Despite its dosimetric advantages, introduction of IMRT in clinical practice has brought unique challenges to the radiation oncology team.

1.1 Development of Intensity Modulated Radiotherapy (IMRT)

Since the first therapeutic use of X-rays in the late 19th century, radiotherapy (RT) has undergone major advances at both the physical and biological levels. Historically, in two-dimensional radiotherapy planning, standard field borders were placed on identifiable bony anatomy resulting in generous margins around tumors to account for uncertainty of target position (Chau et al., 2007). The two-dimensional dose calculation was hardly accurate without considering the anatomic contour irregularity and tissue inhomogeneity (Goitein, 1982).

The invention of computed tomography (CT) by Godfrey Hounsfield in 1971 got the ball rolling in three-dimensional computerized treatment planning (Chernak et al., 1975; Webb, 2008). CT provides not only essential anatomic information, but also the basis for radiation dosimetry by reconstruction of electron density map that is deduced from CT numbers (Geise and McCullough, 1977; Sontag and Cunningham, 1978). The development of multileaf collimator (MLC)

systems in the early 1990s definitely marked a milestone on the way to the three-dimensional conformal radiotherapy (3DCRT). Enhanced dose conformation of the target volumes brings an undeniable dosimetrical advantage over conventional two-dimensional radiotherapy in reducing radiation dose to margins of healthy tissue around the tumor that is included to accommodate organ motion and tumor spread uncertainties (Galvin et al., 1992; Brewster et al., 1995). However, one of the most time-consuming tasks of the 3DCRT planning process is the delineation of the anatomic structures. Accurate delineation is essential for generating dose volume histograms (DVHs) which could summarize three-dimensional dose distributions in a graphical two-dimensional format. As a plot of a cumulative dose-volume frequency distribution, DVH shows promise as an effective tool for quantitative treatment plan analysis (Drzymala et al., 1991; Kessler et al., 1994).

Taking the 3DCRT one step further, IMRT revolutionized radiation therapy over the last two decades (Pirzkall et al., 2000). Unlike 3DCRT, IMRT is characterized by the use of non-uniform, modulated intensity of radiation to enhance dose distributions like painting a treatment volume with different intensity of radiation dose. Renowned for its dose-sculpting ability, IMRT has gained increasing popularity for treating concave-shaped targets and delivering simultaneous boosting dose to the targets (Gérard et al., 2010; Amosson et al., 2003). The IMRT plans in which the tumors are in close proximity to critical structures tend to incorporate steep dose gradients, as much as 10% per millimeter, to avoid too much radiation getting into normal healthy tissues (Bratengeier et al., 2009; Vieira et al., 2003). Hence, all aspects of the IMRT process should meet stringent requirements for accuracy and precision. Two major issues in the widespread

clinical adoption of IMRT are the extensive work in comprehensive quality assurance program and the growing demands for high-quality IMRT plans (McNair et al., 2003; Olson et al., 2012). Over recent years, there has been considerable automation of the IMRT process with the objective to ease staff workload and augment performance.

Implementation of image guidance into routine clinical workflow is crucial to the success of the IMRT (Chen et al., 2011). Daily verification using online cone beam computed tomography could minimize both setup error and organ motion uncertainty, consequently permitting reductions of the required target margins and normal tissue irradiation (Kupelian and Langen, 2011; Wu et al., 2011). Because of the regulation on gantry rotation speed, CT image guidance is greatly affected by breathing motion resulting in significant movement artifacts. This drawback has led to active investigation of the use of respiration-correlated four-dimensional CT to guide radiotherapy.

It is well known that respiratory motion is a main source of error in RT treatment planning especially for IMRT in which precise tumor localization and immobilization are of paramount importance (Mutaf et al., 2011; McClelland et al., 2011). In this era of image guided radiotherapy, four-dimensional medical imaging has been introduced in clinical practice for correction of motion artifacts and provision of temporal volumetric images for treatment planning (Bettinardi et al., 2010; Kuo et al., 2010). The existing strategies to take breathing motion into account include voluntary breath-hold, real-time tumor motion tracking or using patient-specific safety margins to ensure target coverage (Blessing et al., 2010; Nelson et al., 2010). In order to compensate for the intrafractional target

motion, several four-dimensional IMRT planning methods were designed enabling dynamic MLC-based tumor tracking (Tacke et al., 2010; Liang et al., 2009).

Organ deformation, tumor shrinkage and weight loss are often remarkable during the entire course of IMRT treatment. Image guided radiotherapy adapted to motion and anatomical changes has offered remarkable level of precision and accuracy in IMRT delivery. Apart from positional adaptive radiotherapy, megavoltage CT on a helical tomotherapy system provides the essential requirements for dose adaptive radiotherapy. It was found that the megavoltage CT values correlated extremely well with electron density (Sheng et al., 2005). Since the megavoltage CT numbers better represent the attenuation coefficients of the actual treatment beam, megavoltage CT images are potentially more relevant for dose recalculation based on changes to the patient (Langen et al., 2005; Duchateau et al., 2010). Online adaptive IMRT appears to be a promising approach for delivery of personalized cancer care (Murthy et al., 2011). Yet, effective real-time modification and evaluation of IMRT plans remain an area of major concern. The multidisciplinary team including the oncologists, physicists and radiation therapists could be overwhelmed by the exponential growth of workload, and thus the situation demands for the automation tools.

1.2 Challenges in quality control of IMRT plans

The therapeutic success of IMRT has been echoed in the radiotherapy community fueling widespread adoption. IMRT planning is more of an art, relying heavily on planner experience and human inspection of resultant dose distribution (Wu et

al., 2009). The sharp dose gradients in IMRT warrant careful examination of resultant plan. As an extension of DVH analysis, qualitative inspection of isodose distributions on each image slice is indispensable. Due to its dose-painting ability, IMRT plans typically exhibit higher degree of dose heterogeneity than conventional 3DCRT plans. With such complex and unconventional nature of IMRT dose distribution, detailed evaluation on the magnitude, size and location of all cold and hot spots (underdose and overdose areas respectively) relative to targets becomes crucial. The current quality control paradigm has relied primarily on personal judgment and experience. Even for experienced planners, identification of hot and cold spots from corresponding CT slices is definitely cumbersome and not error-free. The traditional manual practice of determining the best plan has been proved to be extremely difficult and the development of an automatic evaluation system would improve the situation.

IMRT for head-and-neck cancer poses a particular challenge as the anatomical site is complex with many critical and radiation-sensitive structures in close vicinity. Variation in spatial relationship between head-and-neck tumors and surrounding organs at risk (OARs) is remarkably heterogeneous. Though all OARs are important in relation to quality of life, prioritization should be done on a case-by-case basis during the optimization. Professional judgement and extensive experience are recognized as vital elements in producing high-quality IMRT plans for head-and-neck cancer. The overall IMRT planning time for head-and-neck cancer takes far more time than for conventional radiotherapy (Miles et al., 2005). Greater emphasis should be put on the quality control in radiotherapy delivery (de Crevoisier et al., 2007; Breen and Zhang, 2010).

The International Organization for Standardization (ISO) has suggested standards for use in radiation oncology to achieve consistency of practice and optimal quality (Pawlicki and Mundt, 2007). At present, the manual method of quality control for IMRT planning is ineffective as it requires substantial experienced personnel and institutional resources (Margalit et al., 2011). Upon completion of a new plan, the planner should explicitly assess the compliance of the plan to the plan acceptance criteria. All qualified plans are subject to a careful review and approval by the attending radiation oncologist. As a final check prior to treatment, a second physicist should closely scrutinize all treatment parameters to assure that the plan is clinically reasonable. Obviously, these quality control tasks performed by humans are both time- and labor-intensive, requiring sustained vigilance.

Conventionally, the prescription has been radiation dose at a point of interest. The International Commission on Radiation Units and Measurements (ICRU) Reports 50 (1993) and 62 (1999) suggested that dose-at-a-point reporting was no longer adequate for IMRT. Therefore, reporting of the near-maximum and near-minimum absorbed doses are recommended in ICRU Report 83 (2010) when judging the plan quality. As the targets and OARs increase in number, the plan evaluation becomes combinatorially complex. Interpreting such meticulous statistics has prompted the development of intelligent tools for automated dose-volume data analysis.

Apart from dose-volume-based prescription and reporting, ICRU Report 83 (2010) also recommended the use of dose conformity indices in the routine IMRT reporting. In the era of personalized cancer medicine, much emphasis has

been put on the inherent variability in tumors and the need for a tailor-made treatment regimen (Chiti et al., 2010). As the indicators of plan quality, a variety of indices have been proposed to describe the overall plan conformity. However, only few existing indices take the complex tumor geometry into account. Therefore, it is desirable to design a customized target conformity index which allows immediate appreciation of a plan.

Digital Imaging and Communication in Medicine (DICOM) is an international imaging communications standard developed by the American College of Radiology in conjunction with the National Electrical Manufacturers Association in 1992. DICOM has become the universal format for transmission and storage of medical images (Bidgood and Horii, 1992; Prior, 1993). To support the transfer of radiotherapy-related data, DICOM was extended from radiology to radiation therapy. A vast treasure-trove of information could be accessed by uniquely indexing all the tagged data in DICOM objects (Kamauu et al., 2006; Wang et al., 2011). With its flexible and open architecture, DICOM provides a useful means of extracting valuable information and developing some data mining systems.

1.3 Aim of the study

To make good use of this open standard, the aim of this study was to develop a DICOM-based computer-aided evaluation (CAE) system for automatic evaluation of IMRT plans on an independent platform. As a powerful complement to the CAE system, a personalized target conformity index (CI) was also designed to quantify the IMRT plan quality.

1.4 Objectives of the study

1. To develop a computer-aided evaluation system for automatic evaluation of IMRT plans.
2. To evaluate the computer-aided evaluation system by comparing the computed dose volume histogram data against the manually extracted data from the treatment planning system.
3. To develop a personalized target conformity index for comparison of IMRT plans.
4. To incorporate the personalized target conformity index into the computer-aided evaluation system.
5. To evaluate the plan quality discerning power of the personalized target conformity index in comparison with other widely used indices.
6. To explore the impact of use of computer-aided evaluation system on IMRT plan evaluation time.

1.5 Hypotheses

1. There is difference in the mean evaluation times with and without using the CAE system.
2. There is difference in the mean evaluation times between inexperienced and experienced planners.
3. There is difference in the effect of use of CAE system on evaluation time for experienced and inexperienced planners.

1.6 Chapter scheme of dissertation

This dissertation is structured as follows. Chapter 1 is the introduction to this thesis. It starts an overview of IMRT development, followed by challenges in quality control of IMRT plans, and why DICOM was used. It provides the necessary background, the aim and objectives of the study. Chapter 2 focuses on the clinical aspects of IMRT including the delivery methods and planning workflow and, more importantly, reviews the literature on the existing IMRT plan evaluation tools. In Chapter 3, features and applications of DICOM and DICOM RT in the field of radiology and oncology are highlighted. A review of literature with emphasis on their potentialities for data mining is also provided. The research methods for developments and subsequent evaluation of the CAE and the conformity index scoring systems are described in Chapter 4. Chapter 5 presents the research findings of the study as follows: the main features of the CAE systems, performance evaluation results followed by the comparison of plan quality discerning power among the conformity index scores and other physical and biological indices. Discussion of the research findings and conclusions of the study are given in Chapter 6, where the implications, limitations and recommendations for future research are addressed.

Chapter 2 Literature Review of IMRT

The invention of computed tomography (CT) as an imaging tool has revolutionarized the planning and treatment delivery in radiation therapy. It provides a third dimension to the viewing and planning of the tumor volumes and thus enables three-dimensional techniques in radiation therapy. After the introduction of three-dimensional conformal radiation therapy (3DCRT) in the early 1990s, intensity modulated radiation therapy (IMRT) followed soon after and has become a popular technology. The different IMRT methods and the existing plan evaluation tools will be reviewed in the following sections.

2.1 IMRT delivery methods

IMRT is a kind of three-dimensional conformal radiation treatment that allows the modulation of radiation intensity to shape the desired dose to the target volumes so as to provide highly focused radiation and the best conformity to the tumor volume with minimal impact to surrounding normal tissues. Today IMRT delivery methods with conventional linear accelerators are divided into two classes: static gantry IMRT and rotational IMRT (Yu et al., 2002; Wu et al., 2010). Static gantry IMRT techniques include "step and shoot" method and "sliding window" method. The former creates static field segments that can be superpositioned to build up the intensity profile. The latter method employs moving multileaf collimator (MLC) leaves.

Rotational IMRT delivery technique, can be called intensity modulated arc therapy (IMAT) and volumetric modulated arc therapy (VMAT) depending on

the manufacturer. It provides a continuous modulation of gantry speed, dose rate and MLC shapes simultaneously (Wiezorek et al., 2011; Shepard and Cao, 2011). Tomotherapy is a new kind of linear accelerator that combines a CT scanner with a linear accelerator and is specially designed for rotational IMRT. The radiation source and the collimator continuously revolve around the patient but in slices, similar to that of a CT unit. A dedicated binary MLC is used to modulate the fan beam while the patient is translated through the gantry (Welsh et al., 2006; Rong and Welsh, 2011). The first serial tomotherapy system approved by Food and Drug Administration in 1994 was known as the Peacock. It was implemented into clinical use at Memorial Sloan-Kettering Cancer Center in 1995 and gained unprecedented popularity over a very short period of time (Mackie, 2006).

Each IMRT delivery method has unique strengths and weaknesses. By using sequential delivery of smaller subfields, the "step and shoot" technique allows precise delivery and easy portal verification but this comes at the cost of prolonged treatment time. "Sliding window" technique requires substantially more monitor units to yield more complex dose distribution and smoothly varying intensities (Seco et al., 2001; Luan et al., 2004; Nicolini et al., 2005). On the other hand, rotational delivery techniques can enhance treatment precision by reducing the total treatment delivery time and the risk of intrafraction organ motion (Rao et al., 2010; Oliver et al., 2010; Palma et al., 2008). Using 51 angles in the rotation, helical tomotherapy offers more degree of freedom for beam modulation than linear accelerator-based IMRT, creating superior dosimetry. Without compromising target coverage, a marked improvement in sparing the organs at risk (OARs) was reported when shifting from linear accelerator-based IMRT to tomotherapy (Cendales et al., 2011).

2.2 IMRT planning workflow

IMRT has become a standard practice for a wide number of tumors, making the concept of "personalized medicine" a reality. The IMRT planning process is broken down into five steps:

1. Patient positioning and immobilization;
2. Image acquisition;
3. Targets and normal structures delineation;
4. Dose prescription and beam optimization; and
5. Treatment plan evaluation.

Concerns have been raised in relation to the impact of workload after large-scale adoption of online adaptive IMRT re-planning. Therefore, much interest is being focused on the automation of the IMRT planning process to clear the obstacles to individualized cancer therapy.

2.2.1 Patient positioning and immobilization

Since IMRT can deliver highly conformal dose distribution to tumor, precise patient positioning and immobilization techniques are mandatory (Saw et al., 2001). By comfortably securing the treatment site, custom-designed immobilization device helps eliminate patient movement and produce better reproducibility (Fuss et al., 2004). The use of thermoplastic cast is incorporated into routine treatment for patients with head-and-neck cancers (Velec et al., 2010). It has been demonstrated that the setup reproducibility of these devices was within 2 to 3 mm on a daily basis (Rotondo et al., 2008).

2.2.2 Image acquisition

IMRT needs a precise three-dimensional representation of the patient anatomy to permit the design of personalized treatments. The use of multimodality imaging allows improved target volume definition and geometrical precision (Kao et al., 2010; Tzikas et al., 2011). Like 3DCRT, a planning CT with the patient in treatment position is acquired featuring high geometrical accuracy with a measure of electron density (Skrzynski et al., 2010). Together with multiplanar capability and increased imaging functionality, magnetic resonance imaging provides superior characterization of soft tissues and visualization of tumor extent (Jonsson et al., 2011; Thoeny, 2011). The emergence of functional imaging techniques, such as magnetic resonance spectroscopy, positron emission tomography, and single photon emission computed tomography allows us to introduce the concept of biological target volume in IMRT treatment planning (Castadot et al., 2010; Partridge et al., 2010; Astner et al., 2010).

2.2.3 Targets and normal structures delineation

Encouraging IMRT results can only be achieved when the exact location and extension of targets are defined with respect to all OARs. Targets and normal structure delineation is a crucial step in the IMRT planning process. The gross tumor volume (GTV), clinical target volume (CTV) and planning target volume (PTV) concepts defined by the ICRU in Reports 50 and 62 are widely used (Figure 2.1). The GTV is the gross palpable or visible/demonstrable extent and location of malignant growth based on information obtained from various imaging studies, clinical and endoscopic findings, comprising the primary tumor and clinically involved lymph nodes. Based on the clinical knowledge about the microscopic spread of disease, CTV is expanded from the GTV with a CTV

margin to account for the potential microscopic extension. Geometric uncertainty of the target localization is recognized as one of the main obstacles to the success of IMRT. The PTV is designed to ensure that the CTV received the prescribed dose with a high degree of certainty. As a geometrical concept, PTV is expanded from the CTV with a PTV margin, accounting for patient setup uncertainty and internal organ motion. In ICRU 62, these factors are divided into an internal margin and a setup margin. The internal margin is defined based on the expected physiologic changes in organ size, shape and position relative to the patient geometry obtained at the treatment planning. The CTV plus the internal margin constitute the internal target volume. The PTV envelopes the CTV with the combination of internal margin and setup margin, taking into consideration the net effect of all possible geometrical variations (Purdy, 2004). Daily image guided localization helps minimize both setup and interfraction organ motion uncertainties, allowing for a reduced PTV margin to take into account the remaining intrafraction motion. It is desirable to tailor an individualized and tumor specific internal margin in the PTV (Reddy et al., 2009; Tanyi et al., 2010; Chen et al., 2011).

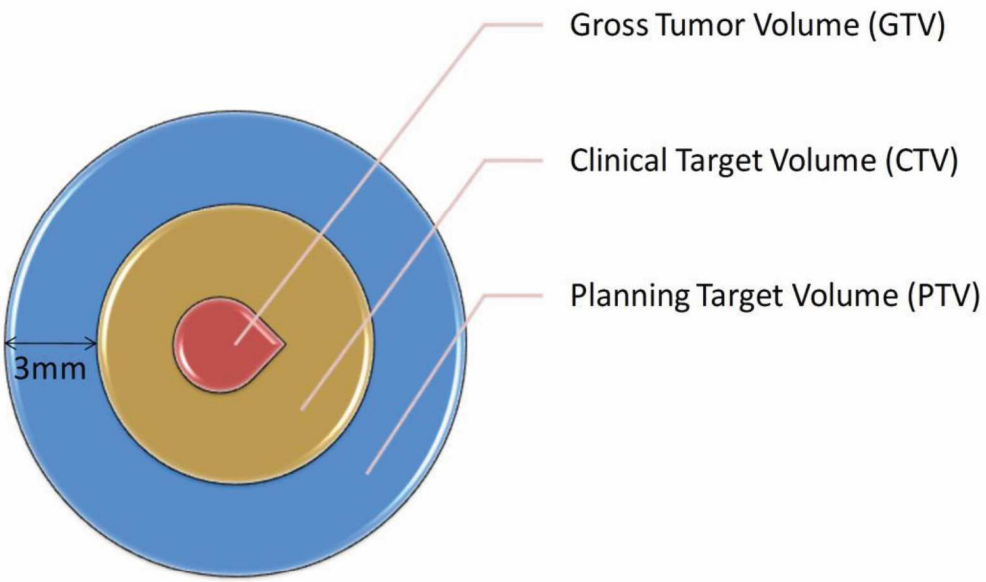

Figure 2.1. Target volume definitions according to ICRU Report 50 and 62.

In a similar manner, all dose-limiting organs known as OARs are drawn to enable optimal sparing during IMRT optimization. Table 2.1 lists the adjacent radiosensitive organs at different treatment sites.

Table 2.1. Adjacent radiosensitive organs in different anatomical regions.

Treatment sites	**Adjacent radiosensitive organs**
Head and neck	Brainstem, Spinal cord, Salivary glands, Optic structures, Larynx, Temporal lobes, Auditory apparatus
Chest	Spinal cord, Lung, Heart
Abdomen	Spinal cord, Liver, Kidneys, Bowel, Stomach
Pelvis	Bladder, Rectum, Bowel

IMRT is more sensitive to geometric uncertainties. ICRU Report 62 introduced the concept of the planning organ at risk volume (PRV), in which a suitable margin

could be added around the OAR to account for movement and uncertainties in setup. Manual slice-by-slice delineation is one of the most tedious and time-consuming tasks in IMRT planning. The use of automatic model-based deformable segmentation could be a solution to such drawback, resulting in reduced inter- and intra-observer variability (Wang et al., 2008; Bueno et al., 2011; Speight et al., 2011).

2.2.4 Dose prescription and beam optimization

To provide clear guidelines for IMRT planning, well defined site-specific jointly-developed treatment protocols should be set out. Nowadays, the IMRT dose prescription and specification for a particular treatment situation differ substantially among different institutions, raising concerns about the validity of comparing clinical outcomes for IMRT (Das et al., 2008; McGarry et al., 2011).

There are two paradigms for radiotherapy treatment planning: forward planning and inverse planning. In conventional forward planning, the beam configuration, beam weighting and blocking designs are assigned and refined by trial and error until a satisfactory plan is produced. In inverse planning, the desired dose distribution is firstly prescribed and the computer is run to create a custom plan that best matches all the input criteria.

With sophisticated computer software, IMRT plans are always generated using the inverse planning. A golden key to the entire inverse planning process is the specification of standard beam arrangement and physically achievable optimization parameters. Many investigators demonstrated that automatic selection of beam orientations could lead to improved quality and consistency of

treatment planning (Lei and Li, 2009; Craft and Monz, 2010; Zhang et al., 2011). Samuelsson and Johansson (2003) showed that increasing the number of beams in IMRT planning offered better quality of plan with steeper dose gradients around the targets and OARs.

An IMRT plan can be generated using various optimization algorithms. In beamlet-based inverse planning, each radiation field is firstly divided into multiple pencil beams enabling custom design of optimum dose distributions (Zhang et al., 2005). Despite its popularity, this approach has several shortcomings. Firstly, the monitor units are often unnecessarily high with complex intensity patterns (Men et al., 2007). A huge number of beams that must be considered during the optimization prohibit the use of a precise calculation algorithm from the beginning so that an additional sequencing step is required leading to plan degradation (Milette and Otto, 2007).

For these reasons, a new, reliable and more efficient approach for IMRT planning is of paramount concern. Direct aperture optimization is an inverse planning technique whereby the weights and shapes of apertures are optimized simultaneously. As compared to the traditional beamlet-based IMRT, direct aperture optimization IMRT improved the planning and delivery efficiency while maintaining dosimetric quality, making it a robust tool for IMAT and VMAT treatment planning (Broderick et al., 2009; Salari et al., 2011).

Traditionally, the inverse treatment planning optimization was kicked off by assigning a series of optimization parameters and tweaking manually until a satisfactory plan was found. Recent studies introduced a hybrid optimization

algorithm by using both physical and biological objective functions (Hartmann and Bogner, 2008; Dirscherl et al., 2011). Compared to the dose-based plans, the biologically-based plans could be characterized by better OARs sparing with comparable target coverage (Semenenko et al., 2008; Qi et al., 2009). However, the major impetus for the biologically-based IMRT optimization is the scarcity of evidence-based data for radiobiological models (Kim and Tomé, 2010). Interpretations should be made with caution.

To further improve the IMRT plan quality and reduce planning time, Hong et al. (2008) and Craft et al. (2012) developed the robust multi-criteria optimization methods by focusing on the tradeoffs between different treatment planning goals. One approach is based on the computation of a set of Pareto-optimal plans, thus providing a means to select the best plan for each patient.

Currently, no consensus exists on the best optimization algorithm for IMRT planning. Whichever method is adopted, adequate quality control process should be carried out to maintain a high standard of resultant IMRT plans. Therefore, this study aims to develop an automatic IMRT plan evaluation system for controlling and maintaining a desired level of plan quality for head-and-neck cancer.

2.2.5 Plan evaluation

No matter how experienced the planners are, the IMRT optimization and evaluation processes involve a human iteration loop relying heavily on subjective and qualitative plan evaluation. As shown in Figure 2.2, each IMRT plan has two

primary concerns – target coverage and normal tissue sparing. A three-dimensional plot can connect three variables together. In this figure, the x- and y-axes are related to the OAR sparing and the PTV underdose, while the z-axis shows the number of optimization iteration. A key goal of IMRT is to minimize complications to normal tissues by decreasing the dose to OARs while to maximize tumor control by increasing the dose to PTV. To obtain a better plan, the optimization and evaluation loop could continue until no further improvement is required. The determination of the best plan requires a clinical decision based on the balance between adequate target coverage and normal tissue sparing.

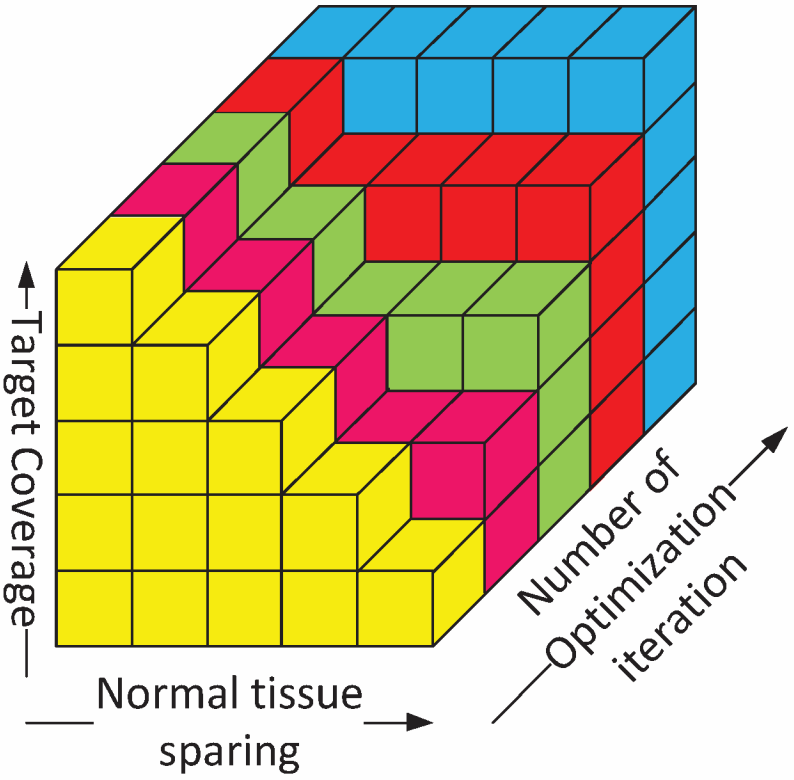

Figure 2.2. Two primary concerns for an IMRT plan.

2.3 IMRT plan evaluation tools

Conventionally, the suitability of a treatment plan needs to be evaluated carefully using dose volume histograms (DVHs) and planar dose distributions. DVH could summarize three-dimensional dose distributions in a graphical two-dimensional format. Figures 2.3 and 2.4 show the cumulative DVHs with ideal curves for the target volume and the OAR respectively. Ideally, 100% volume of the target should receive the maximum prescribed dose e.g. 70Gy while a little volume of OAR as possible should receive the least amount of radiation dose. Despite lacking spatial information, DVHs provide a global view of whether the resultant plan meets the set limits.

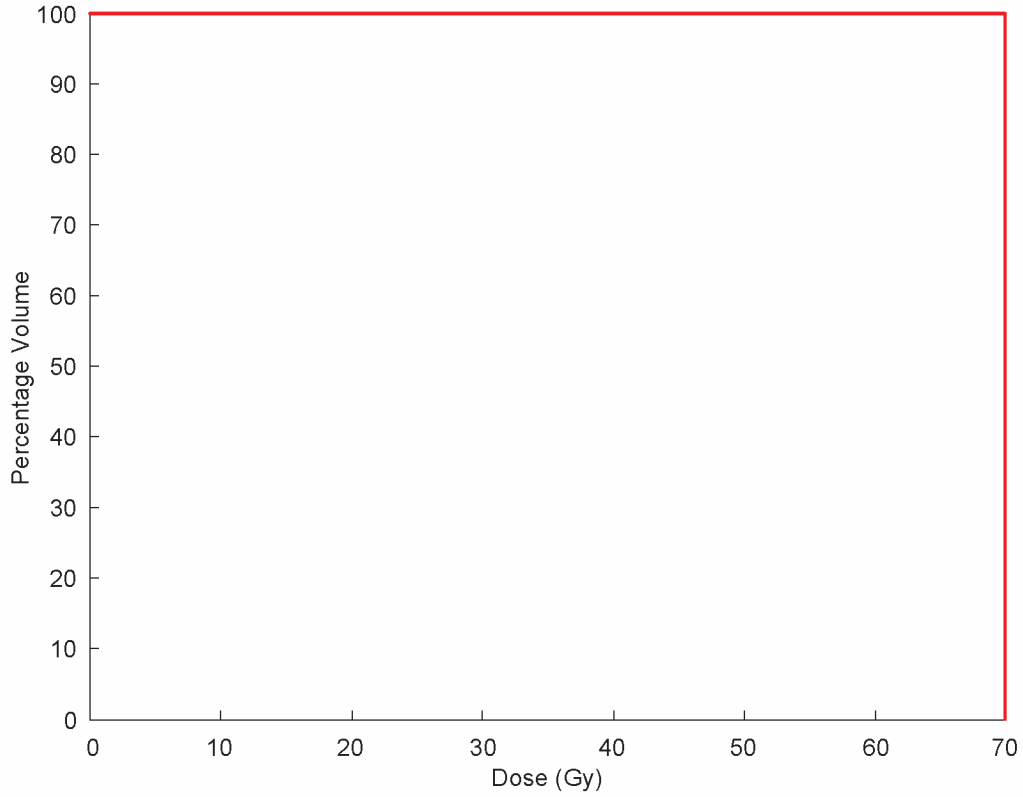

Figure 2.3. The ideal DVH for the target volume.

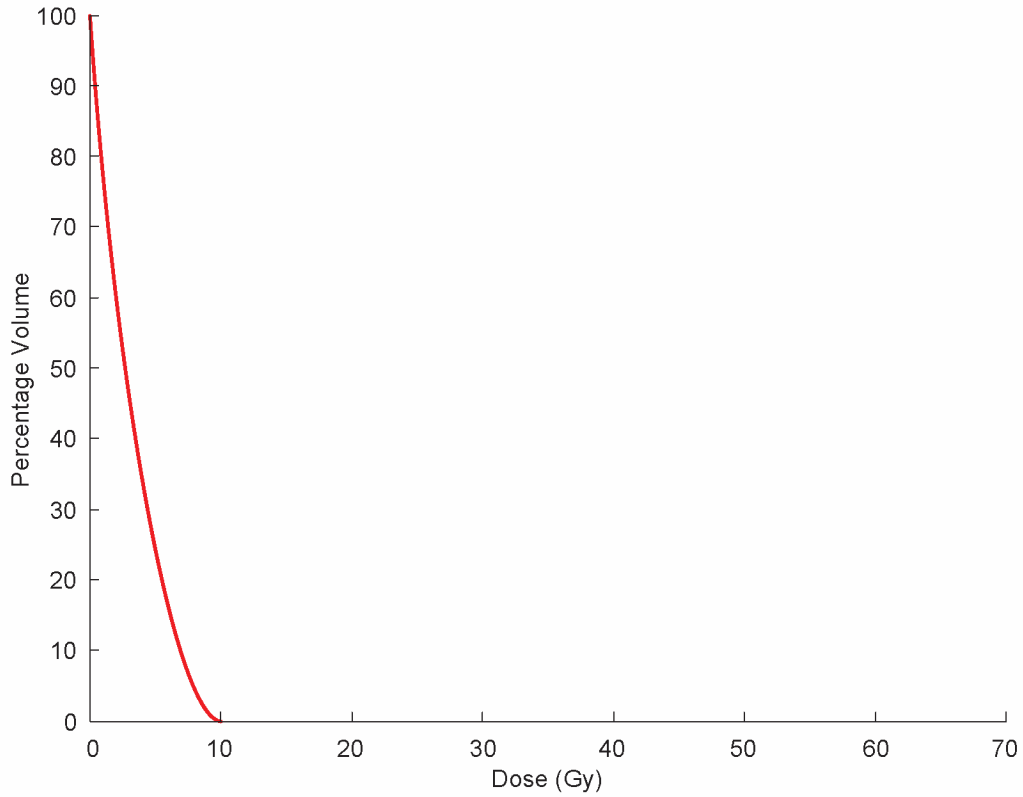

Figure 2.4. The ideal DVH for the organ at risk.

Planar dose distributions are radiation dose curves overlaid on CT images. Such dose distribution could show areas of overdose or underdose in the treatment plan. Though less frequently used, the conformity index (CI) and the biological index are also adopted to express the degree of conformity of the planned dose distribution to the target volume. The histogram, the conformity index as well as other biological indices will be further reviewed in the rest of this chapter.

2.3.1 Dose volume histograms (DVHs)

Quality of a treatment plan is often measured by a DVH which is presented in either differential or cumulative form. The cumulative DVH is a plot of the volume of a given structure receiving at least a given absorbed dose against dose whereas the differential DVH shows the fractional volume receiving a specified

dose. Despite the lack of spatial information, DVHs are accepted as a tool for rapid screening of different rival plans since the late 1970s. When judging the plan quality, the DVH data for each region of interest is extracted individually.

The International Commission on Radiation Units and Measurements (ICRU) has devoted continuous effort in providing a basis for evaluation of treatment plans. In the 3DCRT era, the ICRU Report 50 issued in 1993, defined simple parameters to characterize the spatial dose distribution like the maximum and minimum doses to the PTV, absorbed doses to OARs and ICRU reference dose for reporting dose. After entering the era of volumetric PTV prescribing, ICRU Report 83 (2010) recommended a near-minimum dose ($D_{98\%}$) (which indicates the dose received by 98% of the PTV), a near-maximum dose ($D_{2\%}$) (dose received by 2% of the PTV) and a median dose ($D_{50\%}$) (dose received by 50% of PTV) for dose reporting purposes. These dose volume statistics from DVHs should be routinely analyzed.

Later, the dose surface histogram was proposed as a treatment planning tool for thin walled hollow structures such as the bladder and the rectum. Compared with the dose to volume, estimation of the dose-surface is more biologically relevant. However, the locations of hot and cold spots are not appreciated. Plans that had similar DVHs or dose surface histograms could have different spatial and biological characteristics.

Cheng et al. (1999) considered the loss of spatial information and introduced the z-dependent DVH which was defined as a differential DVH with respect to CT slice position. As a two-dimensional analog to three-dimensional DVH, z

-dependent DVH provides the spatial variation and the size and magnitude of high- and low-dose regions. However, the precise locations of hot and cold spots within each CT yet remain unknown.

By incorporating the spatial information in the DVH format, Zhao et al. (2010) introduced the concept of spatial DVH to help the planners locate the regions of greater risk inside the target. The spatial DVH is color coded representing dose voxels in the different regions, making it less intuitive than the simple DVH format. Without condensing the spatial DVH into a single index, the planners could be easily overwhelmed by the abundant information.

Recognizing the fact that dose optimality depends on the individual patient anatomy, Wu et al. (2009) designed a geometry-based OAR dose prediction tool to assist planners in OAR sparing estimation. The overlap volume histogram which characterizes the relative spatial configuration of the OARs and the targets, proved successful in improving the quality of treatment plans.

More recently, an adaptive IMRT plan quality evaluation tool using machine learning approach was developed which estimated the DVH for OARs based on high quality prior plans as a reference (Zhu et al., 2011). The concept of a shape relationship descriptor, called the distance-to-target histogram was introduced by providing a summarized characterization of organ shape relative to the PTV. With automatic feature selection, it is a promising tool to identify hidden patterns in data. By combining advantages of principal component analysis and support vector regression, Zhu's system could provide a unique solution and benefit by reducing redundancy without losing much of the information. System

performance is robust even when the training samples have unfavorable bias (Van Belle et al., 2011). Nevertheless, it does not provide a ranking system for simple and clear evaluation of different IMRT plans.

Since IMRT plan evaluation requires more attention to detail, it has become more of a demanding issue to develop a reliable computer-aided system to improve the efficiency of the evaluation process. Recently, Pyakuryal et al. (2010) designed an automated system for evaluation of DVH statistics. By eliminating manual data extraction, the system could increase the efficiency and accuracy of DVH statistical analysis. However, other essential features such as slice-by-slice isodose review were not provided in Pyakuaryal's work. To bridge the gap, it is desirable to develop an all-in-one IMRT plan evaluation system to put a comprehensive range of features at planners' fingertips.

Treatment plan quality evaluation and comparison have long been the thorny issues because resultant dose distribution is closely constrained by the patient anatomical geometry, the complexity of clinical goals, the subjective experiences of the planners. Dealing with the tradeoff between cold spots inside the target and hot spots in nearby OARs remains challenging in radiation therapy planning. In particular, IMRT plan evaluation requires more diligence and special attention to cold or hot spots in unexpected locations. To assure the IMRT plan quality, some quantitative quality control measures are an absolute necessity.

2.3.2 Conformity indices (CIs)

Since the emergence of advanced radiotherapy techniques like IMRT and

stereotactic radiotherapy in the mid-1990s, the ICRU Report 62 was published in 1999 so as to keep up to date with current practice. Apart from the three levels for treatment plan reporting, the conformity index for the PTV was also introduced.

2.3.2.1 Conformity index and target volume

As an extension of slice-by-slice dosimetric analysis and DVHs, the conformity index (CI) was firstly proposed in the Radiation Therapy Oncology Group (RTOG) radiosurgery guidelines in 1993 and also described in Report 62 of the ICRU. Their definition was the ratio of reference isodose volume (V_{RI}) to target volume (TV). Depending on the choice of V_{RI}, the results vary considerably leading to erroneous conclusions. The 95% isodose volume following the ICRU 50 guidelines is systemically used as V_{RI} which corresponds to the parameters used for treatment planning (Menhel, 2006).

According to the RTOG guidelines, the treatment plan is considered to comply with the protocol if and only if this index is situated between 1 and 2. The plan has a minor violation as judged by the RTOG guidelines if the index is between 2 and 2.5 or 0.9 and 1. The treatment plan is rated as having major violation by RTOG standards if the index is less than 0.9 or more than 2.5.

Despite being easy to interpret, conformity index proposed by RTOG (CI_{RTOG}) never takes into account the degree of spatial intersection of the two volumes or their shapes. It could yield false perfect score in the extreme cases of nonconcordance of target and isodoses.

Knöös et al. (1998) reported a radiation conformity index to evaluate conformal treatment plans and it was defined as the ratio of the PTV to the volume enclosed by the prescription isodose. Like CI_{RTOG}, this radiation conformity index inevitably results in a false perfect score when the same shape and size of the treated volume and target volume are not perfectly overlapped as shown in Figure 2.5, where both (a) and (b) would generate a score of 1.

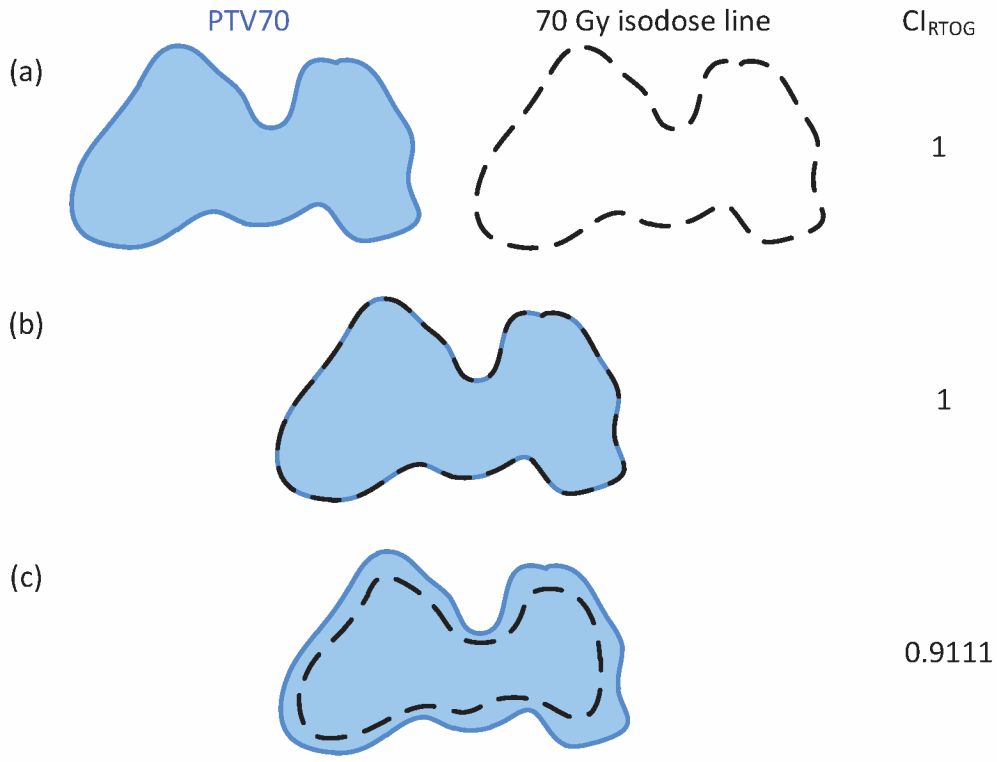

Figure 2.5. Examples showing different radiation conformity indices.

To get around the problem, the Saint-Anne, Lariboisière, Tenon (1998) suggested a modified index for stereotactic radiotherapy namely coverage volume factor which attempted to compensate for the potential false-positive results. The coverage volume factor is a figure of merit calculated from the target dose-volume data as the fraction of target volume that receives a minimum specified therapeutic dose. The index, nevertheless, does not quantify the

irradiated critical structure volumes surrounding the target.

In terms of target coverage, Leung et al. (2007) demonstrated the limitations of existing indices based exclusively on the prescribed isodose, which did not explicitly include the specific evaluation of underdose and overdose problems. A credit-based merit function M, also known as target coverage factor, was hence introduced taking into account all PTV check point doses which were used as a guideline to approve a treatment plan. M was defined as

$$M = \frac{1}{r}\sum_{j=1}^{r}\left\{\frac{\sum_{i=1}^{p}\left(\frac{V_{T_j,D_i}}{V_{T_j,RD_i}}\right)+\sum_{i=1}^{q}\left(1-\frac{V_{T_j,D_i}}{V_{T_j,AD_i}}\right)}{\sum_{i=1}^{p}\left(\frac{100}{V_{T_j,RD_i}}\right)+q}\right\}, \qquad (2.1)$$

where p was the number of cold spot checks, q was the number of hot spot checks, r was the number of targets of different prescription doses, V_{T_j,D_i} represented the volume of the j^{th} target (in %) receiving dose of at least the i^{th} dose level, V_{T_j,RD_i} represented the minimum volume of the j^{th} target (in %) receiving at least the i^{th} dose level and V_{T_j,AD_i} represented the allowable volume of the j^{th} target (in %) receiving at least the i^{th} dose level.

Penalty is incurred based on target dose-volume violations. Meanwhile, credit is awarded when the volume exceeds the minimum PTV dose requirement for plan acceptance. The primary strength of this function is its ability to monitor the presence and magnitude of hot and cold spots. Yet, no differential penalty is enforced based on the type of violation. Compared with cold spots, hot spots within the target are usually judged as being more clinically acceptable provided

they do not exceed a certain dose limit.

On the other hand, Miften et al. (2004) intended to develop the target conformity index (TCI) employing a flexible penalty function. The TCI was defined as:

$$TCI = P_{PTV} \times \left(\frac{PTV_{TD}}{PTV} \right), \tag{2.2}$$

where PTV_{TD} was the part of PTV enclosed by the therapeutic dose. An exponential function was adopted to model the target penalty function (P_{PTV}), resulting in different penalty values based on the magnitude of dose-volume violation and the type of violation. The penalty values range between 0 and 1. A more drastic Gaussian function is adopted to penalize cold spot since this is somewhat more of a clinical problem than hot spot. However, insufficient spatial information is available to exactly locate the overdose and underdose regions.

2.3.2.2 Conformity index and healthy tissue

Lomax and Scheib (2003) presented healthy tissues conformity index (HTCI) taking into account exclusively the irradiation of healthy tissues. It was determined as the ratio of the target volume covered by the reference isodose (TV_{RI}) to the reference isodose volume (V_{RI}). By definition, a treatment plan with HTCI less than 0.6 is considered to be non-conformal. Even though HTCI could quantify the undesirable dose delivered to the normal tissue, it does not distinguish different critical organs. This index, similar to CI_{RTOG} and coverage volume factor, was defined and evaluated in the context of stereotactic radiotherapy.

There are several practical limitations that should be kept in mind when using this index. As Leung et al. (2007) pointed out, HTCI could lead to a potential false perfect score when just a tiny reference dose volume is located inside the target resulting in obviously suboptimal target coverage. More importantly, this evaluation model could break down whenever simultaneous integrated boost approach is applied with several targets receiving different prescribed doses. Though the conformity of high-dose targets is truly reflected, HTCI could give erroneous results for coverage of intermediate- and low- risk targets. With a slightly revised definition of TV_{RI}, a modified HTCI was introduced by Leung et al. (2007) to compensate for these defects. The irradiated target volume as defined represents the target volume whose prescription dose is higher than or equal to the reference dose level. The effect of different doses to targets could hence be demonstrated. To generalize the formula to cater for numerous prescribed doses to various targets, $HTCI$ was redefined as

$$HTCI = \frac{1}{r}\sum_{i=1}^{r}\left(\frac{TV_{RI,i}}{V_{RI,i}}\right), \tag{2.3}$$

where r was the number of targets of different prescription doses. $TV_{RI,i}$ represented the target volume covered by the i^{th} reference dose and $V_{RI,i}$ represented the total isodose volume of the i^{th} reference dose.

2.3.2.3 Global conformity index (Target volumes and healthy tissues)

Van't Riet et al. (1997) and Paddick (2000) postulated an alternative conformity index (called conformation number) comprising two terms: the first was a measure of dosimetric target coverage, and the second was a measure of normal tissue overdose. The conformation number (CN), also known as $CI_{Paddick}$, was

defined as

$$CN = \frac{TV_{RI}}{TV} \times \frac{TV_{RI}}{V_{RI}}, \tag{2.4}$$

where TV_{RI} represented the target volume covered by the reference isodose, TV represented the target volume and V_{RI} represented the volume of the reference isodose.

Using this definition it is clear that $CN = 1$ when there is a complete target coverage, as well as complete organ sparing. Any deviation in either one of these parameters results in a lower value of CN. Unlike radiation conformity index and $CI_{RTOG,}$ it yields no false positive result. However, CN raises two particular comments. Firstly, it suffers from an inherent loss of information that accounts for more than one factor. Different plans with vastly differing potential outcomes could have the same value of CN. Secondly, it only addresses a global healthy tissue dose, lumping all non-tumor tissue together as normal tissue.

2.3.2.4 Conformity index taking into account critical organs

Initially proposed for brachtherapy, the conformity index of Baltas et al. (1998) abbreviated as COIN was the production of CN (Van't Riet et al., 1997) and a term accounting of critical organ doses. COIN was defined as

$$COIN = CN \times \prod_{i=1}^{N_{co}} \left(1 - \frac{V_{coref,i}}{V_{co,i}} \right), \tag{2.5}$$

where N_{co} represented the number of critical organs, $V_{coref,i}$ represented the critical organ volume receiving at least the reference dose, $V_{co,i}$ represented the critical organ volume, and CN given in (2.4) represented the Van't Riet's

conformation number.

Penalty is given whenever OAR volumes receive at least the prescription doses. Nevertheless, in many cases, OAR tolerances are much lower than tumor prescription doses. $COIN$ presents two significant drawbacks. Firstly, it provides indissociable information, making it impossible to discern the contribution of each term to the resultant $COIN$ value. The second issue is that $COIN$ is not calculated for each organ at its specific tolerance level.

2.3.2.5 Conformity index scoring for critical organs

As opposed to the $COIN$ index, critical organ scoring index (COSI) was developed specifically to compare individual critical organ's involvement at different dose levels (Menhel et al., 2006). The $COSI$ was defined as

$$COSI = 1 - \frac{V(OAR)_{>\text{tol}}}{TC_V}, \tag{2.6}$$

where $V(OAR)_{>\text{tol}}$ was the fraction of volume of OAR receiving more than a pre-defined tolerance dose, and TC_V was the volumetric target coverage, defined as the fractional volume of PTV covered by the prescription isodose.

Any deviation from the perfect score of unity could be either due to insufficient target coverage or critical organ overdose. Its main gain is the ability to distinguish different tolerance doses for different organs whereas CN only addresses a global healthy tissue dose. Knowing which OAR is being assessed, the physicians could make a more informed choice of the optimal plan. In extreme cases, $COSI$ could be equal to unity when a plan provides a complete organ sparing, regardless of tumor coverage. Though $COSI$ could score target

underdoses and OAR overdoses, it contains no information about the overall plan conformity. Owing to a certain loss of information, different quality plans could have identical $COSI$ values requiring further investigation of DVHs and isodose lines to determine their relative merits.

To go one step further, Menhel et al. (2006) also introduced a simple and visual two-dimensional representation of $COSI$ versus CI proposed by Lomax and Scheib (2003) to improve the specificity. The most significant advantage of the $COSI$ versus CI formulation is its ability to simultaneously compare multiple plans and multiple critical structures, clearly depicting the tradeoffs between target coverage and critical organ irradiation.

As mentioned earlier, a plan with a perfect $COSI$ score could be caused by complete organ sparing but poor target coverage. Since $COSI$ and CI are independent parameters, visual inspection of $COSI$ versus CI plot could immediately reveal the cold spots in target with a low CI value. However, for more complex cases with an array of OARs, multiple plans comparison in one plot could be problematic, making slice-by-slice isodose evaluation unavoidable. In spite of this complicated plan comparison process, the power of $COSI$ versus CI formulation to rank rival plans is greater than either index alone.

A penalty function P, on the other hand, was developed by Leung et al. (2007) for quantifying dose-volume violations for each critical structure using the cumulative DVH and was defined as

$$P = \frac{1}{n}\sum_{j=1}^{n}\left\{\frac{1}{m}\times\sum_{i=1}^{m}\left[1-\frac{V_{o_j,D_i}}{V_{o_j,AD_i}}\right]\right\}, \qquad (2.7)$$

where n was the number of critical organs to be monitored, m was the number of check points used for the j^{th} critical organ, V_{o_j,D_i} represented the volume of the j^{th} critical organ (in %) receiving dose of at least the i^{th} dose level and V_{o_j,AD_i} represented the allowable volume of that organ (in %) receiving at least the i^{th} dose level.

For a given planning protocol, various dose levels at which maximum tolerable normal tissue volume are examined. Any negative value at individual check point dose is considered a protocol violation. Value approaching 1 therefore represents the favorable sparing of critical structures. The unique feature of P function is the expression having an intrinsic weighting with respect to the user's protocol. For numerous critical organs with multiple check points, P function could still perform well. Yet, the index has room for improvement as the relative importance of various OARs could not be distinguished.

Normal tissue sparing index (NTSI) as presented by Miften et al. (2004) allowed organ specific considerations making it customizable to planner's specifications. The $NTSI$ was defined as

$$NTSI = P_{NTV} \times \left(1 - \frac{NTV_{TD}}{NTV}\right). \tag{2.8}$$

The NTV_{TD} / NTV ratio reported the ratio of normal tissue volume covered by the therapeutic dose. P_{NTV} was a penalty function as a value between 0 and 1, specifying normal tissue subvolume limits exceeding tolerance doses. For an ideal case, P_{NTV} is 1 with complete sparing of normal tissue. A value of less than 1 implies a penalty is enforced based on organ specific dose-volume

violations, driving the $NTSI$ down toward zero. Penalty values for each OAR are predetermined in collaboration with physicians and planners according to their estimate of the acceptable toxicity risks.

2.3.3 Biological Indices

A simple premise of radiotherapy is to maximize the probability of cure with a minimum of side effects. Over the past decade, there has been a surge of interest in biological modeling. Considerable studies attempted to integrate biological information into the current clinical planning paradigm (Sanchez-Nieto and Nahum, 2000; Das, 2009; Bruzzaniti et al., 2011). Tumor control probability (TCP) and normal tissue complication probability (NTCP) models are commonly adopted to estimate the radiological response.

2.3.3.1 Tumor control probability

A variety of TCP models have been proposed for evaluating the efficacy of the treatment plans. Classical expression for the TCP was based on the assumption that the number of clonogens surviving a given radiation regimen had Poisson distribution, which led to

$$TCP = \exp(-n_0 \times S(D)), \tag{2.9}$$

where n_0 was the initial number of cells and $S(D)$ denoted the fraction of cells surviving radiotherapeutic dose D. The linear quadratic model was widely used to describe the cell survival curve, considering both lethal and sublethal radiation damage. Presuming that the tumor cell population was uniform and that the effect of the treatment was independent of cell cycle, the $S(D)$ was

generally expressed as

$$S(D) = \exp(-(\alpha D + \beta D^2)), \tag{2.10}$$

where D was the dose in Gy, α represented the linear non-repairable component while β represented the quadratic repairable component of cell survival curve. The strength of this model is its simplicity. There is a range of possible α and β values across tissue and tumor types characterizing their intrinsic radiosensitivity.

Expressions for TCP could be derived in a number of different ways with varied degrees of complexity. Tucker et al. (1990) were among the first to question the validity of the oversimplified Poisson TCP model. Webb et al. (1993) extended the TCP model to account for the inter-patient tumor cell heterogeneity and non-uniform dose delivery. Several studies noticed that radiation damage of tumor cells was in fact a stochastic birth-death process (Yakovlev, 1993; Hanin et al., 2001). Pioneered by Zaider and Minerbo (2000), several derivations of TCP formulas were developed to account for the sophisticated cell population models. Dawson and Hillen (2006), based on the non-Poissonian model of Zaider and Minerbo (2000), derived a TCP formula including the cell cycle dynamics. By considering two subpopulations, it was presumed that all newly born cells were in a quiescent stage being less sensitive to radiation before becoming active.

2.3.3.2 Normal tissue complication probability

Another biological endpoint for quantitative comparison of rival treatment plans is to estimate the likelihood of radiation-induced complications. As the predictors

of the radiobiological effect for OARs, various *NTCP* models attempt to combine the dosimetric and anatomic information into a single parameter.

By ignoring the dose variation in the volume, the empirical Lyman model (1985) described complications association with uniform partial organ irradiation. To allow inclusion of heterogeneous dose distributions, Kutcher and Burman (1989) proposed the effective volume technique to modify the inhomogeneous normal tissue DVH to an equivalent uniform one in which the effective volume was irradiated to the maximum dose. The Lyman-Kutcher-Burman *NTCP* model combining the Lyman model with the Kutcher-Burman DVH reduction algorithm was currently widely used (Deasy, 2000). In this model, the *NTCP* was uniquely determined from the DVH using two fundamental equations:

$$NTCP = \frac{1}{\sqrt{2\pi}} \int_{-\infty}^{t} \exp\left(-\frac{x^2}{2}\right) dx, \quad t = \frac{EUD - TD_{50}}{m \times TD_{50}}, \tag{2.11}$$

where $\frac{1}{\sqrt{2\pi}} \exp\left(-\frac{x^2}{2}\right)$ is probability density function, $\frac{1}{\sqrt{2\pi}} \int_{-\infty}^{t} \exp\left(-\frac{x^2}{2}\right) dx$ is the area under standard normal curve, EUD was the equivalent uniform dose, TD_{50} was the uniform dose given to the entire organ volume that resulted in 50% complication risk and m was a measure of the slope of the sigmoid curve represented by the integral of the normal distribution.

Integration of the *TCP* and *NTCP* models was first proposed by Ågren et al. in 1990. In its simplest form, the uncomplicated tumor control probability defined as the probability of complication-free tumor control was given by the product of *TCP* and (1 minus *NTCP*) (Kutcher and Burman, 1989). To integrate biological dose washout effects into static physical dose distribution, the dose convolution filter model was introduced for more accurate prediction of

tumor control and tissue response (Huang et al., 2010).

2.3.3.3 Equivalent uniform dose

As an alternative DVH-reduction method, Niemierko (1997) suggested the concept of equivalent uniform dose (EUD) for tumors and OARs taking into account the organ functional architecture and the biological response characteristics of each structure. By definition, EUD is the uniform dose which leads to the same response probability as the corresponding inhomogeneous dose distribution. EUD application has gained considerable popularity in the realm of biologically based treatment planning because of its mathematical simplicity and incorporation of information about organ functional architecture. To compare target and OAR dose distributions in terms of their biological effectiveness, a generalized EUD was computed using

$$EUD = \left(\frac{1}{N} \sum_{i=1}^{N} D_i^a \right)^{\frac{1}{a}}, \tag{2.12}$$

where N was the number of voxels in the structure of interest, D_i was the dose in the i^{th} voxel and a was the tissue-specific parameter that described the dose-volume effect. Depending on tissue type and structures, overdose and underdose regions are of paramount importance. The value of "a" is negative for all tumor, for which cold spots are heavily weighted leading to large effects on the EUD. The a-values close to 1 are typical for parallel normal tissues, such as parotid glands, liver and lung, for which the EUD corresponds to the mean dose. For serial structures such as the spinal cord, hot spots are of greatest concern regarding $NTCP$, "a" approaches positive infinity (Jaganathan et al., 2011). On the whole, the DVH of the volume of interest is summarized by the

EUD which is subsequently related to the TCP and $NTCP$.

In summary, IMRT could offer potential advantages but existing evaluation tools suffer from several major drawbacks. Clinical application of biological indices for treatment plan evaluation is hampered by the lack of consensus on the most appropriate biological model and uncertainties in tissue-specific parameter estimates. Further validation is certainly warranted but it falls outside the scope of this study. To streamline the IMRT evaluation workflow and increase the consistency in plan quality, emphasis of this study was put on the development of a computer-aided evaluation system with a novel conformity index for automatic evaluation of IMRT plans.

Chapter 3 Literature Review of Digital Imaging and Communication in Medicine (DICOM) and its utilization

3.1 Digital Imaging and Communication in Medicine (DICOM)

DICOM is an international imaging communications standard developed by the American College of Radiology in conjunction with the National Electrical Manufacturers Association in 1992. It is used for transmission of medical images (Bidgood and Horii, 1992; Prior, 1993). It facilitates interoperability of medical imaging equipment by specifying a set of protocols, transfer syntaxes and semantics of commands. A conformance to DICOM statement is required nowadays from all manufactures to ensure interoperability between equipment and storage in the current Picture Archiving and Communication System (PACS) in radiology departments. The DICOM standard has reached well beyond radiology and been extended across multiple specialties such as radiation therapy, pathology, cardiology, ophthalmology, dentistry, veterinary, neurology and surgery (Chen, 2001; Frommelt et al., 2002; Farman, 2005).

DICOM uses the object-oriented design concepts. All real-world data such as patients and image studies as well as their attributes are grouped into modules as shown in Figure 3.1 which describes the real world as a hierarchical structure. At the top level is the patient. Each patient can have multiple studies, each of which may hold several series. Each series can have one or more images (Clunie and Carrino, 2002; Kabachinski, 2005; Kahn et al., 2007).

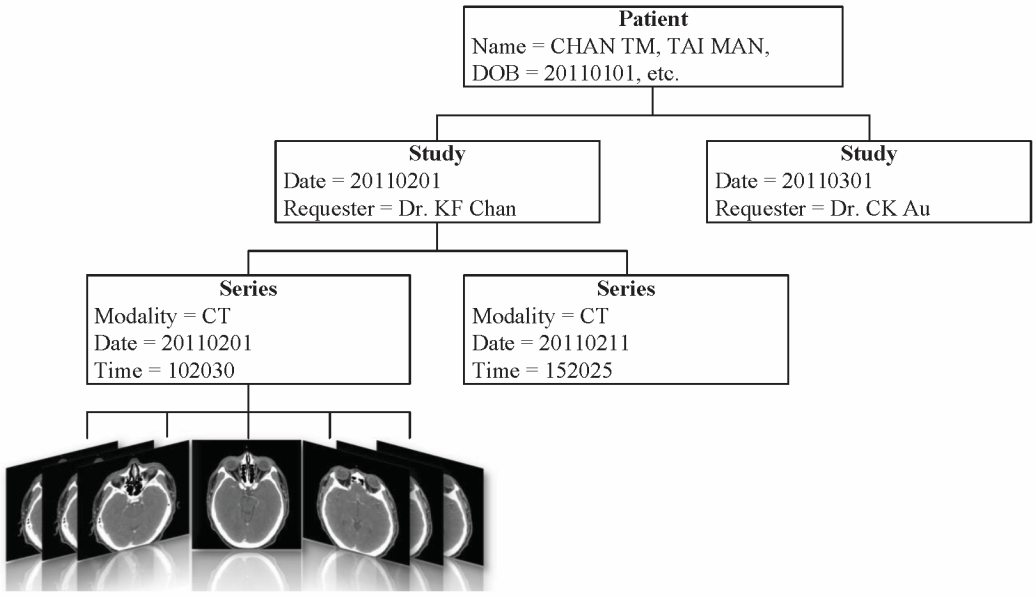

Figure 3.1. Basic DICOM hierarchical data model.

DICOM specifies the set of Information Object Definitions (IODs) which describe the content and functions of the real-world objects (Foord, 2001; Mildenberger et al., 2002). It defines the multiplicity of each attribute and specifies whether that attribute is mandatory or conditional. Each IOD consists of several information entities, where each information entity contains one or multiple modules to group certain attributes that logically related.

A DICOM attribute is composed of four fields: a data element tag, a value representation field, a value length field and a value field (Bidgood and Horii, 1992; Prior, 1993). Table 3.1 lists some examples of DICOM attributes. The data element tag consisting of group and element hexadecimal numbers can uniquely identify the element. The two-letter value representation describes the data type and format of the attribute's value. There are 27 explicit value representation defined in the Part 5 of the DICOM standard corresponding to dates, times, names and so on. For instance, the DICOM tag (0010,0020) corresponds to a

patient identifier with a value representation of long string. The first two bytes (0010) represent the group tag and the second two bytes (0020) represent the element tag. The maximum length of a long string is limited to 64 characters. A value length indicates the length of the attribute's value and a value field contains the attribute data.

Table 3.1. Examples of some DICOM attributes.

Attribute Name	Tag	Value Representation (VR)	Value Length	Value Field
PatientName	(0010,0010)	PN	64 chars maximum per component group	CHAN TM. TAI MAN
PatientID	(0010,0020)	LO	64 chars maximum	RTA01-1234
PatientsBirthDate	(0010,0030)	DA	8 bytes fixed	20110101

All information objects are classified into two types: normalized and composite. A normalized information object represents attributes that are inherent in a single, real-world entity (Huang, 2010; Roberson and Shieh, 1998; Riddle and Pickens, 2005). For example, the study date and time are attributes of the study information object because they are inherent whenever the study is performed. On the other hand, a composite object combines two or more normalized information objects to facilitate operations. An example of a composite information object would be the CT Image information object which contains attributes from the patient information object (patient's name, ID, etc.) and the CT image information object (image date, time, etc.).

3.2 DICOM and its utilization in radiology

With burgeoning image management needs in radiology, Huang et al. (1988) pioneered in designing PACS tailored for easy access and economical storage of

medical images. With its flexible and open architecture, DICOM is the communication protocol implemented in PACS (Gale et al., 2000; Hsiao et al., 2005; Mongkolwat et al., 2005). By uniquely indexing all the tagged data in DICOM objects, a vast treasure-trove of information gathered in the databases could be accessed in efforts to improve clinical practice and benefit patient care (Kamauu et al., 2006; Wang et al., 2011).

The widespread availability of PACS with the vast amount of data from the digital images helped fuel the explosive growth of computer-aided detection (CAD) schemes for detection and differentiation of lesions on digital images. Some investigators have been working dedicatedly on the development of CAD system for detection and differential diagnosis of various lesions (Doi 1999; Doi 2004; Doi 2007; Li et al., 2008; Li et al., 2010; Romero et al., 2011; Sung et al., 2011; Jacobs et al., 2011; Shiraishi et al., 2011). Image analysis techniques including edge detection, image segmentation and image filtering were employed to improve the image quality and the diagnostic outcome (Nakayama et al., 2007; Shiraishi et al. 2008; Levman and Martel, 2011).

In recent years, there has been growing interest in mining DICOM data. Various electronic teaching files were created by harvesting interesting cases from the database for education, clinical and research purposes (Ernst et al., 2002; Lim et al., 2003; Kamauu et al., 2006). To support clinical decision-making, computed aided bone age assessment using a digital hand atlas was also reported (Pietka et al., 2003; Gertych et al., 2007; Tang et al., 2011). With the increase in public awareness about medical radiation exposure, some DICOM data mining systems were developed to calculate and monitor the radiation dose delivered by different

medical imaging systems (Stewart et al., 2007; Wang et al., 2011). Useful information such as examination protocol and dose information could be parsed out by matching the relevant DICOM tags. Without compromising the image quality, these evidence-based quality assurance processes could effectively reduce the radiation dose by half (Stewart et al., 2007).

3.3 DICOM RT objects

In 1997 and 1999, the DICOM standard committee extended DICOM for RT application with the ratification of seven DICOM RT objects, thereby facilitating data transmission and storage of radiotherapy images and related information in a multi-vendor environment. RT Structure Set, RT Dose, RT Plan, RT Image, RT Beams Treatment Record, RT Brachy Treatment Record and RT Treatment Summary Record are officially defined by the DICOM standard.

3.3.1 RT Structure Set

The RT Structure Set object is defined for the contouring of structures or region of interest (ROI) such as tumor volume and organs at risk (OARs). It contains a collection of contour points for ROIs and points of interest. It addresses the requirements for transfer of patient structures and related data. The target volumes and nearby OARs defined in accordance with the guidelines in ICRU Reports 50 and 62 are associated with reference CT images. Each ROI is uniquely identified with an ROI number.

3.3.2 RT Dose

The RT Dose object is defined for dose related attributes such as isodose curves,

DVH, reference points. It contains dose data generated by a treatment planning system and supports the transfer of dose. To correctly associate a dose distribution with a structure, each DVH is specified by the ROI number in the RT Structure Set. The isodose contour level is displayed in either percentage or absolute dose with co-registered CT images overlay. The RT Dose, RT Structure Set and the DICOM CT images are commonly put in the same frame of reference.

3.3.3 RT Plan

The RT Plan object is defined for textual information related to treatment parameters, fractionation scheme, prescription, machine information, treatment setup etc. It is used for transfer of treatment plan generated by manual entry, a simulation workstation or a treatment planning system. Information from RT Plan could be represented on the RT Structure Set and a CT scan.

3.3.4 RT Image

The RT Image object to a certain extent is similar to the Image Object in radiology. It contains radiotherapy images acquired or calculated using a conical imaging geometry such as digitally reconstructed radiographs, simulation images, and portal images and addresses the requirements for image transfer. Unlike DICOM images, additional RT-specific characteristics of a projection image like isocenter position, distance from source to imaging plane and beam limiting device openings can be found.

3.3.5 RT Treatment Record

The RT Treatment Record object is further divided into three objects, namely RT Beams Treatment Record, RT Brachy Treatment Record, and RT Treatment Summary Record. It consists of historical record of all treatment data. The RT Plan and RT Treatment Summary Record are retrieved and reviewed by Accelerator Treatment Console prior to every treatment. If the previous session is incomplete, the RT Beams Treatment Record could be loaded to resume the interrupted treatment. The RT Brachy Treatment Record includes all treatment data acquired during the course of brachytherapy.

3.4 DICOM RT and its utilization in oncology

Along with DICOM, DICOM RT standard has been widely implemented in oncology and become mandatory requirements for all new RT modality purchases. Like DICOM, the most fundamental and primary level of DICOM RT deals with exchanging, archiving and retrieving objects (Law, 2005). With the ever increasing popularity of PACS, DICOM standard enables the integration of network hardware from multiple vendors into a PACS (Law and Huang, 2003). Its open architecture could provide amazing application flexibility, arousing intense research interest. Graves et al. (2007) designed a DICOM-based software to assist in defining metabolically active tumor volumes in positron emission tomography making molecular imaging-guided radiation therapy a reality. As a common platform for RT data exchange and expert consultation, Law et al. (2009) developed a DICOM-based RT electronic patient record to improve the continuity of patient care and facilitate more efficient workflow. Efforts have been devoted to make data mining tool a powerful complement to the electronic

patient record system for clinical decision support and outcome analysis (Le et al., 2011). By exchanging data with treatment planning system via DICOM RT files, Yang et al. (2011) established a software toolkit dedicated for adaptive radiotherapy which brought deformable image registration algorithm closer to RT applications.

3.5 DICOM RT and its utilization in IMRT planning

In order to boost the IMRT productivity, these DICOM RT objects were seamlessly integrated in the IMRT planning workflow (Law and Liu, 2009). Figure 3.2 illustrates the radiation therapy workflow. Firstly, planning CT images are sent as DICOM image objects to the treatment planning system for radiation field planning (step 1). Next, the oncologists are asked to accurately define the targets and OARs on fused multimodality images. Together with the body contour, the outlines of targets and OARs are saved as DICOM RT Structure Set objects in the treatment planning system. Upon completion of optimization and dose calculation, a clinical treatment plan is created including DICOM Image, DICOM RT Structure Set, DICOM RT Plan and DICOM RT Dose objects (step 2). After plan review and approval by oncologists, the anatomic contours, the associated plan containing beam geometry information, and the reference digitally reconstructed radiographs for treatment verification are sent to the radiation oncology information system as DICOM RT Structure Set, RT Plan and RT Image objects, respectively (step 3). Just before treatment, the DICOM RT Plan and RT Summary Record are retrieved by the Accelerator Treatment Console (step 4 and step 5). During the course of treatment, the RT Beam Record object including the details of each delivered treatment session together with the

RT Image object containing all verification images acquired are generated and sent to the radiation oncology information system (step 6 to step 8).

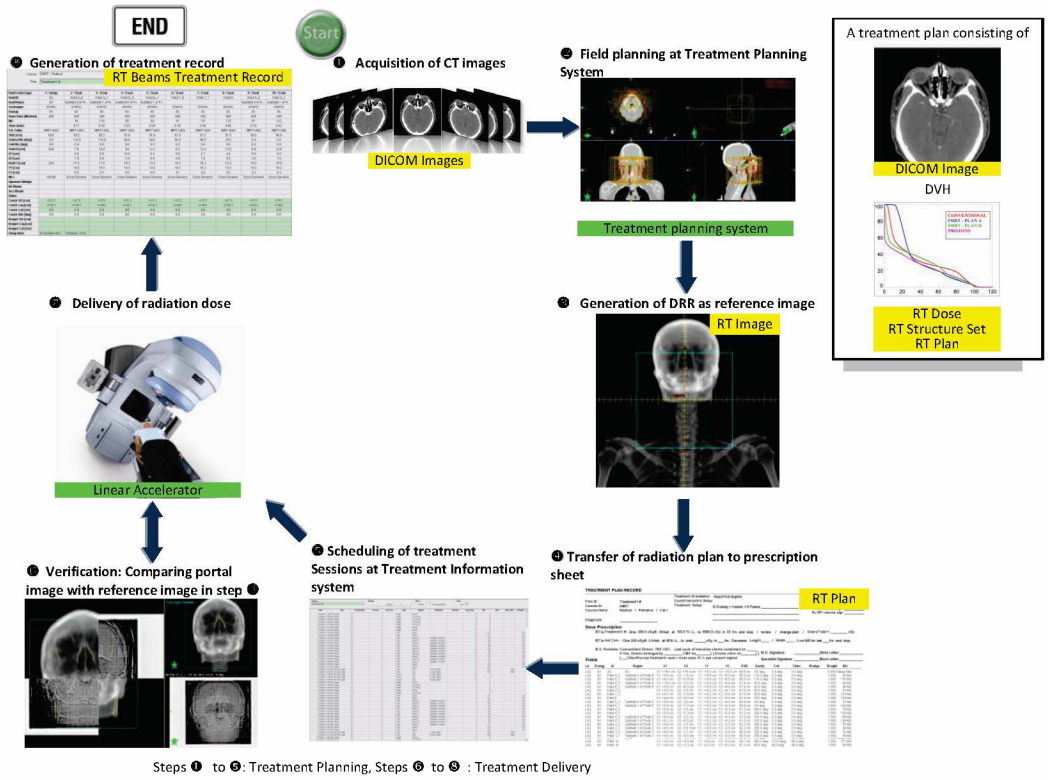

Figure 3.2. Chart illustrates radiation therapy workflow.

3.6 Development of DICOM-based CAE system with a personalized conformity index

Despite the fact that DICOM RT standard has been successfully implemented in oncology, its applications are largely limited to data transfer and storage. Research in mining the DICOM RT data has so far been scanty. Taking full advantage of this open standard, the DICOM-based computer-aided evaluation (CAE) system could potentially be designed to facilitate remote plan evaluation across multiple locations. A two-dimensional conformity index with dose and distance incorporated (CI_{DD}) could also be developed and integrated in the CAE

system to quantify the IMRT plan quality. Various DICOM RT modules together with their attributes required for creating the CAE system with CI_{DD} are introduced in this section.

In the DICOM RT Structure Set module, the **`StructureSetROISequence`** attribute assigns a unique ROI number to each ROI (Figure 3.3). The outline of each ROI is defined in the Contour Data within the **`ROIContourSequence`** attribute containing a collection of contour points.

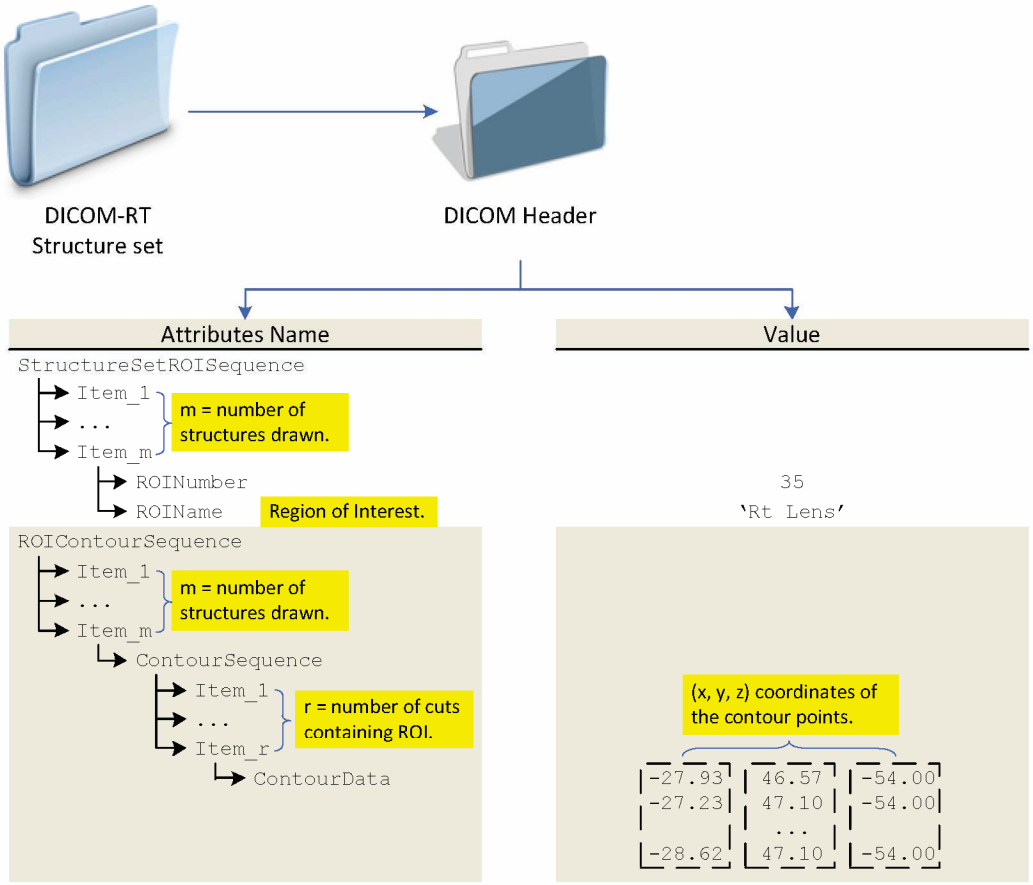

Figure 3.3. Attributes of RT Structure Set module required for development of the CAE and CI_{DD} systems.

Figure 3.4 shows the necessary attributes of RT Dose module for creating the CAE and CI_{DD} systems. Following the reconstruction of region of interest

contours, the grid doses could be constructed by multiplying each pixel value stored in the Image pixel module with the **`DoseGridScaling`** attribute in the RT Dose module. Next, the 3D RT Dose matrix and the region of interest contours could be mapped onto the CT data set according to the coordinates of the **`ImagePositionPatient`** attribute of the RT Dose module and the CT image.

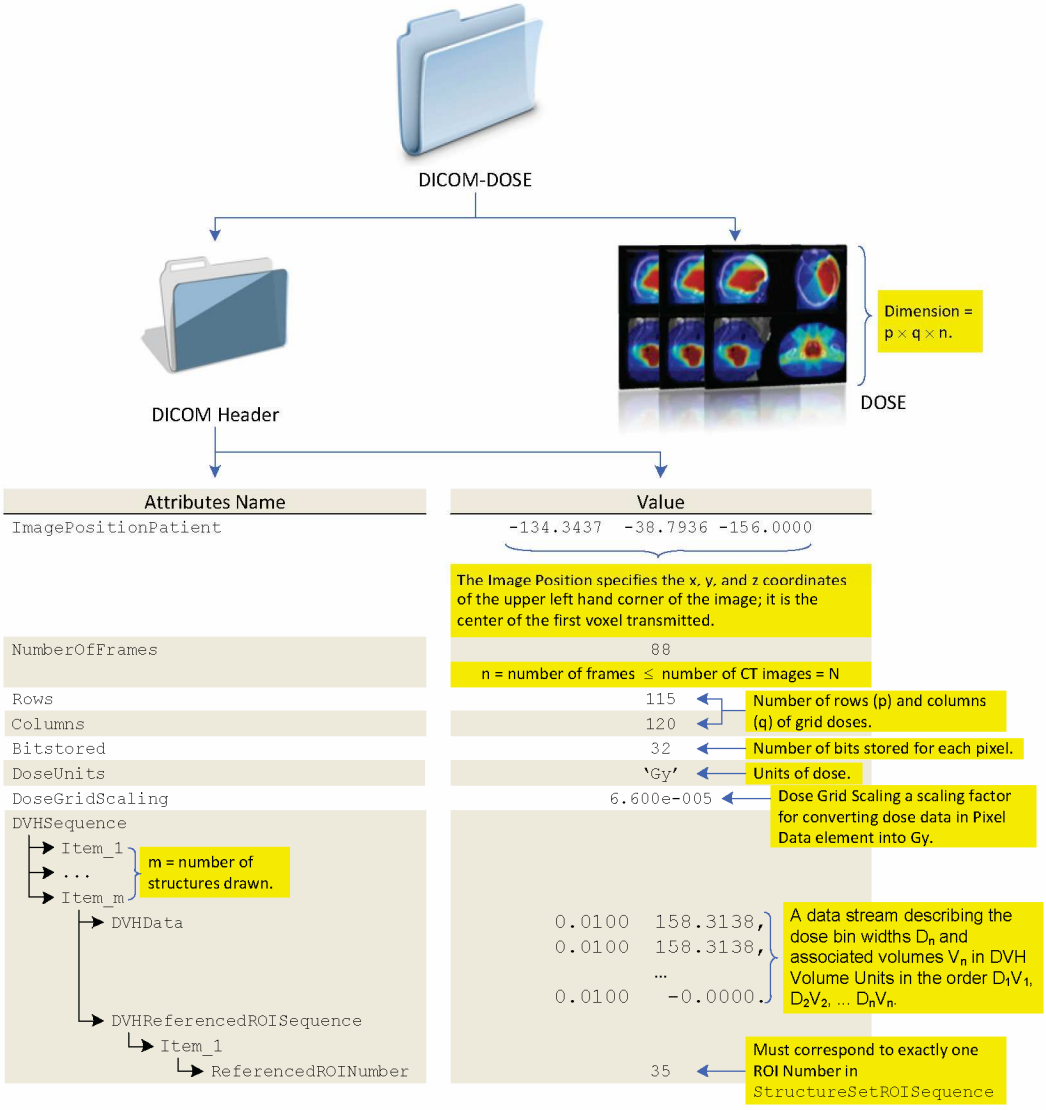

Figure 3.4. Attributes of RT Dose module required for creating the CAE system with CI_{DD}.

As shown at the bottom of Figure 3.4, the Referenced ROI Number within the **`DVHReferenceROISequence_Item1`** provides a cross-reference to the

`StructureSetROISequence` attribute in the DICOM Structure Set module. With reference to this Reference ROI Number, specific DVH could be created by extracting the corresponding DVH data from the `DVHSequence` attribute.

With these basic concepts in mind, more details will be given in the next chapter to further elaborate on the methodologies used in this study.

Chapter 4 Methodology

This study aimed at developing a computer-aided evaluation system (CAE) and a personalised conformity index (CI). The former was for the evaluation of treatment plans generated from the treatment planning systems. The latter was for further discerning the quality of treatment plans so as to help oncologists to make decision on which plan to adopt for IMRT. These two components were integrated in an attempt to provide a one-stop software platform for automatic evaluation of IMRT plans for head-and-neck cancer.

4.1 Development of computer-aided evaluation (CAE) system

The spiral model defined by Boehm (1988) formed the basis for the CAE system development. It allows incremental refinement. As shown in Figure 4.1, each cycle of the spiral goes through four phases, namely planning, risk analysis, engineering and evaluation.

1. Planning phase aims to carefully decide and clearly document the desired outcomes and goals of CAE system development.
2. Risk analysis phase attempts to identify all possible risks and plan corrective actions to mitigate the risks.
3. Engineering phase is to carry out the actual software development.
4. Evaluation phase aims to assess the software design and quantify its potential for improvement.

The design process moves around the spiral in a clockwise direction, starting at the center with an idea. In the spiral model, the radius of the spiral represents the cumulative cost and the angular dimension component represents the progress.

Each subsequent spiral builds on the baseline spiral producing prototypes of aging increasing complexity.

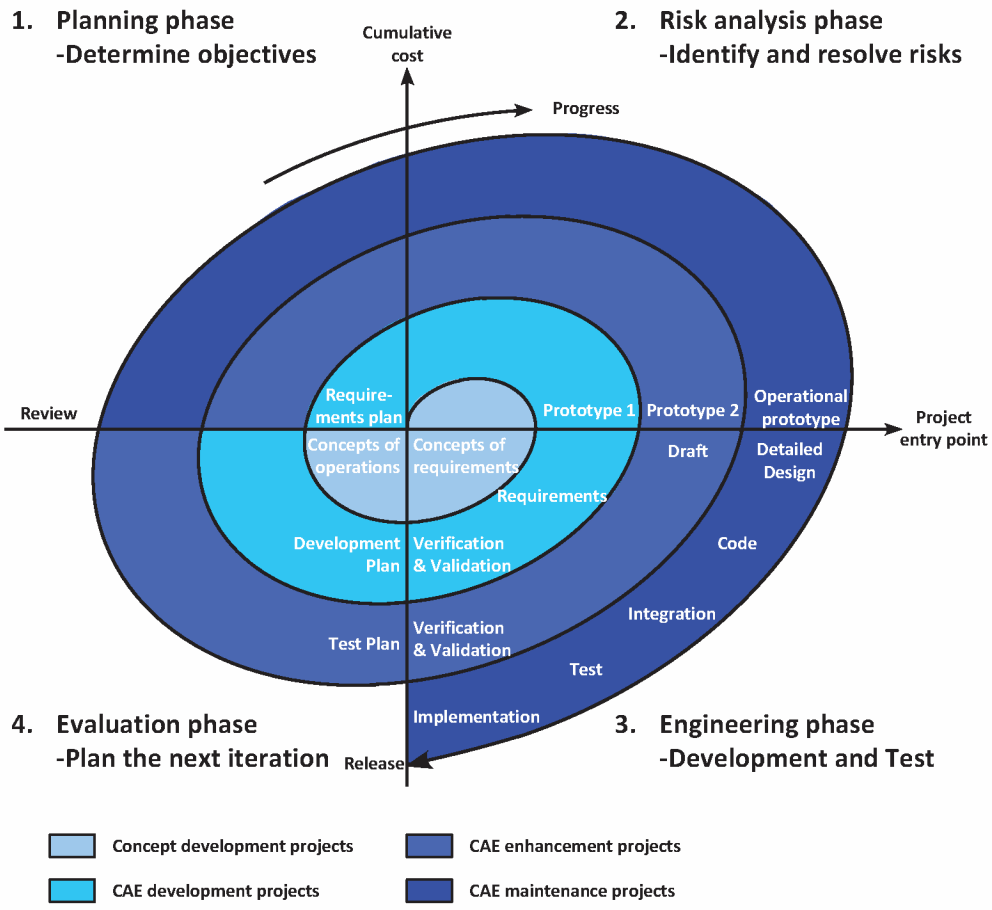

Figure 4.1. Spiral model for CAE system development.

4.1.1 Planning phase

Each cycle in the spiral model starts with the determination of objectives and development of the project plan. In software planning phase, workflow models are valuable in understanding current operational process, identifying system requirements, visualizing the benefits after system implementation and defining the desired future situation. The goal of this CAE system was to develop an automatic IMRT plan evaluation system for controlling and maintaining a desired

level of plan quality for head-and-neck cancer. When such objective was set, the traditional IMRT plan evaluation process was firstly reviewed to pinpoint the existing shortcomings so that changes required could be incorporated into the system

Conventional IMRT plan evaluation process requires human inspection of violation of treatment protocols. The prescribed goals of an IMRT treatment plan are often expressed in terms of dose volume constraints. The DVH statistics for each target and OAR should be extracted manually and checked for compliance against specific constraints. If the results are unsatisfactory, it is necessary to visually inspect the isodose distributions on every single slice containing the corresponding structures. Moreover, the existing quantitative indices for plan quality comparison are generally oversimplified which could lead to false conclusion. In an attempt to eliminate these tedious manual processes, the clinical oncology departments are looking for an efficient automated solution for IMRT plan evaluation.

After the review of workflow, the objectives incorporated into the CAE system were:

1. To develop an algorithm for detection of violations of plan protocols.
2. To design the CAE system architecture with three components including

    i. The algorithm for detection of violations of plan protocols.
    ii. The knowledge base providing information on overdose and underdose regions.
    iii. Multiple graphical user interface (GUI) panels.

3. To design multiple GUI panels for

    i. Inputting DICOM image and DICOM RT objects for data mining.
    ii. Setting of dose-volume acceptance criteria for query formulation.
    iii. Displaying IMRT plan evaluation results after going through the software algorithm (1 above) to indicate violations of plan acceptance criteria for head-and-neck cancers and provide side-by-side display of DVHs and specific CT images with hot and cold spots.

4. To develop a personalized conformity index for objective comparison of IMRT plans for head-and-neck cancer.

4.1.1.1 Hierarchical bottom-up searching design

Choosing an appropriate organizational structure is crucial to the success of the system development planning. After tracing the clinical workflow, it was recognized that there was a vast amount of CT data to be handled in the CAE system. Each head-and-neck cancer patient being treated with IMRT must undergo a planning CT scan of the area of interest consisting of more than 100 slices. To allow efficient query processing over the massive image database, a hierarchical four-layered bottom-up approach was adopted. By breaking the ultimate goal down into more detailed subgoals, the process ran in an upward direction towards the top of pyramid. The starting point for constructing a hierarchy was a comprehensive list of the tasks that made up a job. After identifying hierarchical relationship amongst the tasks, sequential instructions were executed in a bottom-up manner.

As shown in the Figure 4.2, the searching of CT images with violations was decomposed into four subtasks. The hierarchical analysis started with the complete set of CT images by examining the presence of structure contours. With reference to the `ROIContourSequence` attribute in RT Structure Set (in the DICOM standard), images containing OARs and PTVs were categorized as "CT images with OARs" or "CT images with PTVs" respectively. Pruning technique was then employed to progressively narrow down the search. Depending on whether OAR overdose or PTV underdose was present, a specific subset of images were evaluated and searched for pertinent CT slices with violations. This hierarchical structure aimed at providing quick access to query results and easy navigation of detailed information.

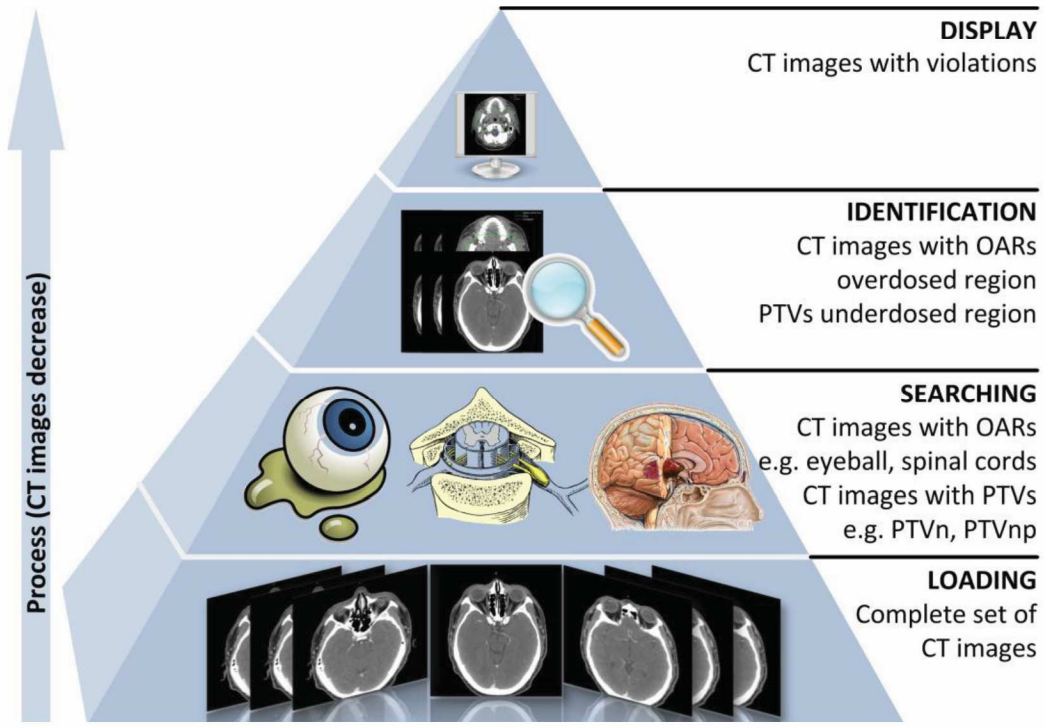

Figure 4.2. Hierarchical bottom-up searching approach.

To allow planners to query for overdose or underdose regions, multiple GUIs were then created using the MATLAB version 7.12 (R2011a) (The MathWorks, Inc., Natick, MA, USA). Using the GUIs, the planner could modify the plan acceptance criteria and keep them up to date. The GUIs were task-oriented and treatment region-dependent, supporting both user input and output display.

4.1.2 Risk analysis phase

The spiral software development model is an incremental and risk-driven approach, addressing the need for risk management and early proof-of-concept (Boehm, 1988). The second phase, known as risk analysis, is intended to recognize and resolve all the possible risks by the repeated use of prototypes at each revolution of spiral. As shown in Table 4.1, a risk management checklist was used as a means of identifying and controlling risks in the CAE system development. The major risk items identified in this study were real-time performance shortfalls, continuous refinement of clinical protocols and software malfunction. The corresponding risk-management techniques were developed with small proof-of-concept prototypes. For example, hierarchical bottom-up searching model was employed to avoid lengthy system response time.

Table 4.1. Risk management checklist.

Possible risk items	Risk management techniques
Real-time performance shortfalls due to massive image database	Design of hierarchical bottom-up searching (Refer to section 4.1.1.1)
Continuous refinement of clinical Protocols	Design of graphical user interface (GUI) supporting formulation of personalized plan acceptance criteria (Refer to section 4.1.3.4)
Software malfunction due to wrong scripts, poor GUI design	Technical verification and performance evaluation (Refer to section 4.1.4)

4.1.3 Engineering phase

In the engineering phase of the spiral model, the actual system is developed in a series of incremental releases. Continuous efforts had been made to the design, coding, implementation and verification of the next-level product along the way.

4.1.3.1 Data flow model

As a blueprint for system construction and composition, the data flow was designed to specify the execution sequence of activities and illustrate how different data types could be integrated into the CAE system. The development of the CAE system should have the following input/output features:

Input data

1. A data set from one head-and-neck cancer patient, shown in Table 4.2, including the following items was sent from the treatment planning system and loaded into the CAE system.

Table 4.2. Number of objects from one patient.

Data Types	Number of objects
CT images (512 × 512 × 12) bits	Several dozens to hundreds
DICOM RT Dose	Less than or equal to number of CT images
DICOM RT Structure set	1

The GUI for importing DICOM and DICOM RT objects was developed to import the data file and perform anonymization. For effective and efficient data access, all DICOM and DICOM RT objects collected for each patient data set were grouped and stored into the same subfolder. A search engine was built for automatic extraction of the necessary data from the DICOM RT objects. For example, the Contour Data within the `ROIContourSequence` attribute should be extracted from the DICOM RT Structure Set module for reconstruction of region of interest contours.

2. Specific dose-volume acceptance criteria for each target and OAR were input and saved as a template for future use. All OARs and targets in the head-and-neck regions were listed on the input data panel allowing formulation of plan acceptance criteria and query of specific knowledge (Table 4.3). Planners could either enter the dose and volume parameters in

the corresponding fields or open an existing template and modify it if necessary.

Table 4.3. Examples demonstrating formulation of plan acceptance criteria.

Regions of Interest (ROIs)	**Dose (Gy)**	**Volume (%)**
Brainstem	54	0
Brainstem + 3mm shell	60	1
Spinal Cord	45	0
Spinal Cord + 3mm shell	50	0
Temporal lobes	70	0
Optic chiasm	54	0
Optical nerves	54	0
Parotid gland	26	50
PTV_{np70} and PTV_{n70}	70	95
PTV_{np70} and PTV_{n70}	66.5	100
PTV_{np66} and PTV_{n66}	66	95
PTV_{np66} and PTV_{n66}	62.7	100
PTV_{np60} and PTV_{n60}	60	95
PTV_{np60} and PTV_{n60}	57	100

Abbreviations: PTV_{np} = nasopharyngeal planning target volume; PTV_{n} = nodal planning target volume; PTV_{np70} = 70 Gy to PTV_{np}; PTV_{n70} = 70 Gy to PTV_{n}; PTV_{np66} = 66 Gy to PTV_{np}; PTV_{n66} = 66 Gy to PTV_{n}; PTV_{np60} = 60 Gy to PTV_{np}; PTV_{n60} = 60 Gy to PTV_{n}.

Output data

1. Statistical analysis plots known as DVHs were necessary for quantitative plan evaluation by summarizing the three dimensional dose distribution data for each structure in a graphical format. The CAE system could reconstruct the cumulative DVH for a region of interest by summing up all differential voxels in a given dose range and plotting this volume as a function of dose (Figure 4.3). DVH could be reviewed by navigating along the DVH curve to explore the dose-volume relationship within a volume of interest and compare against the plan acceptance criteria. Descriptive statistics including mean, median, standard deviation, maximum and minimum doses were calculated for each region of interest which were useful in quantifying relative plan quality.
2. Overdose regions in normal tissues and underdose regions within target volumes were uncovered by automatic visualization of the sizes and exact locations of hot and cold spots on each individual CT slice. The DVH curve was directly linked to the pertinent CT slices containing the violations for better evaluation of complex plans, as illustrated in Figure 4.4.

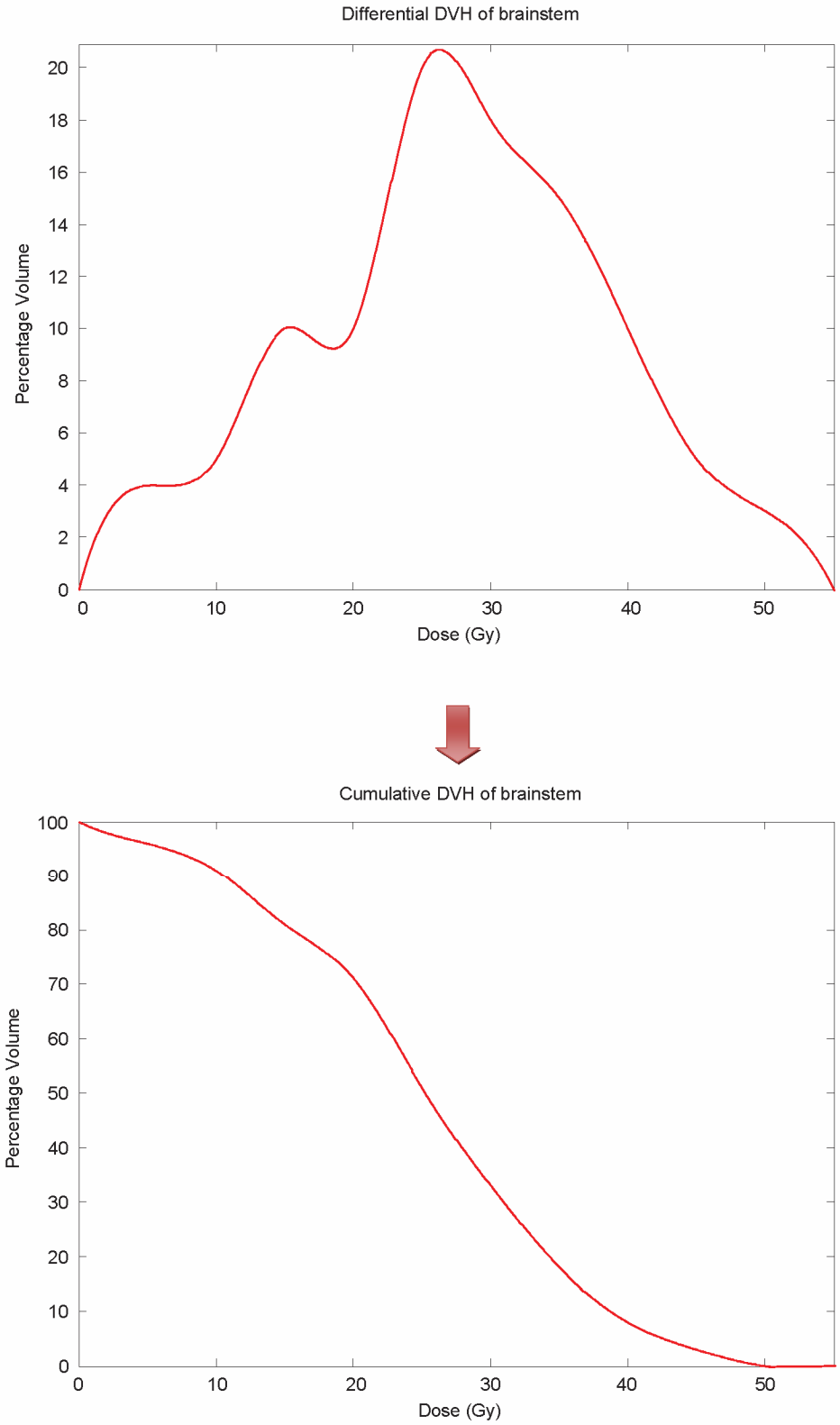

Figure 4.3. Conversion between differential DVH and cumulative DVH of brainstem.

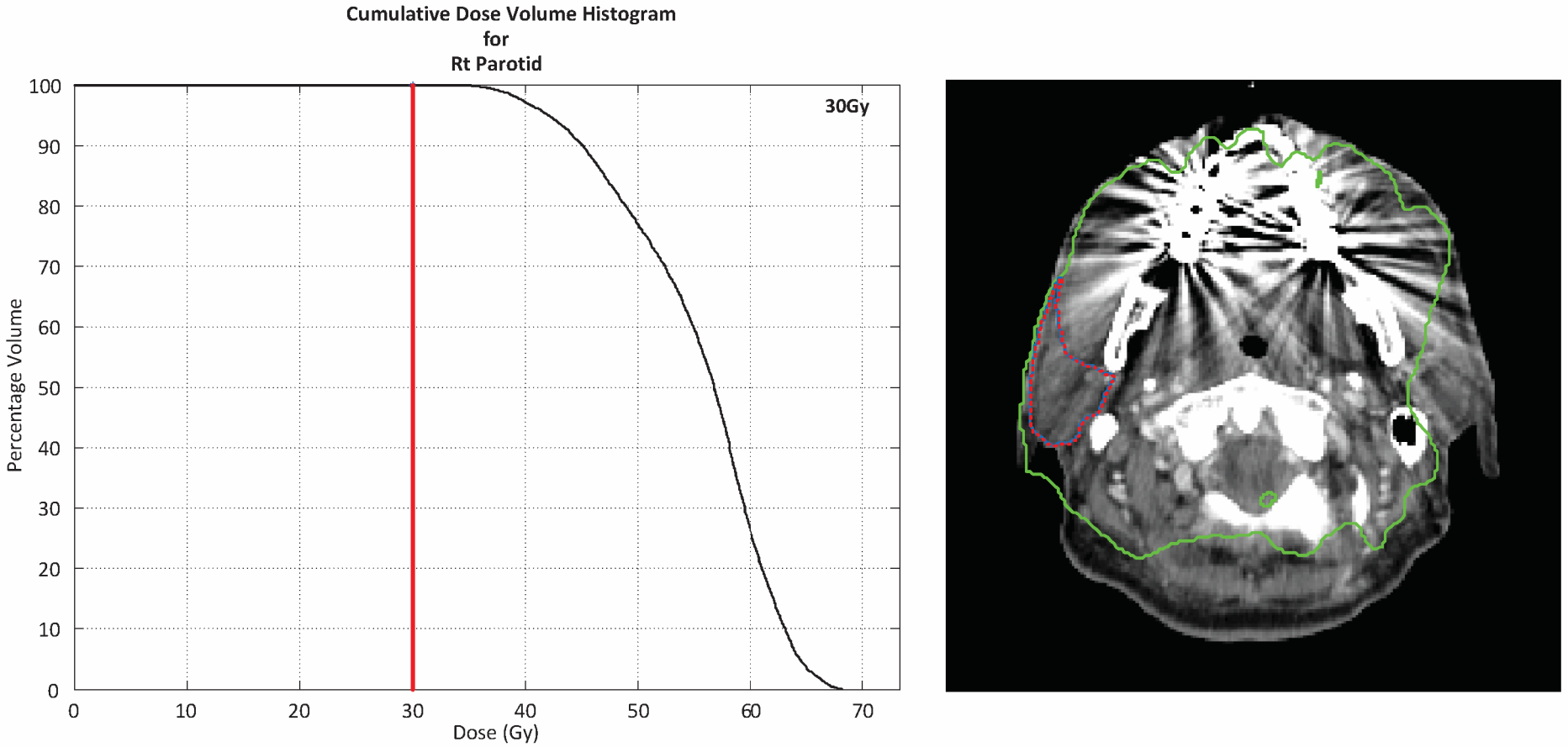

Figure 4.4. Evaluation results showing the relationship between DVH and pertinent CT image containing violation.

3. The areas of each hot and cold spot were computed and displayed on individual CT slice. By adjusting the dose values along the horizontal axis of the DVH curve, it provided the interactive display of the overlapping and non-overlapping area between each region of interest and the corresponding isodose level.
4. A personalized target conformity index along with RTOG conformity index, healthy tissues conformity index (HTCI), conformation number (CN) and target coverage factor were generated using the DVHs of the PTVs for plan evaluation and comparison. These concepts will be discussed in depth later in Section 4.2.

4.1.3.2 Algorithm for detection of protocol violation

At the first stage of violation detection, DVHs were useful in summarizing dose distribution data in a linear graph model to allow rapid screening of treatment plans. Each region of interest was uniquely defined by `StructureSetROISequence` attribute in RT Structure Set with a `ROInumber` attribute as shown in Table 4.4. For example, the `ROInumber` attribute for the right lens was 35. By cross-referencing this number with `DVHReferenceROISequence.Item1.ReferencedROINumber` attribute in RT Dose object, the corresponding item number for the right lens was found to be 26. Based on this item number, DVH of the right lens was reconstructed by extracting data from `DVHData` attribute in RT Dose object.

Table 4.4. Cross reference table between Structure set module and RT DVH module.

RT STRUCTURE: StructureSetROISequence			RT DOSE: DVHSequence	
Item No.	**ROINumber**	**ROIName**	**ReferencedROINumber**	**Item No.**
18	25	GTVnp	25	16
22	28	Lt Eye	28	19
29	35	Rt Lens	35	26
36	44	PTVnp70	44	32

To generate the DVH for a structure, the defined volume of region of interest was partitioned into voxels. Dose for each voxel was then calculated and accumulated in the appropriate dose bin of the histogram. The ordinates for each point on the cumulative DVH curve represented the total volume of region of interest that received at least the given dose indicated on the horizontal axis. Assuming the maximum lens dose was constrained at 6Gy, Figure 4.5 demonstrates how to directly read off the corresponding value represented by DVH.

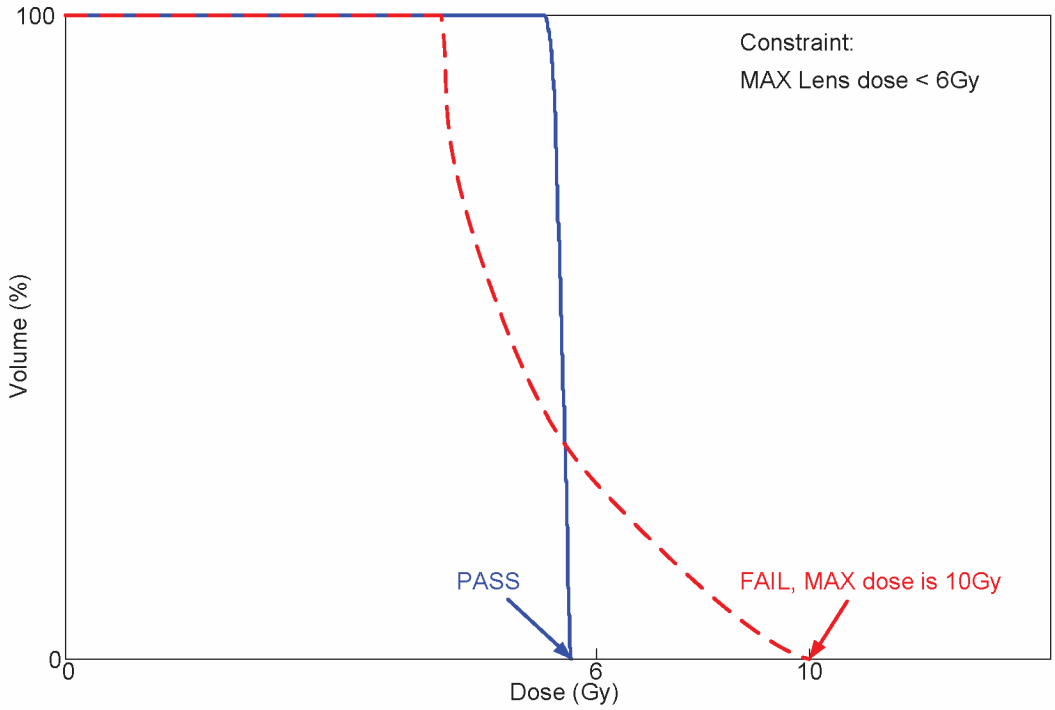

Figure 4.5. Cumulative DVH curves for the right lens of two plans.

The plan represented by the solid line satisfied the constraint with the maximum dose just below 6Gy. Conversely, another plan represented by the dashed line resulted in unacceptable dose distribution. The maximum dose was 10Gy, violating the planning goal. If any of the constraints were not met, detailed slice-based evaluation of isodose coverage was required. The CT slice revealed that a sizable fraction of the right lens received dose exceeding the specified limit, a situation that warranted a modification of treatment plan due to unnecessary damage to vision (Figure 4.6).

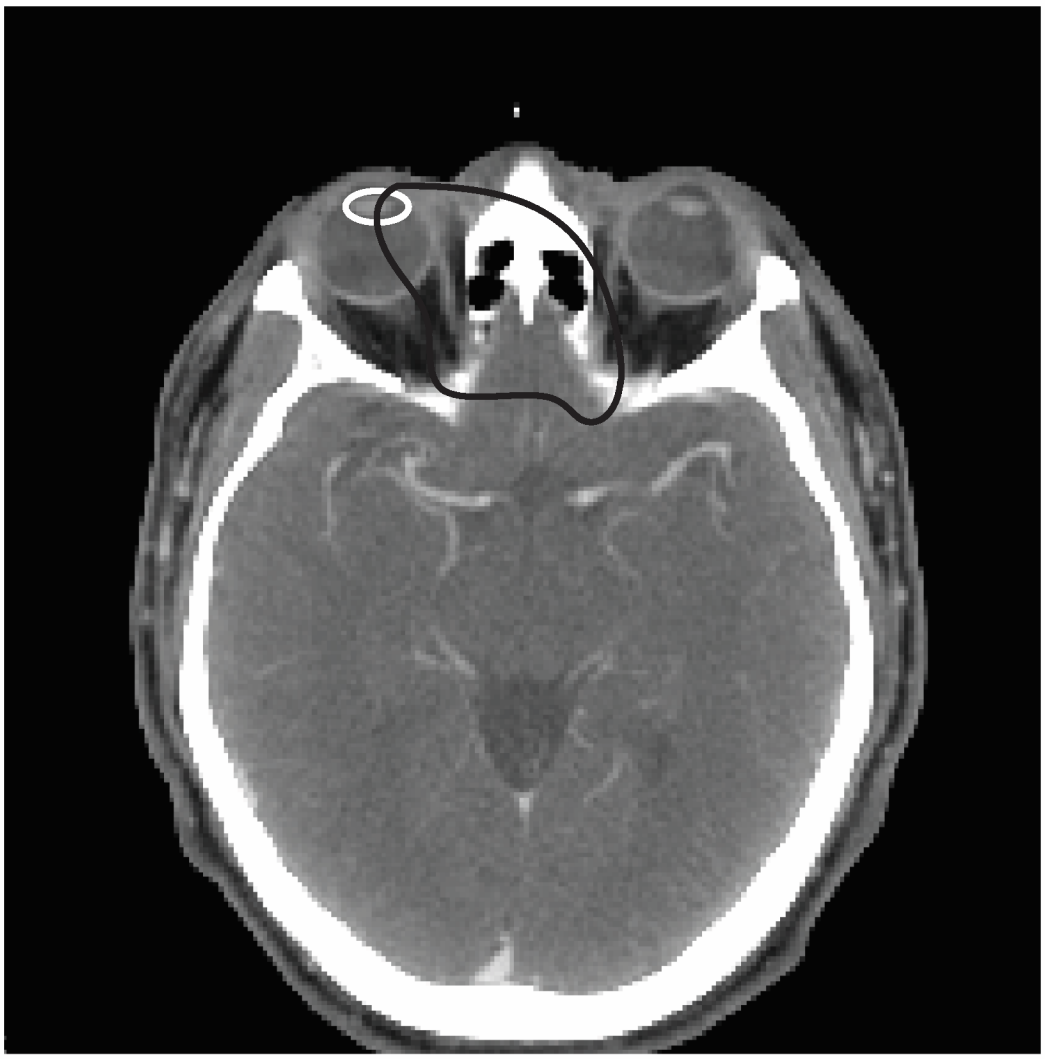

Figure 4.6. The right lens contour and 6Gy isodose line superimposed on the CT image.

As well as OAR sparing, PTV coverage was also used as a criterion for

evaluation. The ideal cumulative DVH for a target volume should appear as a horizontal line at 100% volume on the ordinate with a vertical drop at the prescribed dose on the horizontal axis. In clinical reality, 100% volume of PTV at the prescribed dose can rarely be achieved. Instead, PTV volume coverage of at least 95% is generally prescribed. The adequacy of target coverage could be evaluated by the shape of DVH. As illustrated in Figure 4.7, the plan represented by the solid line achieved acceptable target coverage with 95% volume of the PTV receiving at least 70Gy. On the contrary, the other plan represented by dashed line failed to meet the minimum requirement. Only 83% volume of the PTV was adequately covered as prescribed. To have a clear understanding of spatial locations of the undesirable hot and cold spots in PTV, it was still necessary to review the isodose distribution.

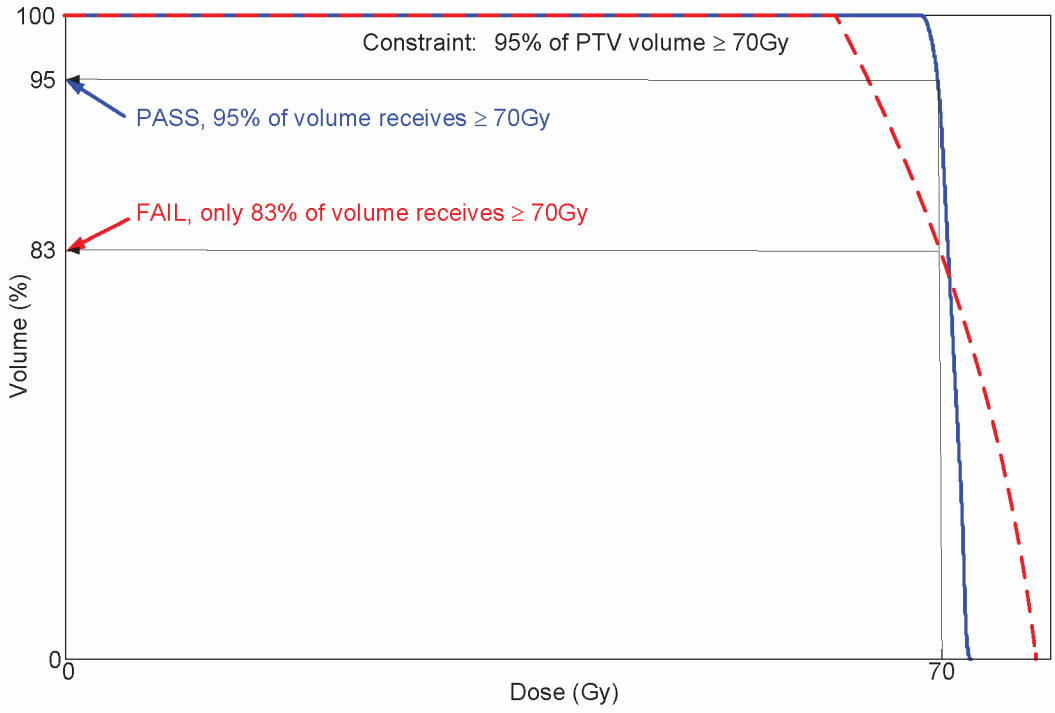

Figure 4.7. Cumulative DVH curves for the PTV of two plans.

4.1.3.3 Overdose and underdose regions extraction

Once the 3D dose distribution of an IMRT plan was calculated and ready for evaluation, the corresponding RT Structure Set, RT Dose objects together with a series of planning CT images were exported from the treatment planning system and loaded into the CAE system (Figure 4.8). With the aim of improving tumor control while decreasing normal tissue complications, either underdosing (cold spot) within tumor or overdosing (hot spot) was undesirable. The quality of each treatment plan was critically evaluated before being implemented. With respect to specific dose volume criteria, the DVH statistics for each region of interest should be evaluated separately. In order to examine the anatomic location and extent of hot and cold spots, the CT slices containing violations were searched by the programme and displayed.

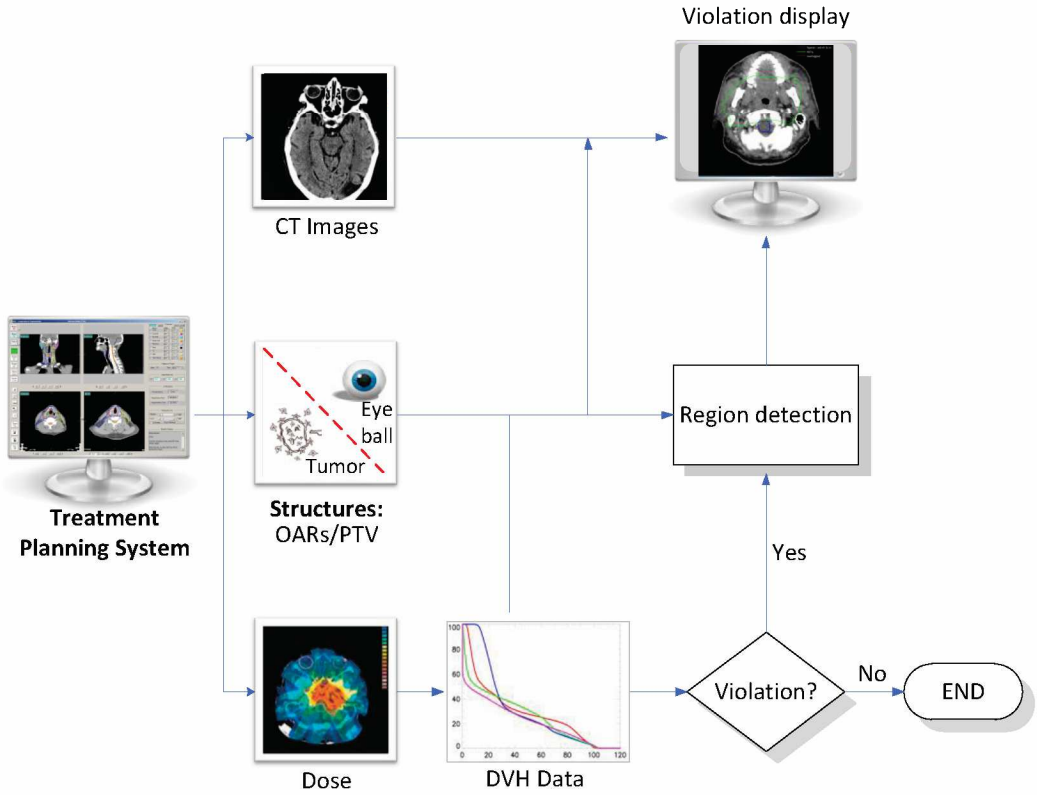

Figure 4.8. Region extraction model based on the concepts of DICOM and DICOM RT objects.

Extraction of both overdose and underdose regions was based on the edge-based approach. First of all, the boundary of the specified isodose line and region of interest contour were plotted respectively. To reconstruct the outline of a structure, the system made use of the contour data stored in the RT Structure Set object. With the same frame of reference, each region of interest was associated with reference to CT images.

Since dose values were described as pixel data elements, grid doses in specified dose units were reconstructed by multiplying each pixel value stored in the Image pixel module with the `DoseGridScaling` attribute in the RT Dose module of the RT Dose IOD. As shown in Figure 4.9, the voxel coordinates of RT Dose matrix with reference to CT images were found in the patient coordinate system as defined in the CT scans. For example, an axial head CT image set consisted of N images of 512×512 pixels whereas the RT dose matrix size was typically smaller containing n images of $p \times q$ pixels. The most inferior CT slice with RT Dose matrix, k^{th} cut, was specified in the z-coordinate of the `ImagePositionPatient` attribute in the RT Dose object.

Step (a): Loading complete set of CT images

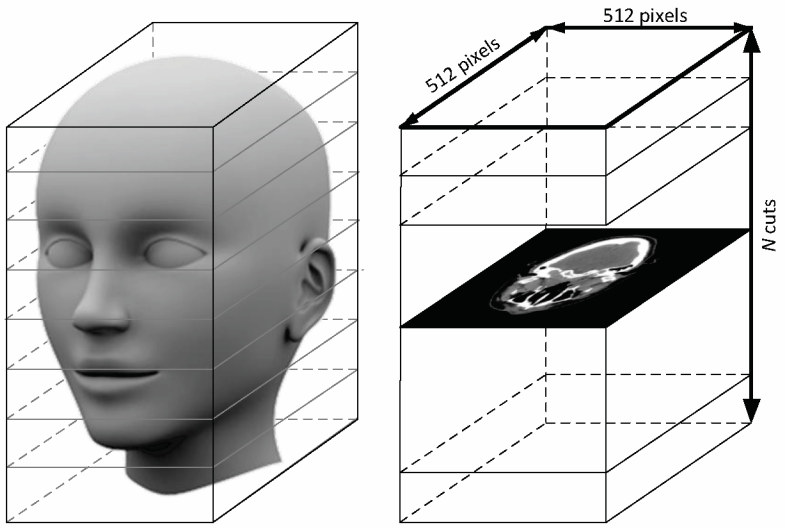

Step (b): Vertical Alignment, finding the common reference

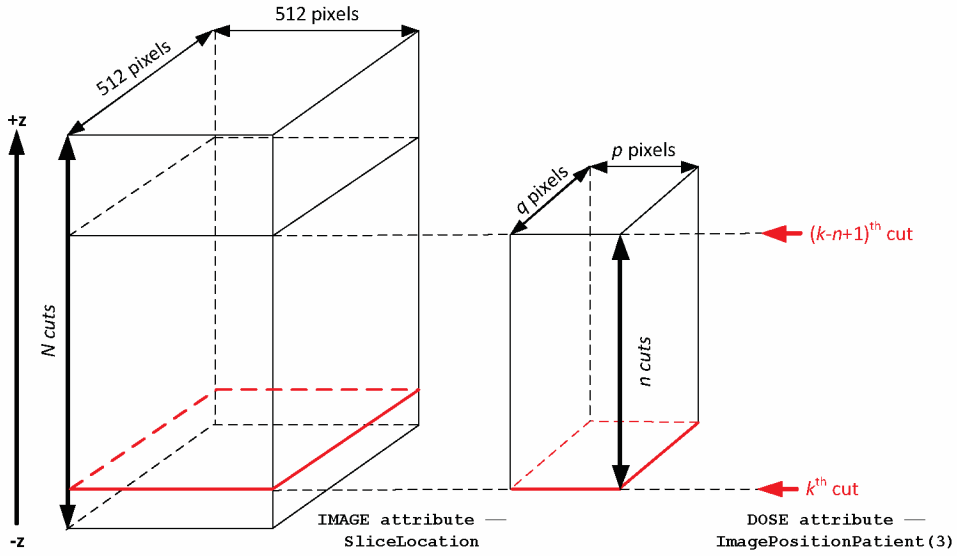

No dose for cuts < k -n +1 and cuts > k

Figure 4.9. Three dimensional RT Dose matrix mapping onto the CT data set. Step (a) A typical CT head data set contains N slices with a resolution of 512×512 pixels; Step (b) ImagePositionPatient attribute specifies the lowest z -slice in RT Dose matrix for superior-inferior alignment.

Since dose values were treated as a grid of discrete elements, interpolation was required to convert these sampled point values into continuous surface models. Figure 4.10 illustrates the effect of interpolation. As a recommended default option in the MATLAB program, triangle-based cubic interpolation method was adopted to generate the continuous dose distribution (Sandwell, 1987; Watson, 1992).

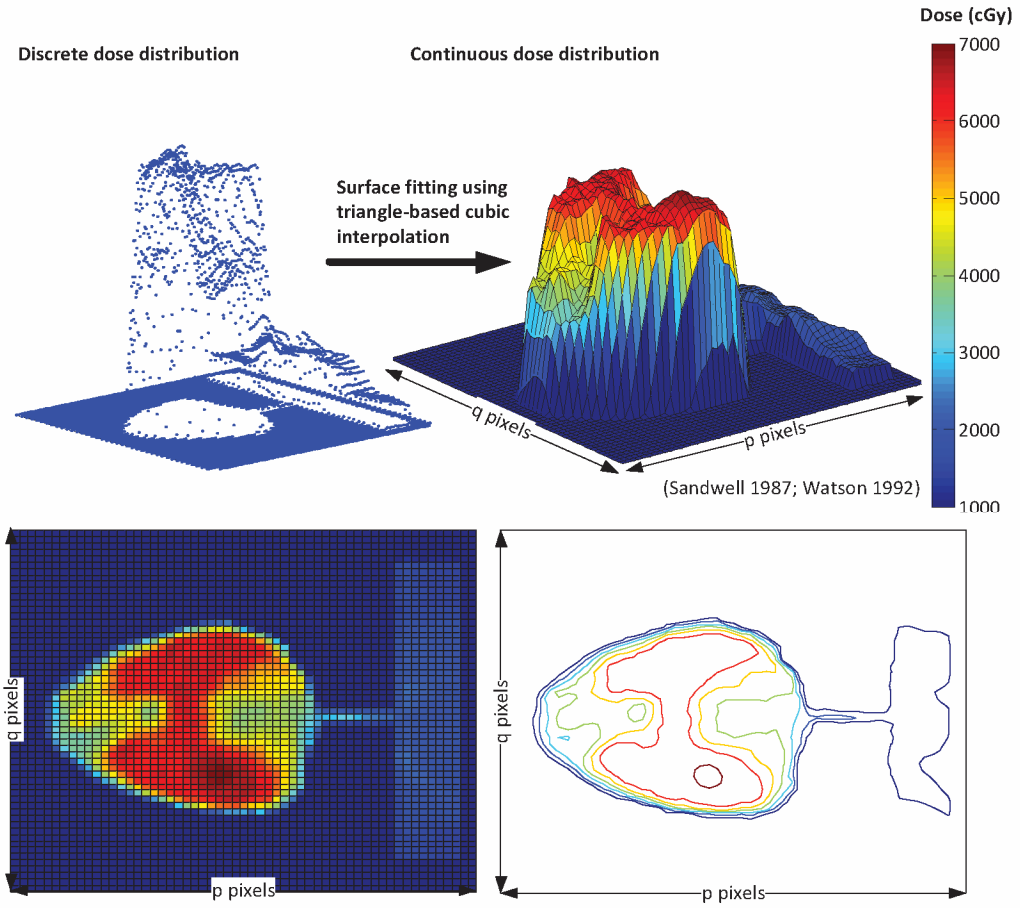

Figure 4.10. Generation of continuous dose distribution using triangle-based cubic interpolation.

According to the x- and y- coordinates of the `ImagePositionPatient` attribute of the CT image and RT Dose objects, two data sets were then registered in the same coordinate space (Figure 4.11). Proper coordinate transformation of RT Dose matrix including enlargement, rotation and translation was necessary.

As a result, the designated isodose curves representing hot and cold spots with the relevant target and structure contours superimposed on exact CT image slices could be displayed. The goal of IMRT was to deliver a dose distribution as homogeneous as possible within the PTV while sparing nearby OARs. Either overdose or underdose within targets should be penalized, whereas OARs only carried overdose penalties.

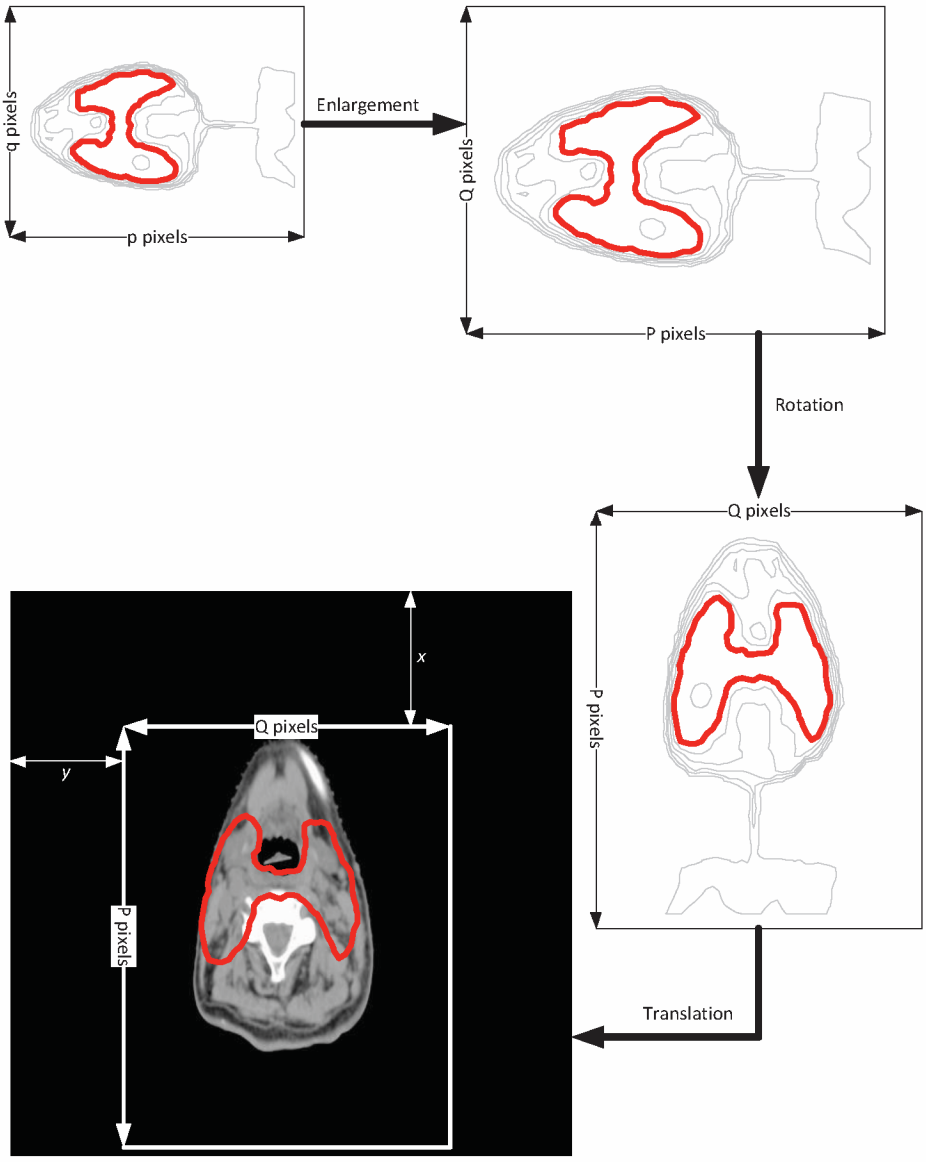

Figure 4.11. Coordinate transformation of RT Dose matrix.

4.1.3.4 Design of CAE system architecture

The CAE system architecture consisted of three fundamental components:

1. The algorithm for detection of violations,
2. The knowledge base providing information on overdose and underdose regions, and
3. Multiple GUI panels.

Evaluation of treatment plan was a knowledge-based decision-making process. By using the algorithm for detection of violations, knowledge was derived by extracting relevant data hidden in the DICOM RT objects and converting them into valuable information. Detailed knowledge of the anatomic location and extent of underdose and overdose regions could be built for plan evaluation. A good user-centered GUI and display design has a major impact on user acceptance and satisfaction. Based on the workflow of treatment planning in a radiation oncology department, multiple GUI panels were designed under the guidance of the experts to intelligently lead the planners through the steps of plan evaluation process. All panel layouts logically reflected user tasks sequences to enhance user-data interaction making operation intuitive. The four major GUI included:

1. The GUI for importing DICOM and DICOM RT objects, where the user could choose data file to import into the CAE system and perform anonymization.
2. The GUI input data panel which allowed users to formulate the plan acceptance criteria by inputting, viewing and modifying the dose and volume parameters for each target and OAR.
3. The GUI for treatment plan evaluation, giving simultaneous display of DVH curve, pertinent CT image, statistics for cold and hot spots and related dose

data parsed from DICOM RT objects to allow an immediate appreciation of potential problems.

4. The GUI for calculation of a two-dimensional conformity index with dose and distance incorporated (CI_{DD}) and other existing quantitative indices where the user could quantify the plan quality and control the display of regions of interest and prescription isodose lines.

4.1.4 Evaluation phase

From stand-alone units to fully integrated systems, the software should be evaluated against the requirements in order to provide feedbacks and ideas for future enhancements. Technical verification followed by performance evaluation were performed to validate the system.

Local ethics committee approval was sought and obtained for a waiver of informed consented for retrospective analysis of 30 consecutive IMRT head-and-neck plans delivered between January 2005 and January 2006 in the Department of Clinical Oncology from a collaborative hospital. Each patient was immobilized in supine position with a thermoplastic shell. Intravenous contrast-enhanced CT simulation was performed at 3mm intervals from the vertex to 5 cm below the sternoclavicular notch with 16-slice Brilliance Big Bore CT (Philips Medical Systems, Cleveland, OH). An IMRT plan was generated for each patient using Varian Eclipse treatment planning system (version 8.6) with anisotropic analytic algorithm (Varian Medical Systems, Palo Alto, CA). The plans generated aimed to cover at least 95% of the PTV with the planned

prescription dose and to keep the maximal point dose below 115% of the prescribed dose at each dose level. Different prescription doses for PTVs and dose constraints for OARs were applied according to individual planning guidelines. Using DICOM export in the Varian Eclipse treatment planning system, the DICOM-based data set for each IMRT plan including CT images, RT Dose and RT Structure Set objects were imported to the CAE system using the input data panel.

4.1.4.1 Technical verification

As part of the software development process, technical verification focused on internal correctness aiming at debugging the logic of a computer program (Lee et al., 2010; Koutkias et al., 2010). In order to examine its technical characteristics, static and dynamic testing methods were conducted to ensure that the codes were well-written. Without executing the codes, static methods involved manual inspection of the knowledge base and access to the internal data structure. Human experts were requested to check the knowledge base against the clinical acceptance guidelines to ensure that the non-structured knowledge source was exactly translated into the knowledge base. On the other hand, dynamic methods applied the CAE system to solve a set of test cases, focusing on validation issues such as external correctness.

4.1.4.2 Performance evaluation

As the reference standard, six planners (three physicists with six years of experience in IMRT planning and three resident physicists with half a year of

relevant experience) were firstly asked to evaluate the 30 IMRT plans randomly without the use of CAE system. As a conventional evaluation approach, manual DVH analysis was required. The DVH data for each region of interest was examined individually to find points or areas violating the plan acceptance criteria. Locations of hot and cold spots on each CT slice were identified and the corresponding z-values of the CT slices containing the violations were recorded by the planners. After that, plan evaluation was done randomly again by the same planner using the CAE system.

Normalized root-mean-square deviation (NRMSD) was considered a good measure of the difference between two sets of data (Pyakuryal et al., 2010). By definition, NRMSD is the square root of the mean squared error divided by the range of observed values (Tuikkala et al., 2008). This value is commonly expressed as a percentage, where lower values indicate smaller discrepancy between the original and observed values. NRMSD tests were performed for comparison of manually extracted data from treatment planning system and CAE extracted DVH data for each OAR.

Previous studies on the performance evaluation of decision support systems showed that speedy response time had a favorable impact on the user acceptance and satisfaction of a system (Degardin-Capon et al., 2008; Eitner et al., 2008). As a measure of efficiency, the total time needed to complete the plan evaluation with and without the use of CAE was recorded. Mixed-design ANOVA was conducted to explore the impact of use of CAE and level of experience on IMRT plan evaluation time. The statistical findings were regarded as significant if $p < 0.05$.

4.2 Enhancement of CAE system by development of a personalized target conformity index

The determination of an optimal treatment plan requires a clinical decision based on the balance between tumor control and normal tissue sparing. Besides satisfying dose constraints on normal tissues, adequate radiation dose coverage of PTV is crucial in increasing the probability of tumor control without complications. As a complementary tool to the CAE system, a two-dimensional conformity index with dose and distance incorporated (CI_{DD}) was designed to quantity the PTV coverage. Useful data stored in the DICOM RT objects were extracted to provide enough information to compute the CI_{DD}. The voxel size used in CI_{DD} was $2.5\times2.5\times3 mm^3$. The proposed algorithm for calculation of CI_{DD} was based on two central assumptions. Firstly, adequate GTV coverage is mandatory to reduce the likelihood of local recurrence and improve survival rate. Secondly, cold spots are generally more acceptable if they are more distant from GTV. The CI_{DD} scoring system contains four major components, namely GTV coverage factor, GTV underdose factor, (PTV minus GTV) coverage factor and (PTV minus GTV) underdose and distance factor.

Using IMRT with simultaneous modulated accelerated radiation therapy (SMART) boost, the GTV is given a higher total radiation dose within the same treatment period than the surrounding subclinical regions enabling differential dose delivery to different parts of the targets. In our standard treatment guidelines for nasopharyngeal carcinoma, subscripts with the GTV nomenclature are applied to distinguish between the primary nasopharyngeal tumor (np as in GTV_{np}) and nodal gross tumor volume (n as in GTV_n). Note that for a typical

head-and-neck case, the prescribed dose to the GTV at the primary and nodal sites plus 3mm margin is 70Gy, while the PTVs for microscopic disease representing high and low risk disease regions receive 66Gy and 60Gy, respectively.

Like the development of CAE system, the hierarchical bottom-up searching approach was implemented to efficiently search for the presence of PTV underdose regions. As mentioned in Section 4.1.1.1, all cold spots inside PTV were found by searching the non-overlapping boundaries between the PTV contours and the corresponding prescribed isodose lines on every CT slice.

The same underdose region extraction model as described in Section 4.1.3.3 was employed. Valuable information hidden in the DICOM RT objects was harvested for computation of each CI_{DD} component. PTV coverage at each prescribed dose level was evaluated individually. To construct the grid dose, each pixel value stored in the Image pixel module was multiplied by the `DoseGridScaling` attribute in the RT Dose object. Besides, the contours of GTV and PTVs defined within the `ROIContourSequence` attribute in the RT Structure Set object were reconstructed and mapped onto the CT data set according to the coordinates of the `ImagePositionPatient` attribute in RT Dose object.

4.2.1 GTV coverage factor

GTV is the most predictive independent survival variable in the multivariate analysis (Chao et al., 2004; Tyng et al., 2009). The concept of selective dose escalation to GTV has recently been advocated as a means of improving local

tumor control (Montejo et al., 2011; Ozyigit et al., 2011). The GTV coverage factor, G, is the probability measures of the underdose region inside GTV which serves as a starting point for treatment plan comparison.

Theorem 4.1 (GTV coverage factor): For each underdose region inside GTV, i.e., GTV receiving less than 70Gy, the GTV coverage factor G is defined as

$$G = \frac{\sum_{\text{all } I_z} 70\text{Gy} \cap (\text{GTV}_n \cup \text{GTV}_{np})}{\sum_{\text{all } I_z} (\text{GTV}_n \cup \text{GTV}_{np})}, \tag{4.1}$$

where I_z is the image of z^{th} cut, $\Sigma_{\text{all } I_z}$ is the volumetric sum of all cuts, $\cap$ is the intersection of two regions, and $\cup$ is the union of two regions.

Abbreviations: GTV_n= Nodal gross tumor volume; GTV_{np} = Nasopharyngeal gross tumor volume.

Properties of Theorem 4.1:

1. $70\text{Gy} \cap (\text{GTV}_n \cup \text{GTV}_{np})$ is a subset of $(\text{GTV}_n \cup \text{GTV}_{np})$. We write $70\text{Gy} \cap (\text{GTV}_n \cup \text{GTV}_{np}) \subseteq (\text{GTV}_n \cup \text{GTV}_{np})$;
2. $0 \le G \le 1$;
3. If $G = 1$, we have $70\text{Gy} \supseteq (\text{GTV}_n \cup \text{GTV}_{np})$; Conversely, if $G = 0$, we have $70\text{Gy} \cap (\text{GTV}_n \cup \text{GTV}_{np}) = \varnothing$.

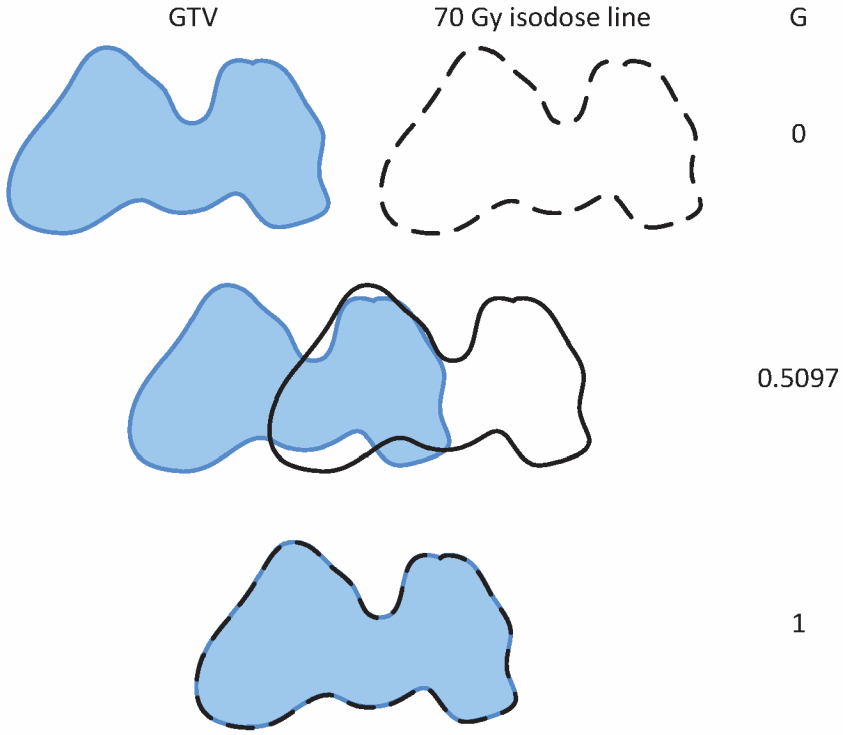

Figure 4.12. Examples showing different GTV coverage factors.

As illustrated in Figure 4.12, G equals to 1 if whole GTV is covered by a prescribed dose of 70Gy and G approaches zero with continuously decreasing volumes of GTV receiving dose of at least 70Gy. Figure 4.13(a) illustrates the 70Gy isodose line, GTV_{np} and PTV_{np70} contours superimposed on an axial CT images. Close examination of Figure 4.13(b) shows that the GTV_{np} is not fully encompassed by the 70Gy isodose line.

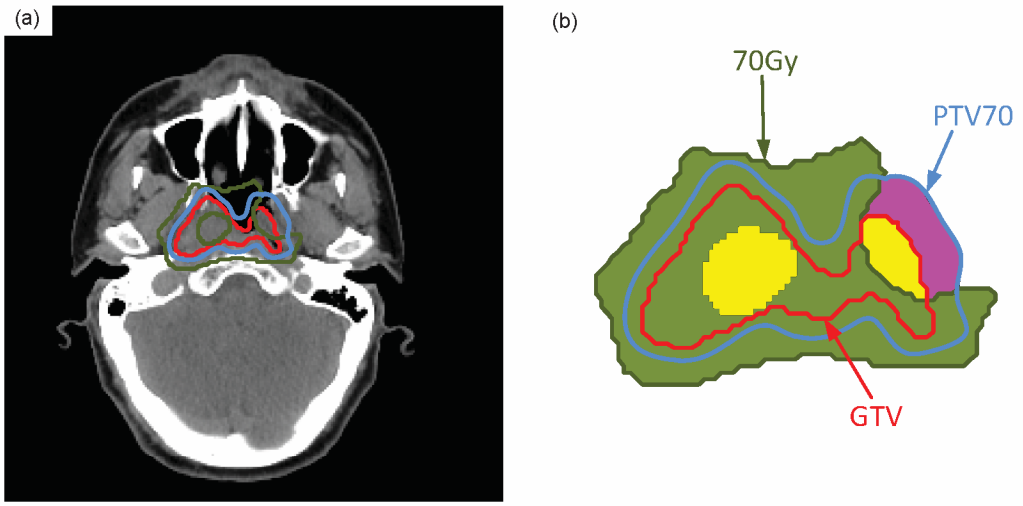

Figure 4.13. The target contours and isodose line superimposed on the CT image (a) The GTV_{np} contour (red), PTV_{np70} contour (light blue) and 70Gy isodose line (dark green) superimposed on an axial CT image; (b) A close-up illustrating the spatial relationship among GTV_{np}, PTV_{np70} and 70Gy isodose line. The yellow region indicates the grade 1 geographic miss and pink region indicates the grade 2 geographic miss.

Using similar concepts described by Leong et al. (2006) and Zheng et al. (2006), the geographic miss of tumor was classified as grade 1 or grade 2 according to the locations of cold spots within PTV (Leong et al., 2006; Zheng et al., 2006). A grade 1 geographic miss was defined as inadequate GTV coverage while a grade 2 geographic miss was defined as inadequate coverage of PTV excluding GTV. It

is widely accepted that GTV coverage should take precedence over PTV coverage. Hence, every effort should be made to avoid grade 1 geographic miss as the GTV always contains the greatest tumor burden (Tyng et al., 2009).

The first step in calculating *G* is to extract the overlapping region between GTV and 70Gy isodose line on every single CT slice. As an example in Figure 4.14, the purple- and red- shaded areas denote the numerator and denominator of the GTV coverage factor, respectively.

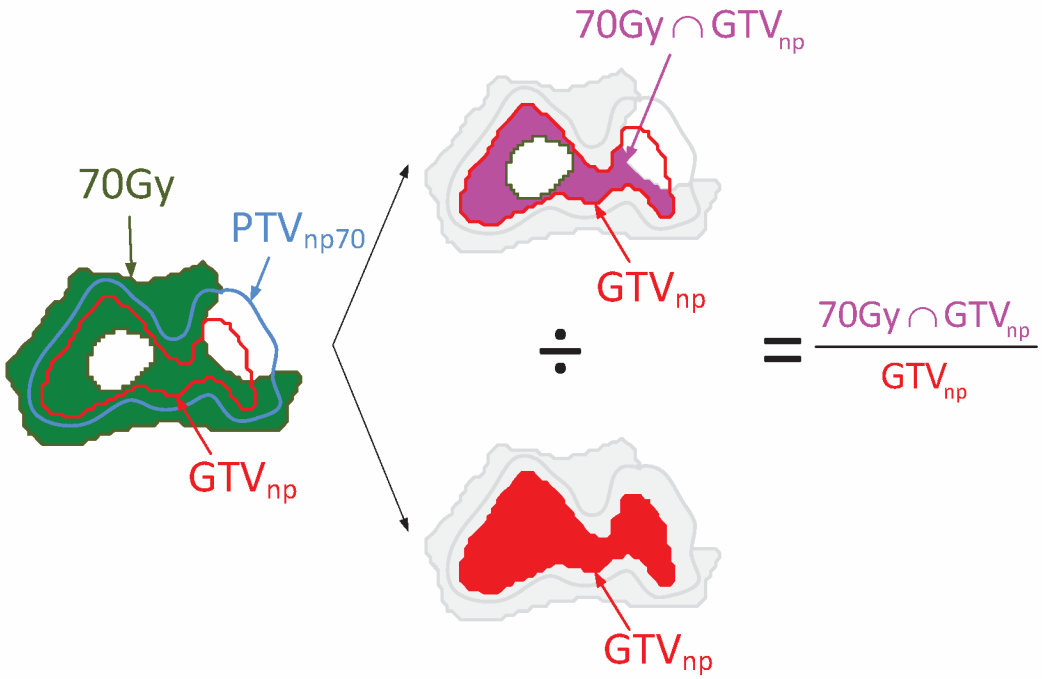

Figure 4.14. Diagrammatic calculation of GTV coverage factor.

Abbreviations: GTV_{np} = Nasopharyngeal gross tumor volume; PTV_{np70} = 70 Gy to nasopharyngeal planning target volume.

4.2.2 GTV underdose factor

Tomé et al. (2002) and Zhao et al. (2010) demonstrated that there was a precipitous tumor control probability drop with the presence of deep cold spots in the GTV which always had higher malignant cell density than peripheral PTV

region. Compared to the volume of tumor underdosed, the magnitude of the underdosage is a more important determinant of tumor control probability (Withers, 2000). Knowing this, the GTV underdose factor was designed giving penalty based on the extent of underdosage for each GTV pixel.

Theorem 4.2 (GTV underdose factor): For each underdose pixel inside GTV, the GTV underdose factor P is defined as

$$P(dose) = 1 - \sum_{\text{all } I_z} p(dose) = 1 - \sum_{\text{all } I_z} \exp\left(-\frac{2 \times dose^2}{35^2}\right), \quad 0 \le dose \le 70, \qquad (4.2)$$

where $\exp(x) = \sum_{n=0}^{\infty} \frac{x^n}{n!}$, $\exp(0) = 1$ and $\exp(1) \approx 2.71828$.

Properties of Theorem 4.2:

1. $\exp(x)$ is an increasing function, while $\exp(-x)$ is a decreasing function;
2. $P(0) = 0$ (maximum penalty), $\lim_{dose \to 70^+} P(dose) = 1$ (no underdose).

Proof of Theorem 4.2:
We begin with the probability density function or Gaussian function, which takes the form

$$f(x) = \frac{1}{\sqrt{2\pi}\sigma} \exp\left(-\frac{(x-\mu)^2}{2\sigma^2}\right), \quad -\infty < x < \infty, \qquad (4.3)$$

where μ is the mean and σ is the standard deviation. The amplitude of $f(x)$ occurs when $x = \mu$, i.e., $f(x = \mu) = \frac{1}{\sqrt{2\pi}\sigma}$ (as depicted in Figure 4.15).

Noting that

$$\begin{aligned}
\lim_{x \to \mu \pm 4\sigma} f(x) &= \lim_{x \to \mu \pm 4\sigma} \frac{1}{\sqrt{2\pi}\sigma} \exp\left(-\frac{(x-\mu)^2}{2\sigma^2}\right) \\
&= \frac{1}{\sqrt{2\pi}\sigma} \exp\left(-\frac{(\mu \pm 4\sigma - \mu)^2}{2\sigma^2}\right) \\
&= \frac{1}{\sqrt{2\pi}\sigma} \exp\left(-\frac{16\sigma^2}{2\sigma^2}\right) \\
&= \frac{1}{\sqrt{2\pi}\sigma} \exp(-8), \ \exp(-8) \approx 3.35 \times 10^{-4}, \\
&\approx 0.
\end{aligned} \qquad (4.4)$$

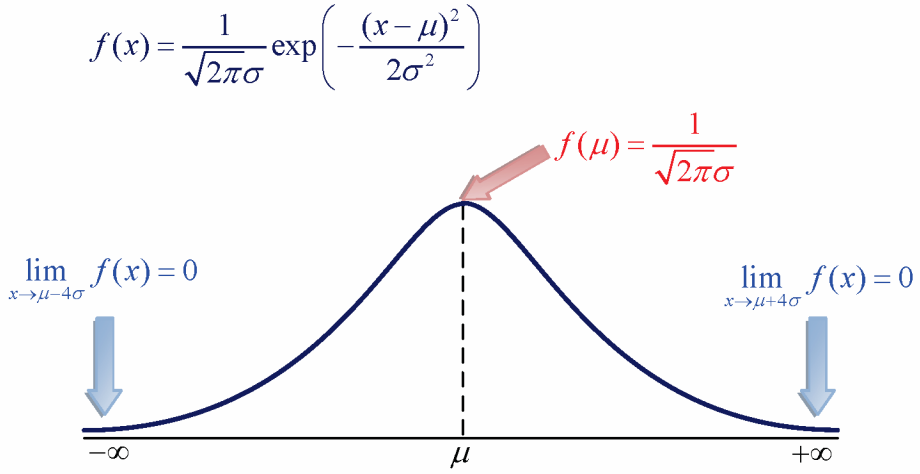

Figure 4.15. Gaussian function.

Similar to previous study by Miften et al. (2004), Gaussian function was applied to penalize the cold spots (Miften et al., 2004). This bell-shaped function was chosen because of its exponentially decreasing character. With a central peak, its tails drop towards zero rapidly as x approaches infinity (Figure 4.15). The use of GTV underdose factor, $P(dose)$, to quantify the dose-volume violations should satisfy the following criterions (as demonstrated in Figure 4.16):

1. The admissible values of penalty function are non-negative values;
2. No penalty is given when the GTV pixel receiving not less than 70 Gy;
3. Maximum penalty is enforced whenever the GTV pixel receives 0 Gy.

Therefore, penalty function $p(dose)$ is given by first normalizing the function $f(x)$ (by dividing its amplitude $\frac{1}{\sqrt{2\pi}\sigma}$), choosing $\mu=0$, $4\sigma=70$, i.e., $\sigma=\frac{70}{4}$ and $x=\text{dose}$. We then have

$$p(dose) = \frac{f(dose)}{\frac{1}{\sqrt{2\pi}\sigma}} = \exp\left(-\frac{(dose-0)^2}{2\left(\frac{70}{4}\right)^2}\right) = \exp\left(-\frac{2\times dose^2}{35^2}\right). \tag{4.5}$$

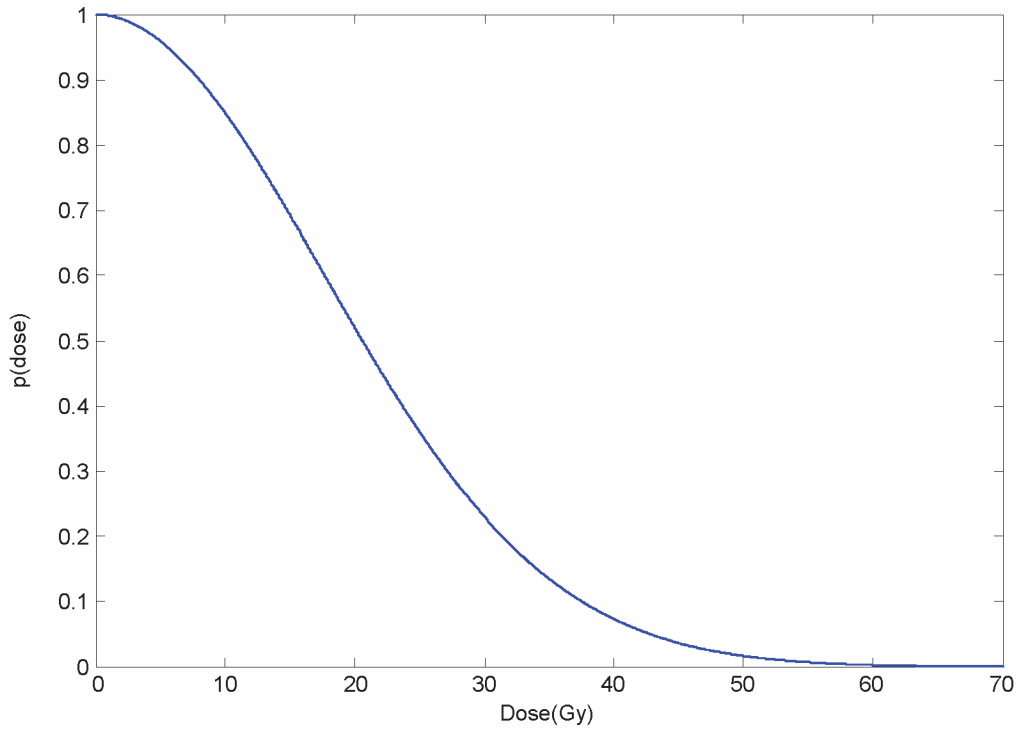

Figure 4.16. The penalty function p.

As a result, the GTV underdose factor P is defined as

$$P(dose) = 1 - \sum_{\text{all } I_z} p(dose). \tag{4.6}$$

4.2.3 (PTV minus GTV) coverage factor

For grade 2 geographic miss, the (PTV minus GTV) coverage factor was introduced as the total probability measures of the underdose region. To meet the needs for comprehensive evaluation of IMRT plan with SMART boost, PTV

coverage at each prescribed dose level was considered individually.

Theorem 4.3 ((PTV minus GTV) coverage factor): For each underdose region inside PTV excluding GTV, the (PTV minus GTV) coverage factor PG is defined as

$$PG = \frac{1}{6}\left\{ \frac{\sum_{\text{all } I_z} 70\text{Gy} \cap (\text{PTV}_{n70} - \text{GTV}_n)}{\sum_{\text{all } I_z} (\text{PTV}_{n70} - \text{GTV}_n)} + \frac{\sum_{\text{all } I_z} 70\text{Gy} \cap (\text{PTV}_{np70} - \text{GTV}_{np})}{\sum_{\text{all } I_z} (\text{PTV}_{np(70)} - \text{GTV}_{np})} + \right.$$
$$\frac{\sum_{\text{all } I_z} 66\text{Gy} \cap (\text{PTV}_{n66} - \text{PTV}_{n70})}{\sum_{\text{all } I_z} (\text{PTV}_{n66} - \text{PTV}_{n70})} + \frac{\sum_{\text{all } I_z} 66\text{Gy} \cap (\text{PTV}_{np66} - \text{PTV}_{np70})}{\sum_{\text{all } I_z} (\text{PTV}_{np66} - \text{PTV}_{np70})} +$$
$$\left. \frac{\sum_{\text{all } I_z} 60\text{Gy} \cap (\text{PTV}_{n60} - \text{PTV}_{n66})}{\sum_{\text{all } I_z} (\text{PTV}_{n60} - \text{PTV}_{n66})} + \frac{\sum_{\text{all } I_z} 60\text{Gy} \cap (\text{PTV}_{np60} - \text{PTV}_{np66})}{\sum_{\text{all } I_z} (\text{PTV}_{np60} - \text{PTV}_{np66})} \right\}, \quad (4.7)$$

where $\text{GTV}_n \supset \text{PTV}_{n70} \supseteq \text{PTV}_{n66} \supseteq \text{PTV}_{n60}$ and $\text{GTV}_{np} \supset \text{PTV}_{np70} \supseteq \text{PTV}_{np66} \supseteq \text{PTV}_{np60}$.

Properties of Theorem 4.3:

1. $70\text{Gy} \cap (\text{PTV}_{n70} - \text{GTV}_n) \subseteq (\text{PTV}_{n70} - \text{GTV}_n)$,
   $70\text{Gy} \cap (\text{PTV}_{np70} - \text{GTV}_{np}) \subseteq (\text{PTV}_{np70} - \text{GTV}_{np})$,
   $66\text{Gy} \cap (\text{PTV}_{n66} - \text{PTV}_{n70}) \subseteq (\text{PTV}_{n66} - \text{PTV}_{n70})$,
   $66\text{Gy} \cap (\text{PTV}_{np66} - \text{PTV}_{np70}) \subseteq (\text{PTV}_{np66} - \text{PTV}_{np70})$,
   $60\text{Gy} \cap (\text{PTV}_{n60} - \text{PTV}_{n66}) \subseteq (\text{PTV}_{n60} - \text{PTV}_{n66})$,
   $60\text{Gy} \cap (\text{PTV}_{np60} - \text{PTV}_{np66}) \subseteq (\text{PTV}_{np60} - \text{PTV}_{np66})$;
2. $0 \le PG \le 1$;
3. If $PG = 1$, we have
   $70\text{Gy} \supseteq (\text{PTV}_{n70} - \text{GTV}_n)$, $70\text{Gy} \supseteq (\text{PTV}_{np70} - \text{GTV}_{np})$,
   $66\text{Gy} \supseteq (\text{PTV}_{n66} - \text{PTV}_{n70})$, $66\text{Gy} \supseteq (\text{PTV}_{np66} - \text{PTV}_{np70})$,
   $60\text{Gy} \supseteq (\text{PTV}_{n60} - \text{PTV}_{n66})$, $60\text{Gy} \supseteq (\text{PTV}_{np60} - \text{PTV}_{np66})$;
   Conversely, if $PG = 0$, we have
   $70\text{Gy} \cap (\text{PTV}_{n70} - \text{GTV}_n) = \varnothing$, $70\text{Gy} \cap (\text{PTV}_{np70} - \text{GTV}_{np}) = \varnothing$,
   $66\text{Gy} \cap (\text{PTV}_{n66} - \text{PTV}_{n70}) = \varnothing$, $66\text{Gy} \cap (\text{PTV}_{np66} - \text{PTV}_{np70}) = \varnothing$,
   $60\text{Gy} \cap (\text{PTV}_{n60} - \text{PTV}_{n66}) = \varnothing$, $60\text{Gy} \cap (\text{PTV}_{np60} - \text{PTV}_{np66}) = \varnothing$.

Abbreviation: (PTV – GTV) = (PTV minus GTV).

Figure 4.17 demonstrates the target contours required to calculate the (PTV minus GTV) coverage factor. Three prescription doses are delivered to various

PTVs, designated as PTV_{n60}, PTV_{n66}, PTV_{n70}, PTV_{np60}, PTV_{np66} and PTV_{np70} with the subscripts representing different dose levels prescribed to either primary nasopharyngeal tumor or nodal region. Using the inside-out approach, the non-overlapping regions (NORs) between (1) GTV_{np} and PTV_{np70}; (2) GTV_n and PTV_{n70}; (3) PTV_{np70} and PTV_{np66}; (4) PTV_{n70} and PTV_{n66}; (5) PTV_{np66} and PTV_{np60}; (6) PTV_{n66} and PTV_{n60} were drawn out. The next step in calculating PG was to find out the overlapping regions between NORs and their corresponding prescribed dose levels on every single CT slice. For simplicity, Figure 4.18 demonstrates how to compute the first term of PG. The dark green- and light blue- shaded areas represent the numerator and denominator, respectively.

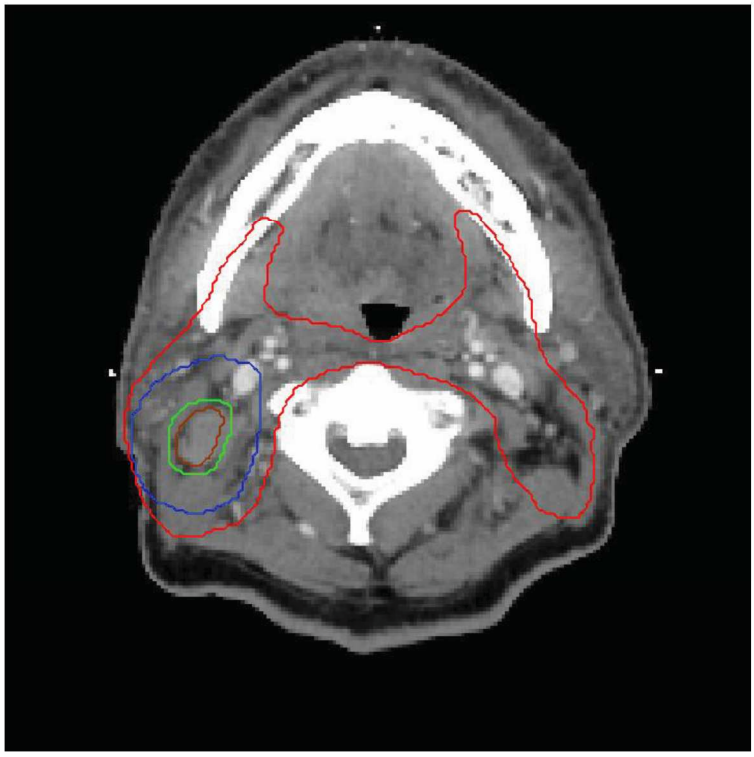

Figure 4.17. Diagram showing various target contours required for calculation of the (PTV minus GTV) coverage factor. The GTV_n, PTV_{n70}, PTV_{n66}, PTV_{n60} are indicated by brown, green, blue and red lines, respectively.

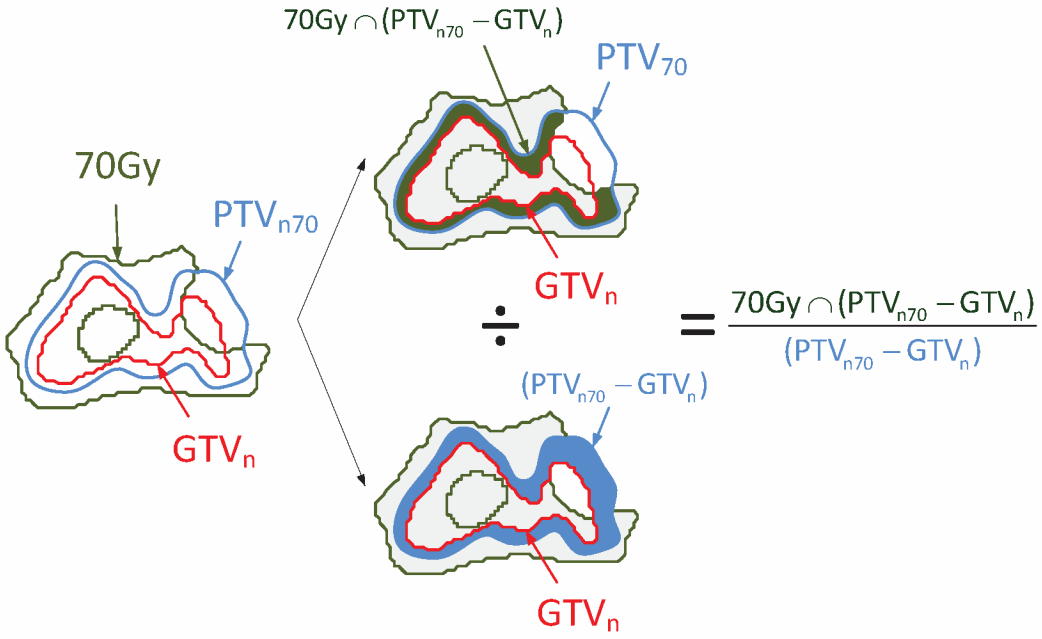

Figure 4.18. Diagrammatic calculation of first term of (PTV minus GTV) coverage factor.

4.2.4 (PTV minus GTV) underdose and distance factor

The (PTV minus GTV) underdose and distance factor was proposed based on the hypothesis that there was differing importance of cold spots to the tumor control for grade 2 geographic miss depending on their locations. Apart from the dose penalty factor, a distance based exponential function was employed taking the specific tumor geometry into account. In the following theorem, two versions of (PTV minus GTV) underdose and distance factor are presented, in the presence of GTV (Theorem 4.4), and in the absence of GTV (Theorem 4.5).

Theorem 4.4 ((PTV minus GTV) underdose and distance factor): For each underdose pixel inside (PTV minus GTV) in the presence of GTV, the (PTV minus GTV) underdose and distance factor P is defined as

$$P(dose, distance) = 1 - \sum_{\text{all } I_z} p(dose, distance)$$
$$= 1 - \sum_{\text{all } I_z} \exp\left(-\left(\frac{8 \times dose^2}{d^2} + \frac{8 \times distance^2}{m^2} \right) \right), \tag{4.8}$$

where $0 \le dose \le d$, $d = 60, 66, 70$, $0 \le distance \le m$ and $m =$ $\max\{\partial \text{PTV} - \partial \text{GTV}\}$ = furthest distance between the boundary of PTV and GTV for each I_z.

Theorem 4.5 ((PTV minus GTV) underdose and distance factor): For each underdose pixel inside (PTV minus GTV) in the absence of GTV, the (PTV minus GTV) underdose and factor P is defined as

$$P(dose, distance) = 1 - \sum_{\text{all } I_z} p(dose, distance)$$
$$= 1 - \sum_{\text{all } I_z} \exp\left(-\left(\frac{8 \times dose^2}{d^2} + \frac{8 \times distance^2}{m^2} \right) \right), \tag{4.9}$$

where $0 \le dose \le d$, $d = 60, 66, 70$, $0 \le distance \le m$ and $m =$ $\max\{\partial \text{PTV} - \text{PTV}_c\}$ = furthest distance between the boundary of PTV and the centroid of PTV, i.e., PTV_c for each I_z.

The following example demonstrates how to find the distance m in the presence of GTV. Figure 4.19(a) is a schematic diagram illustrating relations between GTV and PTV with their boundaries shown in yellow and blue, respectively. Given a DICOM RT image, pixel data are stored starting at the top left. The coordinate values increase down and to the right. In this example, the coordinate (0,0) is the upper-left pixel and coordinate (9,9) is in the lower-right. PTV is completely inclusive of the GTV and the (PTV minus GTV) region is defined by subtracting the GTV from the PTV as shown in white.

With the goal of deriving a customized penalty factor, the distances between individual pixel and its nearest PTV boundary should be found. The Pythagoras' theorem is of fundamental importance in Euclidean geometry providing the basis for the distance formula. As shown in Figure 4.19(b), the Euclidean distance between two points (5,5) and (9,9) is given by

$$\sqrt{(9-5)^2+(9-5)^2} = 4\sqrt{2}.$$

In a similar manner, the shortest distances from any given pixel to the boundary of GTV were computed (Figure 4.19(b)). The furthest distance among them, denoted as m , becomes the denominator. In this example, m is determined to be $4\sqrt{2}$.

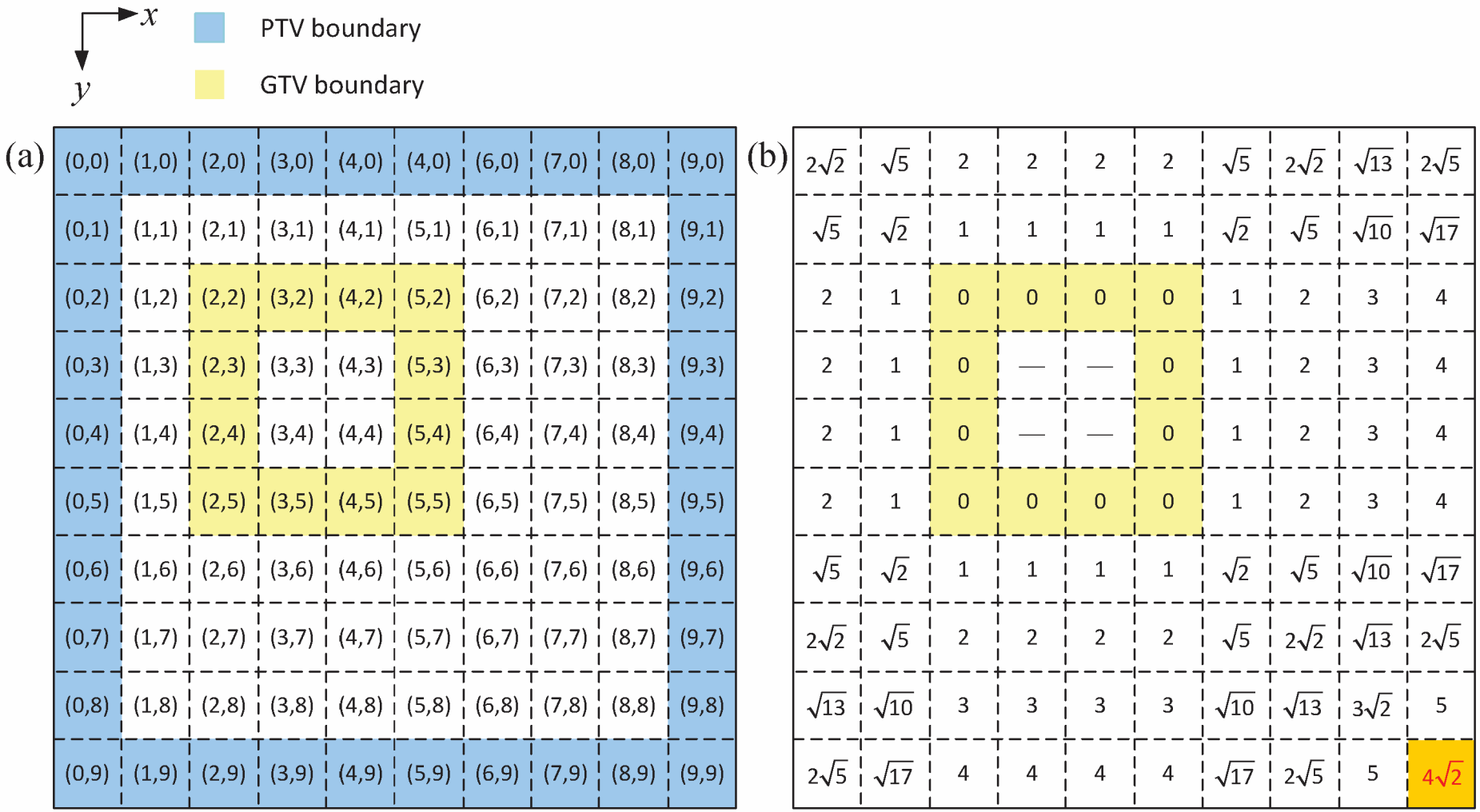

Figure 4.19. Schematic illustrations of the relations between GTV and PTV. (a) The coordinate system used in this example has the origin in the upper left with the *x*-axis extending to the right and the *y*-axis extending downwards; (b) The distance from one pixel to its nearest GTV boundary.

Properties of Theorem 4.4 and Theorem 4.5:

1. Zero dose, at the boundary of GTV or centroid of PTV
$$\lim_{(dose,distance)\to(0,0)} P(dose,distance)=0;$$

2. Prescribed dose, at the furthest distance on the boundary of GTV
$$\lim_{(dose,distance)\to(d,m)} P(dose,distance)=1;$$

3. Zero dose, $0\le distance\le m$, $P(dose,distance)$ depends only on distance
$$\lim_{dose\to 0} P(dose,distance)=1-\sum_{\text{all } I_z}\exp\left(-\frac{8\times distance^2}{m^2}\right);$$

4. Zero distance on the boundary of GTV or centroid of PTV, $0\le dose\le d$ at the boundary of GTV or centroid of PTV, $P(dose,distance)$ depends only on dose
$$\lim_{distance\to 0} P(dose,distance)=1-\sum_{\text{all } I_z}\exp\left(-\frac{8\times dose^2}{d^2}\right).$$

The (PTV minus GTV) underdose and distance factor should satisfy the following conditions. In an extreme scenario where zero dose is delivered to a pixel situated at the boundary of GTV or centroid of PTV, the $P(dose,distance)$ is set to zero imposing the maximum penalty. On the other hand, the $P(dose,distance)$ equals to 1 whichever pixel farthest away from the GTV border receiving not less than its prescribed dose. When pixel within PTV excluding GTV gets zero dose, only the distance factor is considered. In contrast, $P(dose,distance)$ depends only on dose for all pixels located at the boundary of GTV or centroid of PTV.

Proof of Theorem 4.4 and Theorem 4.5:

Similar to the proof of Theorem 4.2, we start with a more general 2 dimensional elliptical Gaussian function, which takes the form

$$f(x,y)=A\exp\left(-\left(\frac{(x-x_0)^2}{2\sigma_x^2}+\frac{(y-y_0)^2}{2\sigma_y^2}\right)\right),\quad -\infty<x,y<\infty, \tag{4.10}$$

where $A=\text{amplitude}$, x_0, y_0, σ_x and σ_y are real constants. $(x_0,y_0)=$ center of the Gaussian function and σ_x, σ_y controls the x, y spread from

the center. The amplitude of $f(x,y)$ occurs when $x = x_0$, $y = y_0$ i.e., $f(x = x_0, y = y_0) = A$ (as depicted in Figure 4.20).

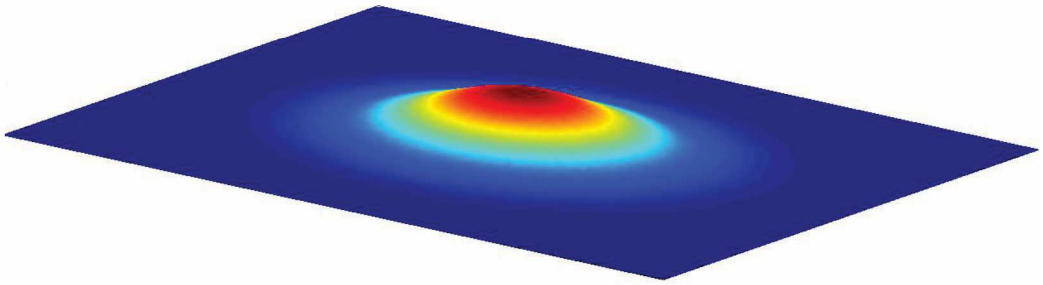

Figure 4.20. Two-dimensional elliptical Gaussian function.

Noting that

$$\begin{aligned}\lim_{\substack{x\to x_0\pm 4\sigma_x,\\ y\to y_0\pm 4\sigma_y}} f(x,y) &= \lim_{\substack{x\to x_0\pm 4\sigma_x,\\ y\to y_0\pm 4\sigma_y}} A\exp\left(-\left(\frac{(x-x_0)^2}{2\sigma_x^2}+\frac{(y-y_0)^2}{2\sigma_y^2}\right)\right)\\ &= \lim_{\substack{x\to x_0\pm 4\sigma_x,\\ y\to y_0\pm 4\sigma_y}} A\exp\left(-\left(\frac{16\sigma_x^2}{2\sigma_x^2}+\frac{16\sigma_y^2}{2\sigma_y^2}\right)\right)\\ &= A\exp(-16)\\ &\approx 0.\end{aligned} \tag{4.11}$$

By integrating both spatial and dosimetric importance for each pixel, (PTV minus GTV) underdose and distance factor was fitted with a two-dimensional elliptical Gaussian function. As illustrated in Figure 4.20, the value becomes maximal at the origin of a Cartesian coordinate system and falls off precipitously to zero as x - and y - values approaches infinity. In two dimensions, $P(dose, distance)$ depends on two individual factors, namely distance and dose penalties (Figure 4.21). Using the two-dimensional elliptical Gaussian function, the impact of distance and dose penalties are substantially larger for deep cold spots situated close to the GTV border or the PTV centroid but peter out quickly wherever slight underdosage occurred at the PTV boundary. Like the $P(dose)$, the admissible values of penalty function are non-negative values. No penalty is

enforced whenever pixel receives not less than its prescribed dose regardless of its location.

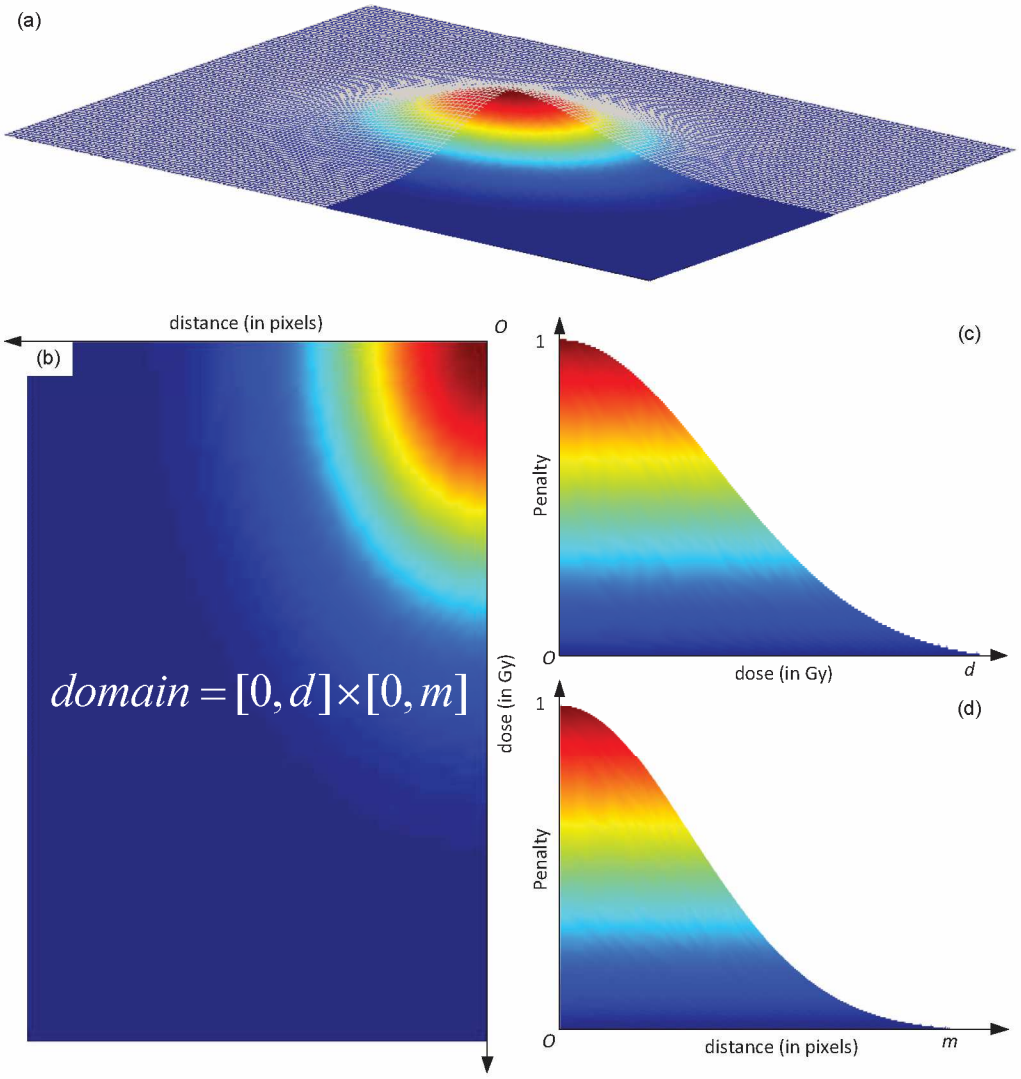

Figure 4.21. (a) Two-dimensional (PTV minus GTV) underdose and distance factor; (b) Domain of the (PTV minus GTV) underdose and distance factor; (c) Penalty with dose; (d) Penalty with distance.

Therefore, the penalty function p is given by first normalizing the function $f(x,y)$ (by dividing its amplitude A), choosing $x_0 = y_0 = 0$, $x_0 + 4\sigma_x = d$, i.e., $\sigma_x = \frac{d}{4}$ and letting $x = dose$, $y_0 + 4\sigma_y = m$, i.e., $\sigma_y = \frac{m}{4}$ and letting $y = distance$. We then have

$$
\begin{aligned}
p(dose, distance) &= \frac{f(dose, distance)}{A} \\
&= \exp\left(-\left(\frac{dose^2}{2(d/4)^2} + \frac{distance^2}{2(m/4)^2}\right)\right), \\
&= \exp\left(-\left(\frac{8 \times dose^2}{d^2} + \frac{8 \times distance^2}{m^2}\right)\right),
\end{aligned}
\tag{4.12}
$$

where $0 \le dose \le d,\ 0 \le distance \le m.$

As a result, (PTV minus GTV) underdose and distance factor P is defined as

$$
P(dose, distance) = 1 - \sum_{\text{all } I_z} p(dose, distance) . \tag{4.13}
$$

4.2.5 CI_{DD} calculation

To consolidate all four distinct factors into one CI_{DD} score, Euclidean 2-norm was applied to represent the quality of a treatment plan. This is similar to the method described by Leung et al. (2007). For a hypothetical case when 100% of prescribed dose is homogenously delivered to the multiple PTVs, all four factors should be unity. The CI_{DD} score is defined as the Euclidean 2-norm between these four factors and $(1,1,1,1)$ to describe the overall plan quality. The Euclidean 2-norm is defined as

$$
\begin{aligned}
CI_{DD} &= \| (1,1,1,1) - (G, P(dose), PG, P(dose, distance)) \|_2 \\
&= \sqrt{(1-G)^2 + (1-P(dose))^2 + (1-PG)^2 + (1-P(dose, distance))^2} .
\end{aligned}
\tag{4.14}
$$

The worst scenario is $\sqrt{4} = 2$ when $G = P(dose) = PG = P(dose, distance) = 0$. In clinical situation, it occurs when all GTV and (PTV minus GTV) pixels receive 0Gy. In contrast, CI_{DD} score is zero for a perfect case, i.e., $G = P(dose) = PG = P(dose, distance) = 1$. This scenario occurs whenever all GTV and (PTV minus GTV) pixels receive not less than the prescribed dose.

Unlike other indices, a lower CI_{DD} score indicates better target coverage in this study.

4.2.6 Evaluation of CI_{DD} scoring system

In order to evaluate the CI_{DD} scoring system, three CT image data sets with stage III or IV nasopharyngeal carcinoma (NPC) cases were collected. Ten IMRT plans were generated from each data set using the Eclipse treatment planning system (version 8.6) (Varian Medical Systems, Palo Alto, CA). Table 4.5 shows the typical optimization parameters for an IMRT NPC plan in clinical practice. For each plan, inverse IMRT plans were optimized using the same sets of constraints as shown in Table 4.5 except for the changing priority factors of PTVs. For plan 1 of each data set, target coverage was assigned the highest priority value of 350 for upper and lower limits. With step-wise relaxation, the priority factors for PTVs were decreased by 20 for each successive IMRT plan. As a result, the plan qualities were expected to deteriorate sequentially in terms of target dose conformity from plan 1 to plan 10 for each data set.

Table 4.5. Optimization parameters for a typical IMRT NPC plan.

Regions of Interest (ROIs)	Limits	Dose (Gy)	Volume (%)	Priority
Brainstem	Upper	54	0	300
Brainstem + 3mm shell	Upper	60	1	300
Spinal Cord	Upper	45	0	300
Spinal Cord + 3mm shell	Upper	50	0	300
Temporal lobes	Upper	70	0	250
Optic chiasm	Upper	54	0	250
Optical nerves	Upper	54	0	250
Parotid gland	Upper	26	50	200
PTV_{np70} and PTV_{n70}	Upper	75	0	350
PTV_{np70} and PTV_{n70}	Lower	74	100	350
PTV_{np66} and PTV_{n66}	Upper	72	0	350
PTV_{np66} and PTV_{n66}	Lower	70	100	350
PTV_{np60} and PTV_{n60}	Upper	64	0	350
PTV_{np60} and PTV_{n60}	Lower	63	100	350

Abbreviations: PTV_{np} = nasopharyngeal planning target volume; PTV_{n} = nodal planning target volume; PTV_{np70} = 70 Gy to PTV_{np}; PTV_{n70} = 70 Gy to PTV_{n}; PTV_{np66} = 66 Gy to PTV_{np}; PTV_{n66} = 66 Gy to PTV_{n}; PTV_{np60} = 60 Gy to PTV_{np}; PTV_{n60} = 60 Gy to PTV_{n}.

Apart from the CI_{DD} score, the RTOG conformity index (CI_{RTOG}), healthy tissues conformity index (HTCI), conformation number (CN), target coverage factor were computed using the CAE system. Their standard equations were inputted into the CAE system for calculation. The plan quality discerning power of CI_{DD} was assessed by ranking the 10 IMRT plans of each CT data set based on the CI_{DD} scores and by comparing the results with other indices. The coefficient of variation, also known as "relative variability", represents the ratio of the standard

deviation to the mean. As a dispersion measurement, coefficient of variation is a useful statistic for comparing diversity across data sets (Kelley, 2007). A greater dispersion corresponds to a higher coefficient of variation. To quantify the variation of diversity, the coefficient of variation was calculated for each data set and compared among different indices. Biological indices like EUD-based TCP and NTCP formula derived by Gay and Niemierko (2007) were also computed as a vehicle to explain the outcome from different indices.

In summary, the wealth of data hidden in the DICOM RT objects was harvested to provide essential information for development of the CAE system and the CI_{DD} scoring system. The CAE along with the CI_{DD} were evaluated by comparing their performance to that of the manual evaluation method using conventional indices.

Chapter 5 Results

The CAE system along with the CI_{DD} that integrated both dosimetric and spatial importance of each voxel within the PTV was developed and evaluated. They will be reported as follows. Firstly, the implementation and functionality of the CAE and CI_{DD} systems will be described in Section 5.1, highlighting some special GUI features. Secondly, the CAE and CI_{DD} system performance evaluation results will be presented in Section 5.2.

5.1 CAE and CI_{DD} systems development

The aim of the CAE system was to provide a one-stop platform for automatic evaluation of IMRT plans for head-and-neck cancer. To gain a better appreciation of how the CAE system could streamline the IMRT plan evaluation workflow, a comparison of conventional and computer-aided methods was illustrated in Figure 5.1. With the use of CAE system, the manual DVH data analysis (step A2) and the slice-by-slice review (step A3), were combined into one single process (step B3). After entering the individualized plan acceptance criteria (step B2), the descriptive statistics and pertinent CT slices showing target underdosage and OAR overdosage could be seen at a glance.

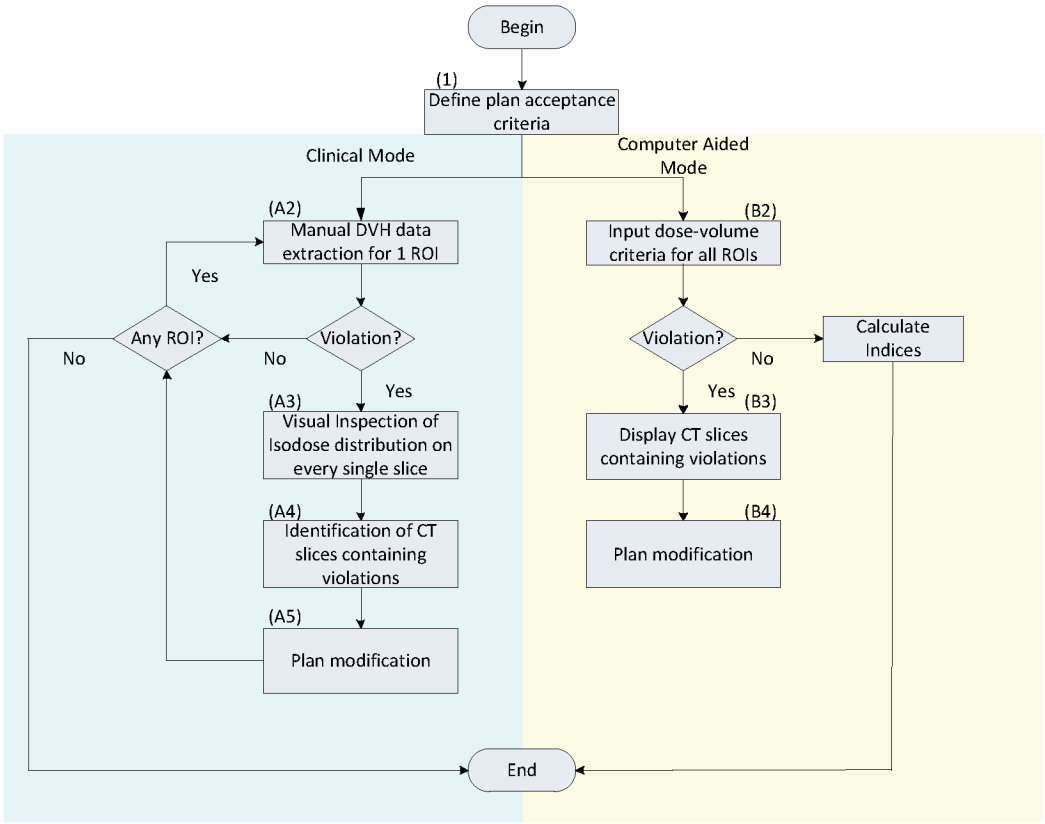

Figure 5.1. Comparison of conventional and computer-aided methods for evaluation of IMRT treatment plan.

The DICOM-based CAE system for automatic evaluation of IMRT plans was successfully developed, allowing better appreciation of resultant plans. To facilitate plan evaluation, three GUI panels were designed including (1) GUI for data entry and review (Section 5.1.1), (2) GUI for treatment plan evaluation (Section 5.1.2), and (3) GUI for calculation of different plan quality indices (Section 5.1.3). To illustrate the functionality of the CAE system, a sample IMRT plan for nasopharyngeal carcinoma was reviewed.

5.1.1 GUI for data entry and review

An IMRT plan is evaluated based on its ability to meet the user-defined dose volume criteria. In the GUI of this CAE system, the input data panel was divided

into two parts: the upper section gave a list of all relevant OARs whereas the bottom section showed details of each PTV, as represented in Figure 5.2. All OARs were enumerated according to their priority of plan acceptance consideration. As a general principle, top priority of importance was given to the neurological structures followed by optical organs, parotid glands and auditory structures. Considering a wide variety of treatment protocols available for adoption, the GUI panel allowing the creation of individual template was designed with flexibility in mind.

As shown in Figure 5.2, the panel contained five buttons which initiated separate functions of the programme. To kick off the plan evaluation process, the user selected an anonymized patient folder using the 'Load Plan' button in the upper left corner. A series of planning CT images together with the corresponding DICOM RT objects, namely the RT Structure Set and RT Dose objects were automatically loaded. The evaluation system provided two approaches to specify the dose volume criteria. User could select an existing template by clicking the second 'Open Template' button or define a new set of parameters by directly entering values into corresponding fields. If desired, all input fields could be saved for future use by clicking third 'Save Template' button.

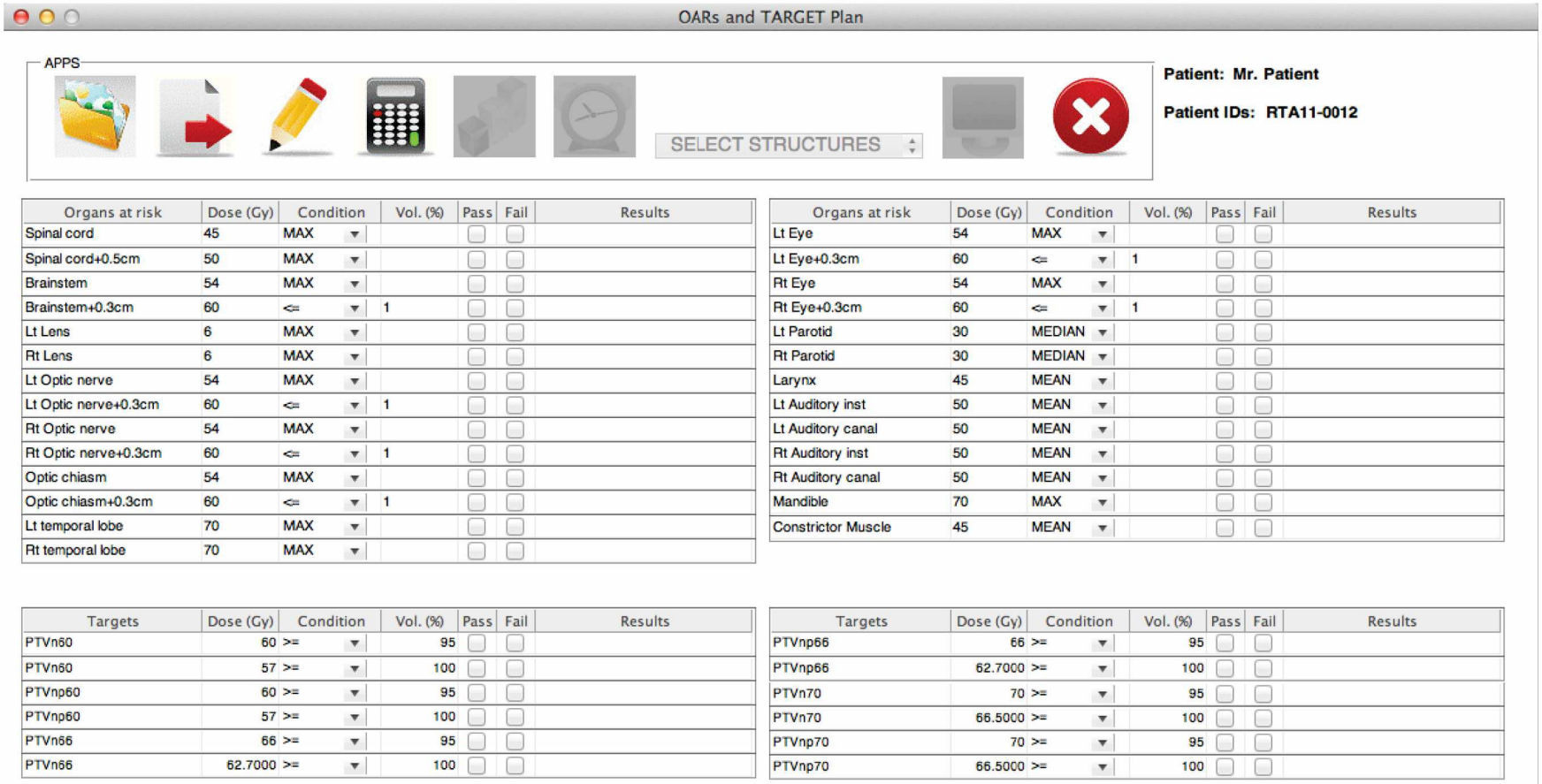

Organs at risk	Dose (Gy)	Condition	Vol. (%)	Pass	Fail	Results
Spinal cord	45	MAX				
Spinal cord+0.5cm	50	MAX				
Brainstem	54	MAX				
Brainstem+0.3cm	60	<=	1			
Lt Lens	6	MAX				
Rt Lens	6	MAX				
Lt Optic nerve	54	MAX				
Lt Optic nerve+0.3cm	60	<=	1			
Rt Optic nerve	54	MAX				
Rt Optic nerve+0.3cm	60	<=	1			
Optic chiasm	54	MAX				
Optic chiasm+0.3cm	60	<=	1			
Lt temporal lobe	70	MAX				
Rt temporal lobe	70	MAX				

Organs at risk	Dose (Gy)	Condition	Vol. (%)	Pass	Fail	Results
Lt Eye	54	MAX				
Lt Eye+0.3cm	60	<=	1			
Rt Eye	54	MAX				
Rt Eye+0.3cm	60	<=	1			
Lt Parotid	30	MEDIAN				
Rt Parotid	30	MEDIAN				
Larynx	45	MEAN				
Lt Auditory inst	50	MEAN				
Lt Auditory canal	50	MEAN				
Rt Auditory inst	50	MEAN				
Rt Auditory canal	50	MEAN				
Mandible	70	MAX				
Constrictor Muscle	45	MEAN				

Targets	Dose (Gy)	Condition	Vol. (%)	Pass	Fail	Results
PTVn60	60	>=	95			
PTVn60	57	>=	100			
PTVnp60	60	>=	95			
PTVnp60	57	>=	100			
PTVn66	66	>=	95			
PTVn66	62.7000	>=	100			

Targets	Dose (Gy)	Condition	Vol. (%)	Pass	Fail	Results
PTVnp66	66	>=	95			
PTVnp66	62.7000	>=	100			
PTVn70	70	>=	95			
PTVn70	66.5000	>=	100			
PTVnp70	70	>=	95			
PTVnp70	66.5000	>=	100			

Figure 5.2. Screenshot of input data panel setting up all acceptance criteria for targets and OARs.

When the dose-volume acceptance criteria for OARs and PTVs were specified, the plan evaluation process could be launched by clicking on the fourth 'Plan Evaluation' button. Through comparison with the user-defined constraints on a point-by-point basis, a series of binary decisions were made, each of which was either pass or fail. The results for each region of interest violating the acceptance criteria were listed enabling a quick-glance summary, as illustrated in Figure 5.3. By checking the details, one might conclude if the plan was satisfactory with the given treatment protocol. To close the GUI window, the rightmost panel 'Close' button could be pressed.

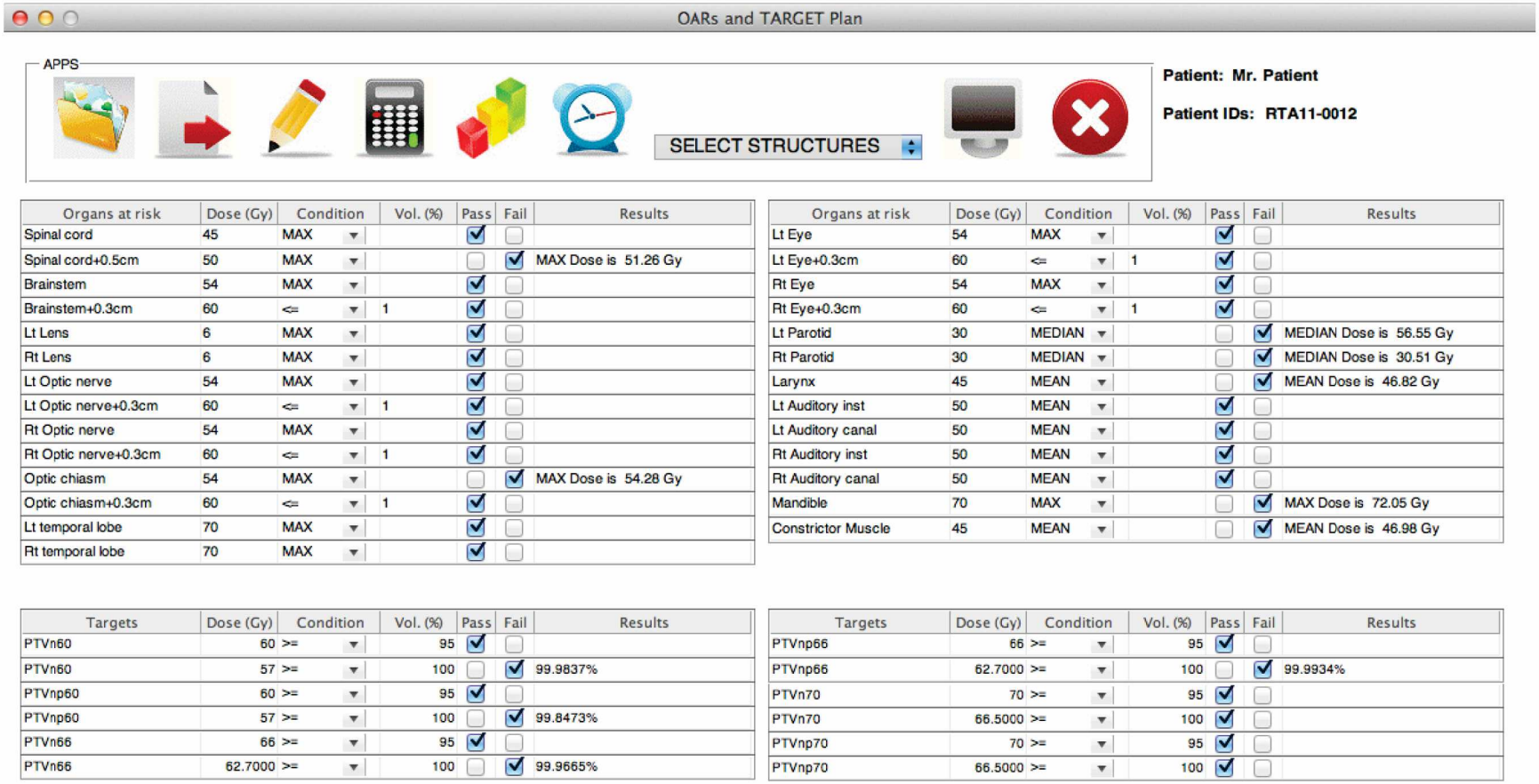

Organs at risk	Dose (Gy)	Condition	Vol. (%)	Pass	Fail	Results
Spinal cord	45	MAX		☑	☐	
Spinal cord+0.5cm	50	MAX		☐	☑	MAX Dose is 51.26 Gy
Brainstem	54	MAX		☑	☐	
Brainstem+0.3cm	60	<=	1	☑	☐	
Lt Lens	6	MAX		☑	☐	
Rt Lens	6	MAX		☑	☐	
Lt Optic nerve	54	MAX		☑	☐	
Lt Optic nerve+0.3cm	60	<=	1	☑	☐	
Rt Optic nerve	54	MAX		☑	☐	
Rt Optic nerve+0.3cm	60	<=	1	☑	☐	
Optic chiasm	54	MAX		☐	☑	MAX Dose is 54.28 Gy
Optic chiasm+0.3cm	60	<=	1	☑	☐	
Lt temporal lobe	70	MAX		☑	☐	
Rt temporal lobe	70	MAX		☑	☐	

Organs at risk	Dose (Gy)	Condition	Vol. (%)	Pass	Fail	Results
Lt Eye	54	MAX		☑	☐	
Lt Eye+0.3cm	60	<=	1	☑	☐	
Rt Eye	54	MAX		☑	☐	
Rt Eye+0.3cm	60	<=	1	☑	☐	
Lt Parotid	30	MEDIAN		☐	☑	MEDIAN Dose is 56.55 Gy
Rt Parotid	30	MEDIAN		☐	☑	MEDIAN Dose is 30.51 Gy
Larynx	45	MEAN		☐	☑	MEAN Dose is 46.82 Gy
Lt Auditory inst	50	MEAN		☑	☐	
Lt Auditory canal	50	MEAN		☑	☐	
Rt Auditory inst	50	MEAN		☑	☐	
Rt Auditory canal	50	MEAN		☑	☐	
Mandible	70	MAX		☐	☑	MAX Dose is 72.05 Gy
Constrictor Muscle	45	MEAN		☐	☑	MEAN Dose is 46.98 Gy

Targets	Dose (Gy)	Condition	Vol. (%)	Pass	Fail	Results
PTVn60	60	>=	95	☑	☐	
PTVn60	57	>=	100	☐	☑	99.9837%
PTVnp60	60	>=	95	☑	☐	
PTVnp60	57	>=	100	☐	☑	99.8473%
PTVn66	66	>=	95	☑	☐	
PTVn66	62.7000	>=	100	☐	☑	99.9665%

Targets	Dose (Gy)	Condition	Vol. (%)	Pass	Fail	Results
PTVnp66	66	>=	95	☑	☐	
PTVnp66	62.7000	>=	100	☐	☑	99.9934%
PTVn70	70	>=	95	☑	☐	
PTVn70	66.5000	>=	100	☑	☐	
PTVnp70	70	>=	95	☑	☐	
PTVnp70	66.5000	>=	100	☑	☐	

Figure 5.3. Screenshot of evaluation results for all regions of interests. In this example, spinal cord plus 0.5cm margin, optic chiasm, both parotid glands, mandible and constrictor muscle failed to meet the acceptance criteria.

5.1.2 GUI for treatment plan evaluation

As noted before, DVH analysis and isodose distribution review are indispensable to a comprehensive plan evaluation. The GUI for treatment plan evaluation allowed easy access of the close-up details for each region of interest that failed to fulfill the acceptance criteria. By selecting a specific region of interest from the list box, the related DVH curve along with other useful indicators such as maximum, mean, minimum doses and standard deviation were calculated and displayed explicitly (Figure 5.4). The drop-down menu allowed the user to choose and view a specific CT slice with overdose or underdose regions highlighted.

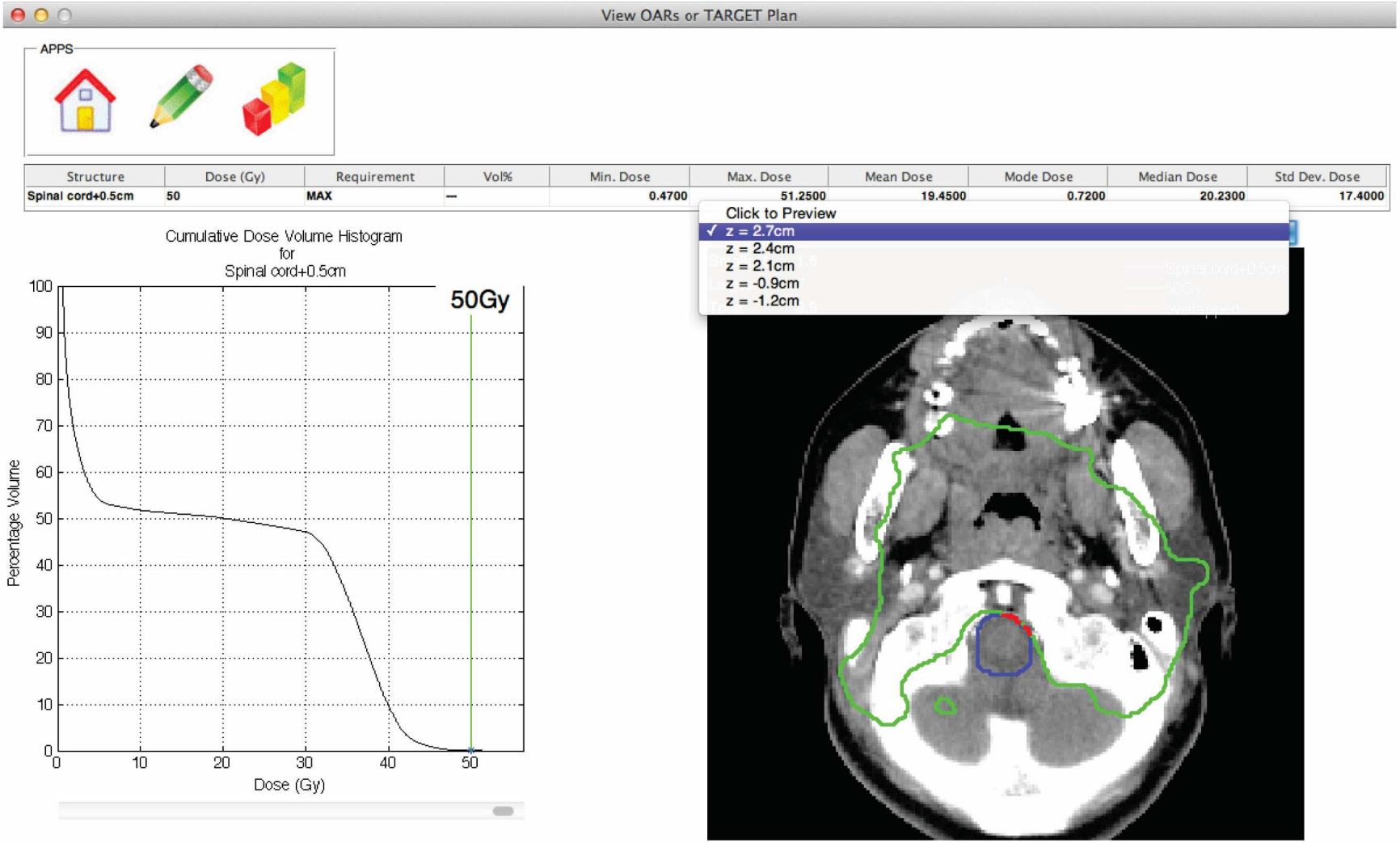

Figure 5.4. Screenshot of treatment plan evaluation page. By choosing a particular *z* position from a drop-down menu, the user can quickly assess for the hot and cold spots.

One of the most prominent features of the CAE system was its dynamic display of isodose lines allowing arbitrary selection of dose levels of interest. As demonstrated in Figure 5.5, the user could interactively drag the slider along the x-axis of the DVH to instantly change the display of isodose line overlaid on each CT slice. For prompt problem detection and correction, the direct relationship between the DVH data to the corresponding inhomogeneity regions on CT slices was shown, providing both flexibility and functionality for in-depth study of the spatial information of the dose-distribution.

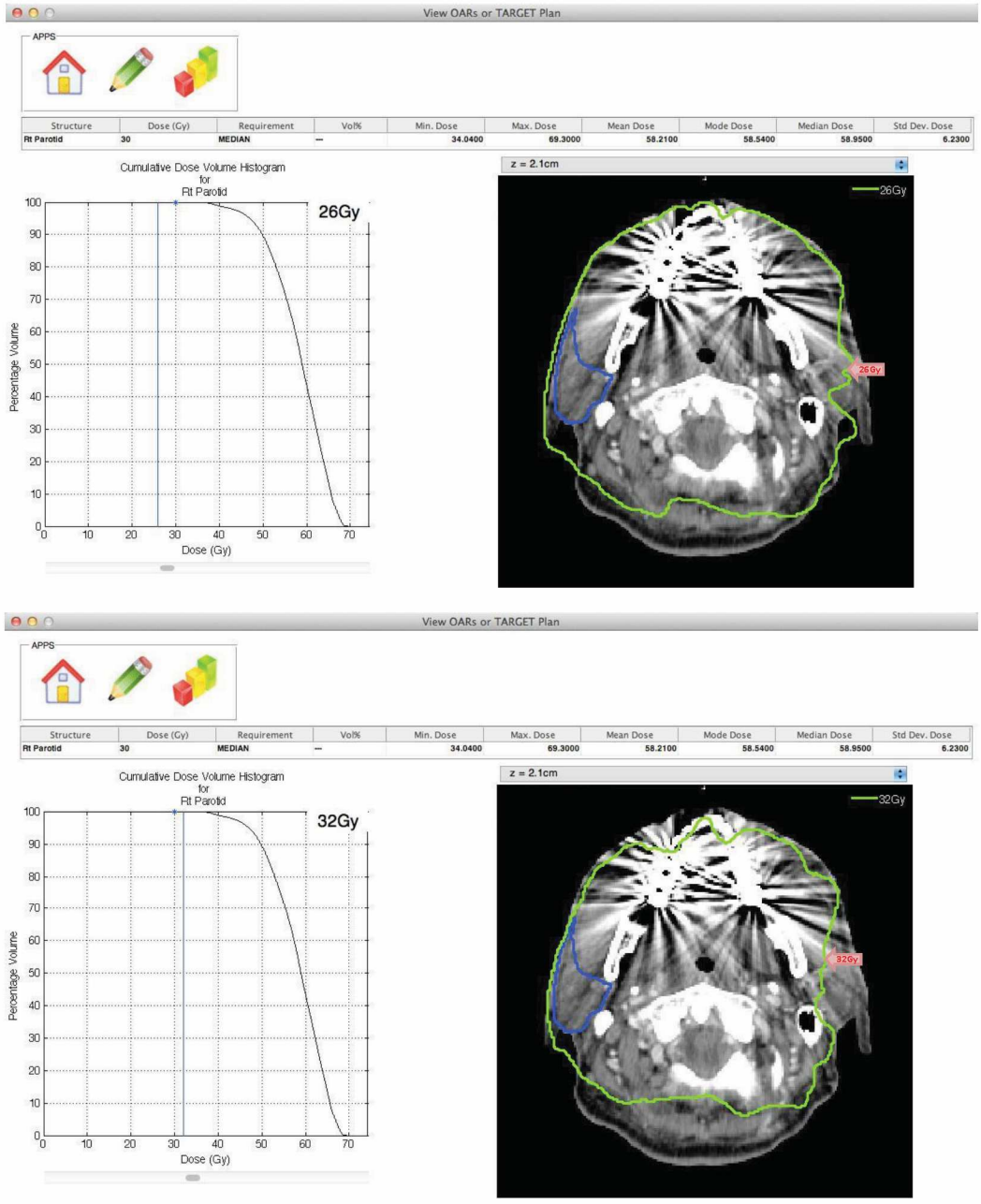

Figure 5.5. Screenshot demonstrating the interactive display of isodose line overlaid on each CT slice.

5.1.3 GUI for calculation of plan quality indices

Since the emergence of advanced radiotherapy technologies, the use of CI in the routine IMRT reporting was introduced in the ICRU Report 62 (1999). Many quantitative indices have been postulated to assist the evaluation of an IMRT plan. The GUI for calculation of plan quality indices provided an objective way

to quantify the plan quality, making direct comparison of IMRT plans possible (Figure 5.6). In addition to RTOG conformity index (CI_{RTOG}), healthy tissues conformity index (HTCI), conformation number (CN) and target coverage factor, this study offered a two-dimensional conformity index with dose and distance incorporated (CI_{DD}) for plan comparison. Slice-by-slice analysis of dose actually delivered to each PTV for comprehensive plan evaluation was also provided.

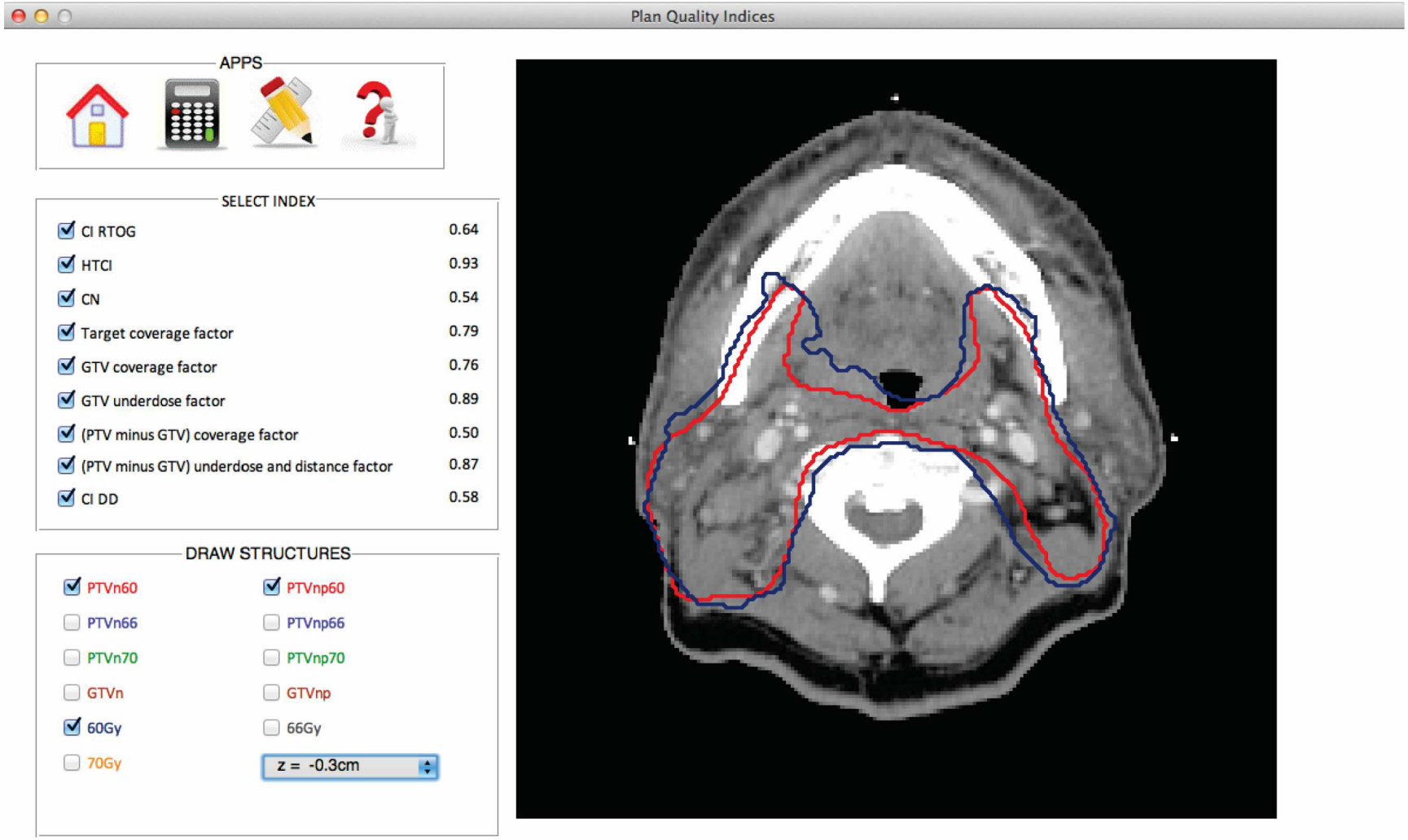

Figure 5.6. Graphical user interface for calculation of different plan quality indices. The PTV_{n60} and 60Gy isodose line are indicated by red and blue lines, respectively. All PTVs and prescription isodose lines could be shown on every CT slice by selecting their corresponding checkboxes.

5.2 Performance evaluation of CAE and CI_{DD} systems

Both structural and functional tests were implemented to assess the system performance. Technical verification results showed that program codes were well written. As mentioned in Section 4.1.4, thirty IMRT head-and-neck plans delivered between January 2005 and January 2006 in the Department of Clinical Oncology from a collaborative hospital were collected for overall system evaluation. Using conventional manual method, six planners (three with six years of experience in IMRT planning and three with less than two years of relevant experience) were asked to evaluate the 30 IMRT plans independently. They were taught to use the CAE system to ensure consistent treatment plan quality and unbiased performance evaluation. The specific DVH-based parameters of each OAR were extracted manually and the violations on each CT slice were marked out. The plans were then re-evaluated by the same planners aided by the CAE system. After importing each IMRT plan into the CAE system, automatic DVH analysis was performed. The sizes and locations of underdose and overdose regions were automatically determined and highlighted allowing easy detection.

5.2.1 Comparison between CAE-computed and manually extracted results

The CAE-computed DVH results were evaluated for 30 IMRT plans by comparison with manually extracted DVH data from treatment planning system. Discrepancy between DVH data extracted by manual and CAE methods was small, producing the NRMSD values of less than 0.05% for all OARs. The five OARs with relatively higher NRMSD values were brainstem, left and right lenses, optic chiasm and spinal cord (Table 5.1). Such small NRMSD values for all OARS indicated that CAE system did an equally good job as manual method. Detailed NRMSD results for all OARs were shown in Appendix 1.

Table 5.1. NRMSD values for five organs at risk measuring the differences between DVH data extracted by manual and CAE methods.

	brainstem		Left Lens		Right Lens		optic chiasm		spinal cord	
Plan	**Manual**	**CAE**	**Manual**	**CAE**	**Manual**	**CAE**	**Manual**	**CAE**	**Manual**	**CAE**
1	52.31	52.30	2.31	2.29	5.68	5.69	50.58	50.59	40.85	40.82
2	50.82	50.84	3.86	3.88	4.58	4.57	52.48	52.47	43.79	43.76
3	53.70	53.69	4.85	4.87	5.85	5.87	51.74	51.75	41.87	41.89
4	50.13	50.13	3.00	2.98	5.14	5.13	50.50	50.46	44.80	44.77
5	52.10	52.08	0.95	0.94	2.07	2.05	53.69	53.68	43.22	43.20
6	52.94	52.92	2.33	2.32	1.14	1.13	52.66	52.65	40.91	40.90
7	51.21	51.21	2.00	1.98	3.69	3.66	51.03	51.00	41.91	41.89
8	51.64	51.61	1.84	1.84	4.11	4.11	50.93	50.92	40.01	39.97
9	52.63	52.61	4.73	4.69	5.14	5.09	52.45	52.43	41.19	41.18
10	53.56	53.54	4.15	4.14	4.60	4.57	50.41	50.41	41.17	41.16
11	51.46	51.43	5.06	5.04	4.31	4.28	51.82	51.77	39.15	39.14
12	51.99	51.98	0.57	0.57	5.55	5.50	51.53	51.50	38.21	38.18
13	50.76	50.75	4.73	4.72	4.29	4.27	52.82	52.80	43.93	43.92
14	53.13	53.11	5.10	5.07	1.51	1.50	52.91	52.86	43.23	43.20
15	52.01	51.97	2.03	2.02	3.95	3.94	51.31	51.26	41.84	41.81
16	53.47	53.46	2.28	2.27	5.72	5.71	52.90	52.86	44.08	44.04
17	52.97	52.94	0.89	0.89	2.68	2.67	53.41	53.40	40.03	40.02
18	52.83	52.83	4.46	4.42	1.58	1.57	50.29	50.26	40.03	40.01
19	53.64	53.64	5.01	4.97	1.13	1.12	51.77	51.73	41.03	41.00
20	50.09	50.09	1.48	1.47	5.72	5.71	50.27	50.24	41.30	41.27
21	52.34	52.29	2.29	2.27	3.29	3.27	53.42	53.38	39.33	39.30
22	51.16	51.14	0.71	0.70	1.84	1.83	52.58	52.58	42.87	42.85
23	52.46	52.45	4.97	4.93	1.43	1.42	52.86	52.81	42.70	42.69
24	50.06	50.02	3.48	3.47	1.96	1.95	52.68	52.64	39.79	39.79
25	51.91	51.90	5.00	4.96	2.03	2.03	52.84	52.82	39.30	39.27
26	53.47	53.45	5.77	5.72	3.27	3.25	53.61	53.58	41.55	41.51
27	50.12	50.08	5.79	5.78	3.69	3.66	51.09	51.07	40.98	40.98
28	52.83	52.79	2.79	2.77	2.61	2.59	52.32	52.29	43.20	43.20
29	50.15	50.10	3.34	3.33	5.40	5.35	53.39	53.38	41.96	41.93
30	51.09	51.08	3.91	3.90	3.44	3.43	52.08	52.05	42.20	42.20
NRMSD (%)	0.016		0.010		0.011		0.026		0.009	

To evaluate the respective effect of spot size on region detection, Figure 5.7 provides a quantitative comparison of the performance of the CAE system against that of experienced and inexperienced planners on 30 IMRT plans. In the unassisted sessions, the experienced and inexperienced planners successfully identified 45.92% and 29.08% of total number of regions that failed to meet the acceptance criteria, respectively. Of these 30 IMRT plans, 92.57% of the regions violating the criteria were small-size spots with less than 100mm^3 in volume. No matter how experienced the planners were, tiny spots situated in the periphery of PTVs were more likely to be missed during manual plan evaluation. With the aid of the CAE system, the per-region detection performance for small-size spots was greatly improved by 2.36-fold and 3.99-fold for experienced and inexperienced planners, respectively.

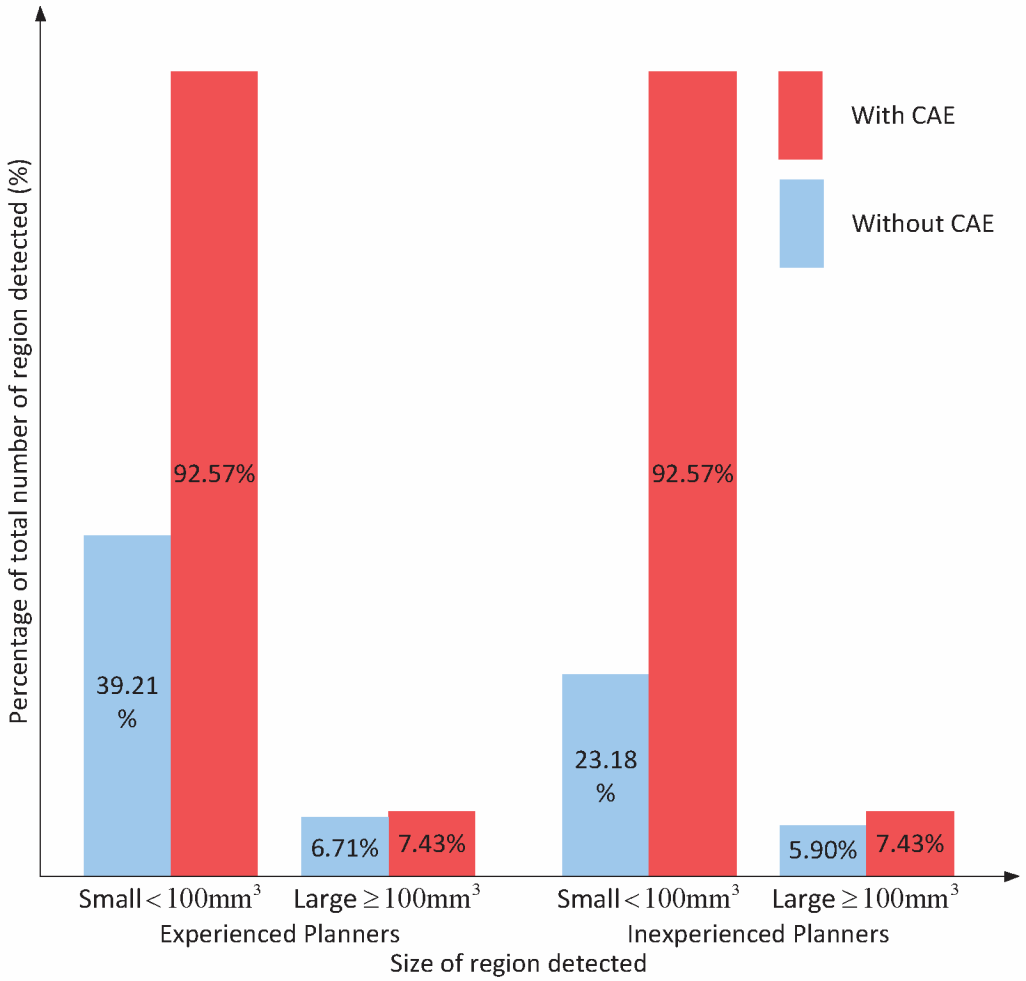

Figure 5.7. Quantitative comparison of the per-region detection performance of the CAE system between experienced and inexperienced planners.

5.2.2 Evaluation of CI_{DD}

Another thirty IMRT test plans were generated to quantify the benefits of the CI_{DD} scoring system. Three CT image data sets of nasopharyngeal carcinoma cases with slice thickness of 3mm were collected. Multiple PTVs were specified in nasopharyngeal (NP) and nodal regions, each with three different dose levels, namely PTV_{np60}, PTV_{np66}, PTV_{np70}, PTV_{n60}, PTV_{n66} and PTV_{n70}, respectively. For each of the three data set, 10 IMRT plans using simultaneously integrated boost were created by steadily decreasing the strictness of dose volume constraints for

PTV coverage (please refer to Section 4.2.6 for further details). In doing so, continuous plan degradation was expected offering worsen target coverage.

The use of CI_{DD} consisting of four discrete factors allowed planners to assess the dose distribution in greater depth. Coverage of multiple PTVs by various levels of prescribed dose was analyzed separately. Each factor was bounded by 0 and 1, greater value indicated superior plan. Figure 5.8 summarizes the results of different factors among the 10 plans of the first NPC patient. All factors suggested that plan 1 was the most superior in terms of target coverage. The first 8 plans provided nearly perfect GTV coverage without GTV underdosage. For plan 9 and plan 10, there was a drop in both GTV coverage and GTV underdosage factors, but the decrease was more pronounced in GTV coverage factor. Among the 10 IMRT plans, the (PTV minus GTV) coverage factor never reached unity suggesting that part of the target outside GTV always received less than the prescribed dose. The values of (PTV minus GTV) coverage factor declined gradually from 0.9 to 0.85 for the first five plans and then fell rapidly down to 0.4 for plan 10. On the other hand, the change in (PTV minus GTV) underdose and distance factor was gradual and subtle initially, but became obvious for the last 5 plans.

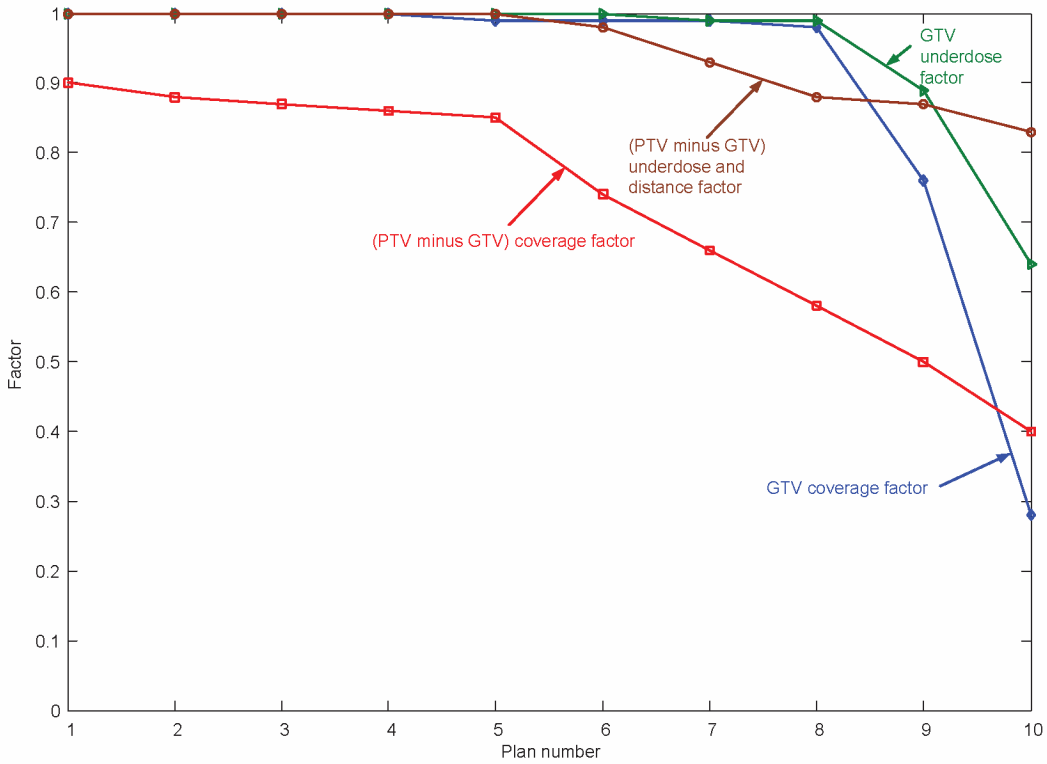

Figure 5.8. Graph showing the variation of different factors among 10 IMRT plans for the first NPC patient.

For the second NPC patient, the curve for GTV underdose factor stayed flat at 0.94 level among 10 IMRT plans (Figure 5.9). The GTV coverage factor remained high around 0.99 for the first 4 plans, then declined steadily to 0.58 in plan 8 but increased again to 0.64 in plan 10. The (PTV minus GTV) underdose and distance factor showed a gradual downward trend. On the other hand, there was a rapid decline in the (PTV minus GTV) coverage factor from plan 1 to plan 8 but picking up slightly for the last 2 plans.

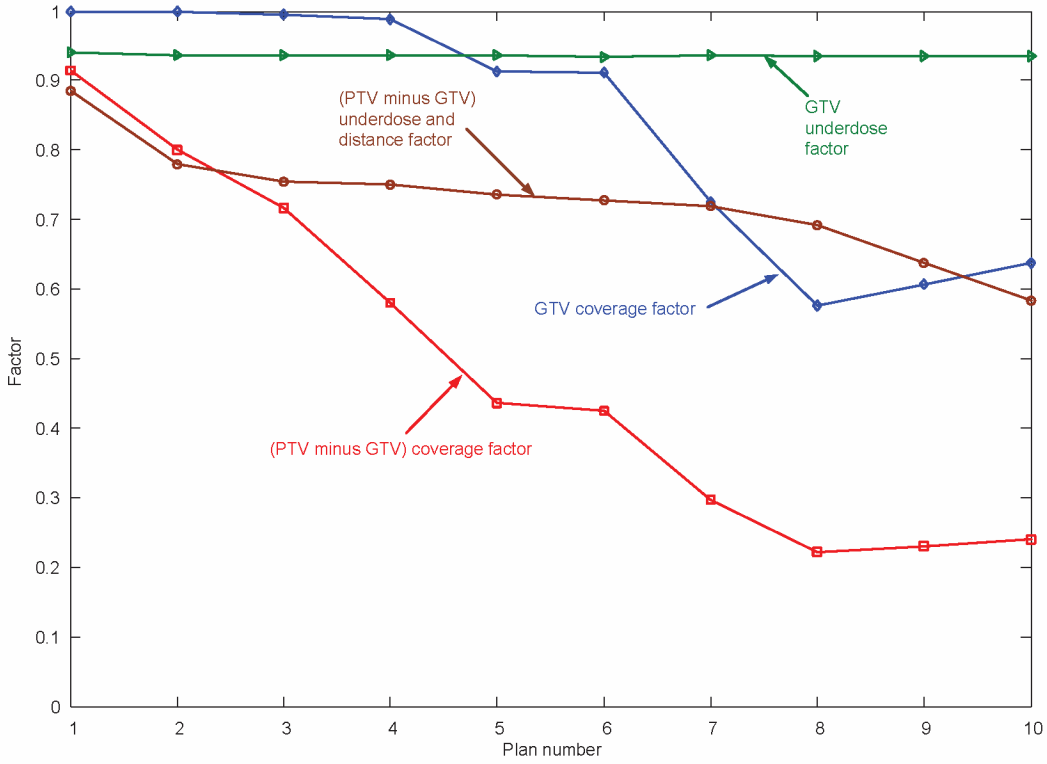

Figure 5.9. Graph showing the variation of different factors among 10 IMRT plans for the second NPC patient.

Figure 5.10 shows the variation of different factors among the 10 plans for the third NPC patient. The GTV underdose factor plateaued at a value close to 0.99 for the first 5 plans then dropped steadily to 0.67 for plan 10. In contrast, the (PTV minus GTV) underdose and distance factor showed a continuous gradual decrease among 10 plans. Both GTV coverage factor and (PTV minus GTV) coverage factor had similar decreasing trends but the drop was less marked for the latter.

As mentioned in Section 4.2.6, plans with increasing degree of degradation were generated for each NPC patient to assess the CI_{DD} scoring system including 4 discrete factors. For each factor, lower scores indicate worse plan quality. In line with expectations, the results for all three patients showed a general decreasing

trend from plan 1 to plan 10. By taking the spatial dose information into account, the target coverage for each subregion of PTV could be assessed separately. The results for all three NPC patients demonstrated that these 4 discrete factors could provide accurate rankings of plan quality by examining the relative importance of each cold spot within the PTVs.

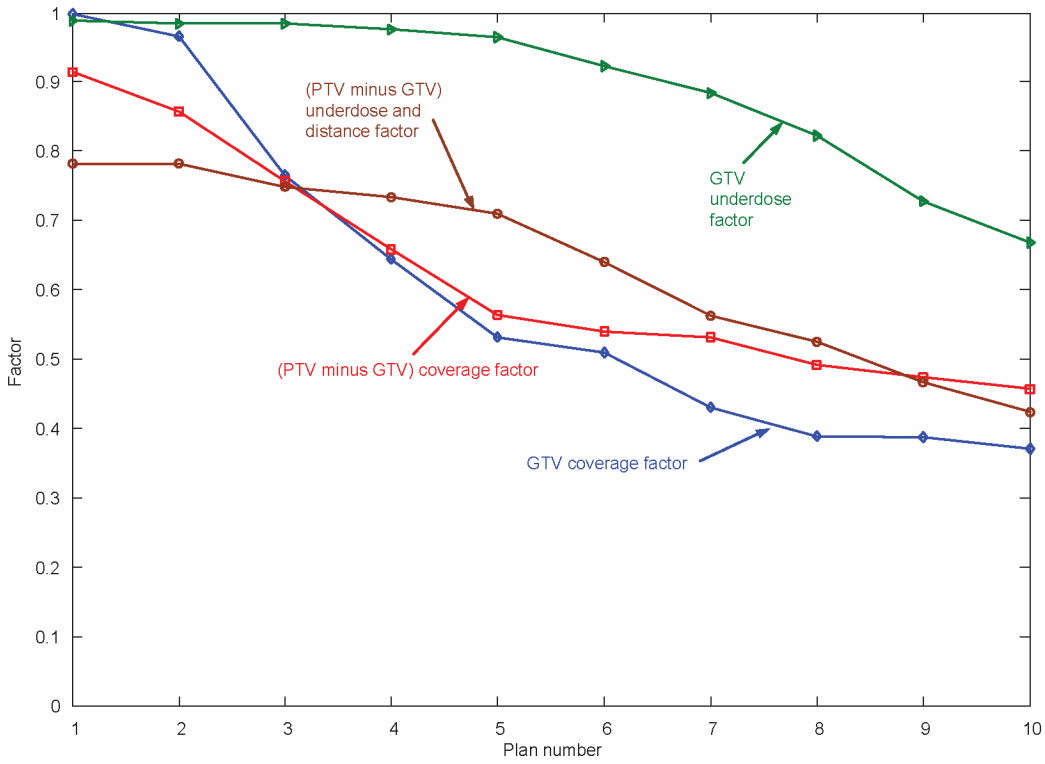

Figure 5.10. Graph showing the variation of different factors among 10 IMRT plans for the third NPC patient.

5.2.3 Comparison among CI_{DD} scores

To consolidate all four distinct factors into one CI_{DD} score, Euclidean distance was applied to describe the overall plan quality. In contrast to other conventional indices, lower CI_{DD} scores indicate better target coverage. The CI_{DD} score trends for three NPC patients were illustrated in Figure 5.11. For the first patient, the CI_{DD} scores climbed slowly from 0.1 to 0.15 for the first 5 plans, then soared to

1.02 for plan 10. Nearly sevenfold increase was observed from plan 5 to plan 10. For the second patient, the CI_{DD} scores went up gradually from plan 1 to plan 7 but levelled off for the last 3 plans. In contrast, the CI_{DD} scores for the third patient rose more steadily from 0.23 for plan 1 to 1.06 for plan 10. On the whole, the CI_{DD} scores increased accordingly with increasing plan number for all three NPC patients. Coherent with expectations, plan 1 was the most superior in terms of target coverage as evidenced by the lowest CI_{DD} score among 10 IMRT plans for each NPC patient.

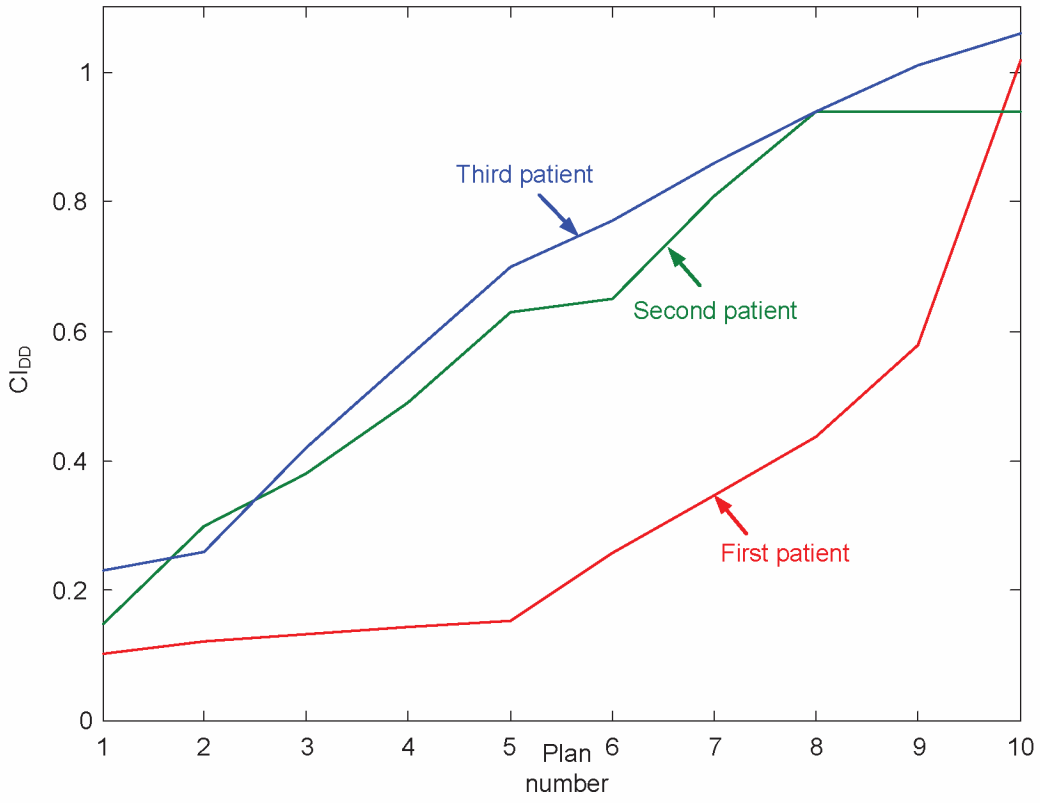

Figure 5.11. Graph showing the trend of CI_{DD} scores among 10 IMRT plans for three NPC patients.

5.2.4 Comparison with various conformity indices

With the use of CAE system, several conformity indices namely CI_{RTOG}, HTCI,

CN, target coverage factor and CI_{DD} were calculated for each plan. The coefficient of variance was computed for each index to compare their plan quality discerning power. Table 5.2 summarizes the scores of all indices and their coefficients of variance for the first NPC patient. For CI_{DD}, lower values indicate better plans while for the rest, higher values indicate better plans. The best plan suggested by CI_{RTOG}, target coverage factor and CI_{DD} was plan 1. Still, plan 3 and plan 4 had the highest scores of CN. Plan 10 was the most superior when ranking based on HTCI alone but the worst according to CI_{DD} index as well as others. Referring to Figure 5.8 again, plan 9 and plan 10 with undesirable grade 1 geographic miss were clearly clinically unacceptable. For the first NPC patient, the coefficients of variance of CI_{RTOG}, HTCI, CN, target coverage factor and CI_{DD} were 31.73%, 7.65%, 15.23%, 10.88% and 87.57%, respectively which indicated that the CI_{DD} index had the greater plan quality discerning power.

Table 5.2. Summary of various indices and coefficients of variance for the first NPC patient.

Plan no.	CI_{RTOG}	HTCI	CN	Target coverage factor	CI_{DD}
1	**1.37**	0.77	0.71	**1.00**	**0.1**
2	1.32	0.78	0.71	0.99	0.13
3	1.27	0.80	0.72	0.99	0.13
4	1.25	0.80	0.72	0.99	0.14
5	1.23	0.80	0.71	0.98	0.15
6	1.07	0.86	0.69	0.94	0.26
7	0.99	0.88	0.65	0.89	0.35
8	0.91	0.90	0.60	0.84	0.44
9	0.64	0.93	0.54	0.79	0.48
10	0.35	*0.94*	0.42	0.72	1.02
μ	1.04	0.85	0.65	0.91	0.33
σ	0.33	0.07	0.10	0.10	0.29
CV	31.73%	7.65%	15.23%	10.88%	87.57%

μ = mean, σ = standard deviation, CV = coefficient of variance

Scores of various indices and relevant coefficients of variance for the second and third patients were listed in Table 5.3 and Table 5.4. The coefficients of variance of CI_{RTOG}, HTCI, CN, target coverage factor and CI_{DD} for the second NPC patient were 38.4%, 8.7%, 14.57%, 14% and 46.09%, respectively (Table 5.3). While for the third NPC patient, the coefficients of variance of CI_{RTOG}, HTCI, CN, target coverage factor and CI_{DD} were 34.48%, 5.15%, 17.28%, 8.87% and 44.39% respectively (Table 5.4). Both sets of data showed that analysis of different indices could lead to different conclusions, indicating that special caution was required when evaluating treatment plans based on one specific index. Compared with other commonly used indices, the CI_{DD} always resulted in the largest coefficient of variance for all three NPC patients. It implied that CI_{DD} scoring system had the greatest power to rank rival IMRT plans.

Table 5.3. Summary of various indices and coefficients of variance for the second NPC patient.

Plan no.	CI_{RTOG}	HTCI	CN	Target coverage factor	CI_{DD}
1	**1.33**	0.74	0.65	**1.00**	**0.15**
2	1.30	0.81	0.66	0.96	0.30
3	1.26	0.86	0.69	0.94	0.38
4	1.23	0.90	0.71	0.90	0.49
5	1.12	0.94	0.72	0.83	0.63
6	0.96	0.93	0.69	0.83	0.65
7	0.82	0.86	0.58	0.74	0.81
8	0.73	*0.97*	0.54	0.70	0.94
9	0.39	*0.97*	0.52	0.70	0.94
10	0.36	*0.97*	0.46	0.70	0.94
μ	0.95	0.91	0.62	0.83	0.62
σ	0.36	0.08	0.09	0.12	0.29
CV	38.40%	8.70%	14.57%	14.00%	46.09%

μ = mean, σ = standard deviation, CV = coefficient of variance

Table 5.4. Summary of various indices and coefficients of variance for the third NPC patient.

Plan no.	CI_{RTOG}	HTCI	CN	Target coverage factor	CI_{DD}
1	**1.31**	0.71	0.65	**0.99**	**0.23**
2	1.30	0.79	0.68	0.98	0.26
3	1.24	0.85	0.71	0.94	0.42
4	1.19	0.82	0.72	0.90	0.56
5	1.15	0.81	0.72	0.84	0.70
6	0.93	0.81	0.68	0.83	0.77
7	0.82	0.80	0.54	0.82	0.86
8	0.54	0.83	0.52	0.80	0.94
9	0.42	*0.85*	0.49	0.80	1.01
10	0.36	*0.85*	0.44	0.79	1.06
μ	0.95	0.81	0.62	0.87	0.62
σ	0.33	0.04	0.11	0.08	0.30
CV	34.48%	5.15%	17.28%	8.87%	44.39%

μ = mean, σ = standard deviation, CV = coefficient of variance

5.2.5 Comparison with TCP and NTCP

The evaluation results were further validated by the calculation using equivalent uniform dose (EUD), EUD-based TCP and NTCP. All three NPC patients followed similar patterns from plan 1 to plan 10, as illustrated in Table 5.5 to Table 5.10. Some conclusions could be drawn from the data. First of all, the EUDs of all PTVs suggested that plan 1 was the most superior in terms of target coverage. The TCP values among 10 IMRT plans had a slight downward trend from plan 1 to plan 10. In contrast, the minimum EUDs of OARs were mostly found in plan 10, with the lowest NTCP. Nevertheless, the EUDs of all PTVs in plan 10 were much smaller as a result of large cold spots. As a whole, the results were in line with that of the CI_{DD} scores. For CI_{DD}, lower values indicate better plans.

Table 5.5. Summary of EUDs for the PTVs and TCPs of the 10 IMRT plans for the first NPC patient using units of gray (Gy).

Plan no.	EUD (in Gy)						TCP (PTV_{70})	CI_{DD}
	PTV_{np70}	PTV_{n70}	PTV_{np66}	PTV_{n66}	PTV_{np60}	PTV_{n60}		
1	71.58	71.97	68.94	68.98	65.95	64.48	88.77%	0.10
2	71.16	71.83	68.64	68.95	65.83	64.27	88.23%	0.13
3	71.25	71.75	68.64	68.88	65.78	64.03	88.25%	0.13
4	71.02	71.57	68.63	68.84	65.76	63.94	87.83%	0.14
5	70.79	71.40	68.63	68.80	65.73	63.85	87.42%	0.15
6	69.44	71.43	68.07	67.96	64.47	60.91	85.82%	0.26
7	69.87	71.33	67.50	66.75	63.50	58.86	86.25%	0.35
8	70.30	71.22	66.94	65.54	62.54	56.80	86.68%	0.44
9	69.41	70.33	66.77	65.28	62.43	56.79	84.58%	0.48
10	68.93	69.82	66.36	64.90	62.24	56.71	83.29%	1.02
μ	70.38	71.26	67.87	67.47	64.39	61.06	86.71%	0.33
σ	0.92	0.68	0.90	1.68	1.56	3.45	0.02%	0.29

μ = mean, σ = standard deviation

Table 5.6. Summary of EUDs for OARs and NTCPs of the 10 IMRT plans for the first NPC patient using units of gray (Gy).

Plan no.	Brainstem	NTCP (%)	Optic Chiasm	NTCP (%)	Left optic nerve	NTCP (%)	Right optic nerve	NTCP (%)	Left temporal lobe	NTCP (%)	Right temporal lobe	NTCP (%)
1	39.90	0.29	37.78	0.15	48.89	3.17	36.92	1.81	32.67	0.07	38.16	0.44
2	40.37	0.33	38.34	0.18	49.37	3.56	37.34	2.03	32.65	0.07	38.55	0.49
3	40.19	0.31	38.16	0.17	49.10	3.33	37.17	1.97	32.56	0.07	38.47	0.48
4	40.13	0.30	38.12	0.16	48.95	3.11	37.11	1.91	32.44	0.06	38.44	0.47
5	40.08	0.24	38.07	0.13	48.80	2.66	37.04	1.83	32.33	0.05	38.42	0.36
6	39.35	0.24	37.32	0.12	48.15	2.25	36.24	1.78	31.61	0.03	37.53	0.26
7	39.33	0.23	37.23	0.12	47.81	2.21	36.15	1.73	31.13	0.03	37.01	0.25
8	39.31	0.23	37.15	0.11	47.47	2.15	36.06	1.69	30.64	0.03	36.49	0.25
9	39.24	0.21	37.06	0.10	47.41	2.12	36.00	1.68	30.61	0.03	36.48	0.25
10	39.14	0.20	36.95	0.08	47.29	2.05	35.92	1.62	30.55	0.03	36.45	0.25
μ	39.70	0.26	37.62	0.13	48.32	2.66	36.60	1.81	31.72	0.05	37.60	0.35
σ	0.47	0.00	0.53	0.03	0.79	0.01	0.56	0.13	0.91	0.00	0.91	0.00

μ = mean, σ = standard deviation

Table 5.7. Summary of EUDs for the PTVs and TCPs of the 10 IMRT plans for the second NPC patient using units of gray (Gy).

Plan no.	EUD (in Gy)						TCP (PTV_{70})	CI_{DD}
	PTV_{np70}	PTV_{n70}	PTV_{np66}	PTV_{n66}	PTV_{np60}	PTV_{n60}		
1	73.98	73.98	69.75	69.39	68.00	67.03	92.25%	0.15
2	72.75	73.24	68.54	67.65	66.08	64.86	90.85%	0.30
3	71.77	72.24	67.70	66.87	65.26	64.05	89.21%	0.38
4	71.07	71.46	66.91	66.12	64.46	63.23	87.78%	0.49
5	70.06	70.53	66.04	65.35	63.77	62.65	85.65%	0.63
6	70.08	70.24	65.95	65.27	63.62	62.42	85.33%	0.65
7	69.48	69.95	64.95	64.04	62.85	61.63	84.22%	0.81
8	69.13	69.57	64.55	63.85	62.43	61.21	83.26%	0.94
9	69.21	69.56	64.41	63.54	62.32	61.05	83.34%	0.94
10	69.28	69.55	64.26	63.14	62.21	60.90	83.43%	0.94
μ	70.68	71.03	66.31	65.60	64.10	62.90	86.53%	0.62
σ	1.67	1.62	1.89	1.92	1.89	1.96	3.30%	0.29

μ = mean, σ = standard deviation

Table 5.8. Summary of EUDs for OARs and NTCPs of the 10 IMRT plans for the second NPC patient using units of gray (Gy).

Plan no.	Brainstem	NTCP (%)	Optic Chiasm	NTCP (%)	Left optic nerve	NTCP (%)	Right optic nerve	NTCP (%)	Left temporal lobe	NTCP (%)	Right temporal lobe	NTCP (%)
1	42.42	0.59	42.96	0.69	48.03	2.58	51.19	5.39	37.88	0.40	38.30	0.46
2	40.83	0.38	41.07	0.40	46.66	1.84	50.36	4.47	35.60	0.19	36.01	0.22
3	40.78	0.37	40.97	0.39	46.55	1.79	49.94	4.06	35.26	0.17	35.80	0.20
4	40.88	0.38	40.74	0.37	46.57	1.80	49.86	3.98	34.94	0.15	35.57	0.19
5	40.93	0.39	40.39	0.33	46.54	1.78	50.02	4.13	34.78	0.14	35.46	0.18
6	40.21	0.31	40.06	0.30	45.59	1.40	49.35	3.54	34.76	0.14	35.28	0.17
7	40.19	0.31	40.01	0.30	46.06	1.58	49.11	3.34	34.09	0.11	35.01	0.16
8	40.11	0.30	39.89	0.28	45.95	1.53	48.94	3.21	33.89	0.11	34.89	0.15
9	40.09	0.30	39.75	0.27	45.93	1.53	48.84	3.14	33.90	0.11	34.79	0.14
10	40.07	0.30	39.61	0.26	45.92	1.52	48.74	3.06	33.91	0.11	34.68	0.14
μ	40.65	0.36	40.54	0.36	46.38	1.73	49.63	3.83	34.90	0.16	35.58	0.20
σ	0.72	0.09	0.99	0.13	0.68	0.33	0.78	0.73	1.21	0.09	1.05	0.09

μ = mean, σ = standard deviation

Table 5.9. Summary of EUDs for the PTVs and TCPs of the 10 IMRT plans for the third NPC patient using units of gray (Gy).

Plan no.	EUD (in Gy)						TCP (PTV_{70})	CI_{DD}
	PTV_{np70}	PTV_{n70}	PTV_{np66}	PTV_{n66}	PTV_{np60}	PTV_{n60}		
1	72.14	72.23	68.14	69.02	66.05	66.29	89.53%	0.23
2	71.31	71.62	67.47	68.42	65.14	65.48	88.19%	0.26
3	70.31	71.30	66.72	67.78	64.33	64.71	86.78%	0.42
4	70.06	70.27	66.68	67.72	64.17	64.38	85.35%	0.56
5	69.86	69.03	66.22	67.14	63.86	64.10	83.48%	0.70
6	70.10	68.49	66.00	66.83	63.51	63.63	82.99%	0.77
7	69.97	68.49	65.93	66.69	63.53	63.47	82.83%	0.86
8	69.09	68.83	65.77	66.68	63.23	63.43	82.17%	0.94
9	69.69	68.51	65.61	66.45	63.26	63.15	82.50%	1.01
10	69.80	67.94	65.49	66.39	63.09	62.95	81.74%	1.06
μ	70.27	69.67	66.40	67.31	64.02	64.16	84.56%	0.62
σ	0.87	1.55	0.86	0.89	0.95	1.08	2.75%	0.30

μ = mean, σ = standard deviation

Table 5.10. Summary of EUDs for OARs and NTCPs of the 10 IMRT plans for the third NPC patient using units of gray (Gy).

Plan no.	Brainstem	NTCP (%)	Optic Chiasm	NTCP (%)	Left optic nerve	NTCP (%)	Right optic nerve	NTCP (%)	Left temporal lobe	NTCP (%)	Right temporal lobe	NTCP (%)
1	44.91	1.17	49.67	3.81	50.70	4.83	52.18	6.69	42.98	1.79	39.08	0.58
2	44.41	1.02	49.86	3.99	50.12	4.23	51.31	5.53	42.12	1.41	38.42	0.47
3	44.46	1.04	49.71	3.85	49.95	4.07	51.28	5.49	41.61	1.22	38.63	0.50
4	44.67	1.10	49.92	4.04	50.33	4.44	51.12	5.30	41.71	1.26	37.95	0.41
5	44.68	1.10	49.84	3.96	50.12	4.23	50.67	4.79	41.55	1.20	37.80	0.39
6	45.01	1.20	49.32	3.51	50.04	4.16	50.26	4.36	41.40	1.15	37.73	0.38
7	45.15	1.25	49.33	3.52	50.12	4.23	50.38	4.49	41.51	1.19	37.76	0.38
8	45.22	1.27	49.19	3.41	49.84	3.97	50.18	4.29	41.27	1.11	37.73	0.38
9	43.81	0.87	49.56	3.72	49.57	3.73	50.25	4.36	40.97	1.02	37.31	0.33
10	44.20	0.97	49.08	3.32	49.59	3.74	50.07	4.18	40.91	1.00	37.31	0.33
μ	44.65	1.10	49.55	3.71	50.04	4.16	50.77	4.95	41.60	1.23	37.97	0.42
σ	0.44	0.13	0.30	0.26	0.34	0.32	0.68	0.80	0.60	0.23	0.57	0.08

μ = mean, σ = standard deviation

5.2.6 Impact of use of CAE and CI_{DD} on plan evaluation time

Mixed-design analysis of variance (ANOVA) was adopted to analyze the effect of use of CAE system and level of experience of planners on IMRT plan evaluation time. Results found that interaction was present between the evaluation time and level of experience of planners ($p < 0.005$) as illustrated in Figure 5.12 where the lines were not parallel. With the aid of the CAE system, the average evaluation time was reduced from 800.1s to 423.7s, regardless of the level of experience. The mean evaluation time for inexperienced planners significantly decreased from 968.27s to 470.23s with and without the use of CAE system, respectively. Meanwhile, the CAE system could help experienced planners reduce the evaluation time from 631.92s to 377.17s. The use of CAE system had statistically greater impact on evaluation time for inexperienced planners.

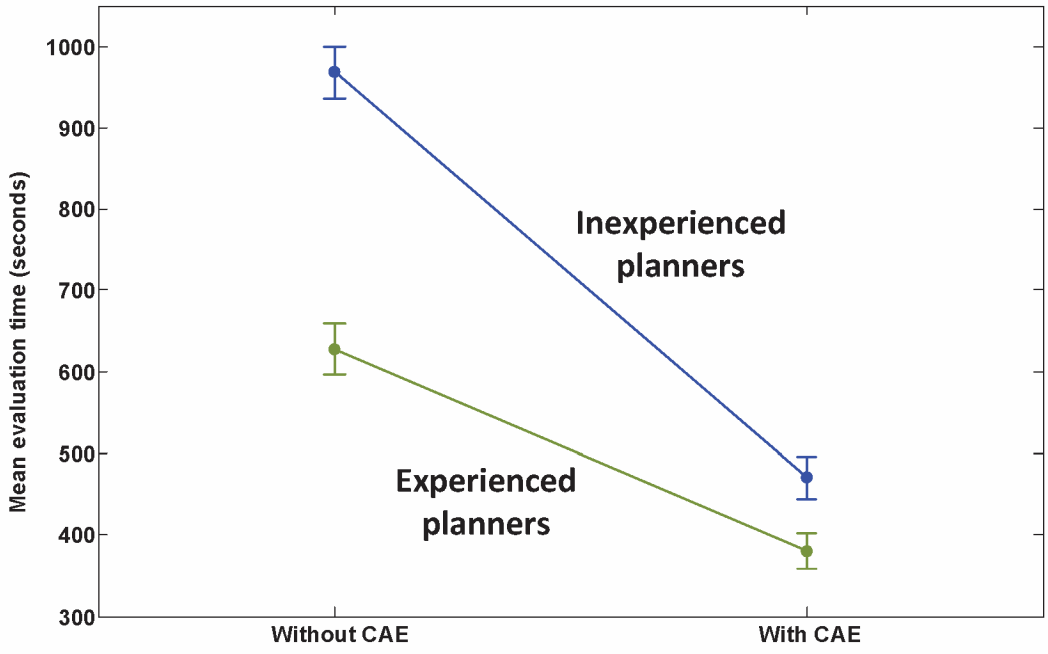

Figure 5.12. Interaction plot of the impact of use of CAE system and level of experience on evaluation time.

To summarize, the CAE and CI_{DD} systems were successfully designed, implemented and evaluated. Three GUI were specifically designed to support the IMRT plan evaluation and decision making process. The planners could set up the plan acceptance criteria according to individual needs and preferences. The CAE-extracted DVH data agreed closely with those obtained manually, resulting in NRMSD of less than 0.05% for all OARs.

For all three NPC patients, there was a fairly good agreement between the CI_{DD} and EUD-based TCP values. Higher CI_{DD} scores were associated with lower TCP values. Plan 1 for each patient with the most superior target coverage yielded the highest TCP and the lowest CI_{DD}. Whereas severe target underdose was observed for each plan 10, giving the lowest TCP and hence the highest CI_{DD}. The impact of using the CAE system on IMRT plan evaluation time was significant. Regardless of the level of experience, a 1.88-fold time reduction was achieved with the use of CAE system.

Chapter 6 Discussion and Conclusion

The use of CAE system along with the CI_{DD} would have a profound impact on maintaining consistent IMRT plan quality and reducing evaluation time for both inexperienced and experienced planners. The CI_{DD} scoring system also yielded promising results which were in line with the EUD values. The practical implications of these findings, potential benefits and ethical issues will be considered.

6.1 Development and evaluation of the CAE system

The comprehensive evaluation of an IMRT plan requires an in-depth analysis of DVHs, detailed review of isodose distribution and careful examination of various physical and biological indices. Owing to erroneous perception, time constraints, oversight, inexperience or fatigue, planner might overlook small-size hot and cold spots during slice-by-slice isodose review and neglect some important DVH statistics. Therefore, quantitative and effective quality control of the IMRT plan development process is of great importance.

In this study, the CAE system with CI_{DD} was successfully developed allowing automation of the plan evaluation process done in a precise and efficient manner. Unlike Pyakuryal's design (2010), the CAE system was not limited to the comparison of DVH data. This CAE system interactively guided planners through the plan evaluation process. To streamline the IMRT planning workflow, the functions provided by the CAE system were reasonably broad allowing (1) input of DICOM CT images and DICOM-RT objects from any treatment planning system, (2) entry of customized plan acceptance criteria, (3) generation

of evaluation results, (4) side-by-side display of DVHs and specific CT images with hot and cold spots and (5) quantitative analysis of plans based on both physical and biological indices. In line with Zhao's software (2010), this CAE system also incorporated spatial information into the plan evaluation process. To go one step further, a single CI_{DD} index was assigned to make plan comparison more direct and objective.

As a knowledge-based decision support tool, the impact of using treatment-plan-surface models in rival IMRT plan comparison was also studied (Zhang et al., 2010). This concept was extended by Zhu et al. (2011) who established an adaptive IMRT plan quality evaluation system tool to provide the best estimate of critical organ sparing. By comparing the geometric configurations, similar past cases were best used to teach planners about realistic decision-making. However, these machine learning tools did not provide any index which could be objectively computed and compared. This study was intended to fill these gaps by constructing an automatic IMRT plan evaluation system with CI_{DD} scores to aid planners in selecting an optimal IMRT plan with adequate target coverage.

Since DVH statistics could provide key information for plan evaluation, careful evaluation of the accuracy of DVH computation was essential (Henríquez et al., 2008 and Gossman et al., 2010). The report of Task Group 53 of the American Association of Physicists in Medicine (AAPM) also recommended the DVH accuracy tests for the quality assurance of treatment planning systems. Resolution of the dose and delineation grids used was the major factor that contributes to the accuracy of the DVH calculation (Ebert et al., 2010). In this

study, the CAE-computed DVH data was compared against the manually extracted data from the treatment planning system for 30 IMRT plans. The results were in excellent agreement with less than 0.05% discrepancy. The CAE system performance was comparable to that of the histogram analysis program developed by Pyakuryal et al. (2010) and conformed to the AAPM Task Group 53 accuracy recommendations.

Both computer-aided detection (CAD) and decision support systems were designed to improve the accuracy and consistency of physicians' interpretation and decision by providing a computerized second opinion (Brenner et al., 2006). Similarly, the CAE system could bring obvious benefits by alerting the planners to potential areas of concern. However, it is important to be cautious about the hidden pitfalls of medical malpractice situations. The CAE system was not intended to replace the planners and oncologists who should make the final fine-tuned decisions. Over-reliance on automation could have drastic consequences leading oncologists to be less vigilant and thorough in their IMRT plan evaluation processes. No doubt, education and training of planners and oncologists played a crucial role for success in the use of CAE system.

This study suggested that the CAE system could boost the performance of even an experienced planner in evaluating an IMRT plan, having the greatest impact on identification of small-size cold spots. The average plan evaluation times for experienced planner without and with CAE system were 631.92s and 377.17s, respectively. It was observed that the novice planner could not stay vigilant when they were not assisted. As a training tool, the CAE system could direct their attention to the regions of greater risk and reduce their average evaluation times

from 968.27s to 470.23s. Regardless of the level of experience, the CAE system could shorten the evaluation time by 1.88-fold, demonstrating the practical value of the system. Yet, the actual evaluation time could vary substantially for each case, depending on the number of CT images containing violation and the level of experience of planners.

Previous CAD research defined expert opinions as gold standard for evaluating the performance of a CAD system. However, experts could make mistakes in judgement and reach their limits of visual perception (Papamichail and French, 2005). It was noteworthy that detection of each near-miss spot could be life-saving. As a part of the plan review process, the CAE system could serve as an effective evaluation tool for uncovering the near misses at an earlier stage in the planning process and speeding production of quality plans.

6.2 Design and evaluation of the CI_{DD} scoring system

Another objective of this study was to design and evaluate a new CI_{DD} scoring system for evaluation of cold spots in targets. To incorporate patient-specific spatial dose information, the CI_{DD} scoring system is a geometry-based physical index enabling customized plan evaluation.

It was widely accepted that GTV was likely to have higher malignant cell density than the remainder of the PTV (Tomé et al., 2002). Since the locoregional failure rate was significantly related to the minimum dose in the GTV, the assumption of equal merit for different subregions inside PTV was inadequate (Ng et al., 2011). Cold spots should be at the periphery of PTV, as far from the GTV as possible.

Different distribution of underdosed volumes could lead to different tumor control probability outcomes. Whenever underdosage is present, it is important to know the magnitude, location and volume of the low dose regions.

By taking the spatial information into account, the relative importance of each cold spot within the subregions of the PTVs could be examined using the CI_{DD} scoring system including 4 discrete factors. Typically each factor equals to unity for an ideal plan, whereas the deviation from unity refers to underdose treatments in the corresponding region. In contrast, there is an inverse relationship between CI_{DD} score and plan quality. The smaller the value of CI_{DD}, the better is the overall target coverage. As a result, a plan with cold spots centrally located within the PTV should result in higher CI_{DD} score than the other with more acceptable cold spots on the periphery of the PTV further away from the GTV.

As discussed in Chapter 2, conformity index firstly proposed by the Radiation Therapy Oncology Group in 1993 (CI_{RTOG}) was defined as the ratio of the prescription volume to the target volume. The RTOG defined three categories of conformity index protocol compliance. An index between 1 and 2 is considered a treatment plan of acceptable dose conformity. Plans with a conformity index value between 2.0 and 2.5 or between 0.9 and 1.0 are classified as having minor deviations. An index less than 0.9 or more than 2.5 is considered to be a major violation. Figure 6.1 shows the trend of different conformity indices among 10 IMRT plans for the first NPC patient. This typical example could clearly demonstrate the weaknesses of each existing index. Plan numbers for each NPC patient are represented on the horizontal axis while the vertical axis shows the index value for each plan. As shown in Figure 6.1, the first 7 plans met the

RTOG guidelines with index between 1 and 2 while plans 8 to 10 were classified as having major violations with CI_{RTOG} values less than 0.9. By ignoring the degree of overlap between the prescription volume and target volume, false perfect score of CI_{RTOG} could be attained in the extreme cases of nonconcordance of target and treated volume. Planners may unwittingly accept and approve these plans.

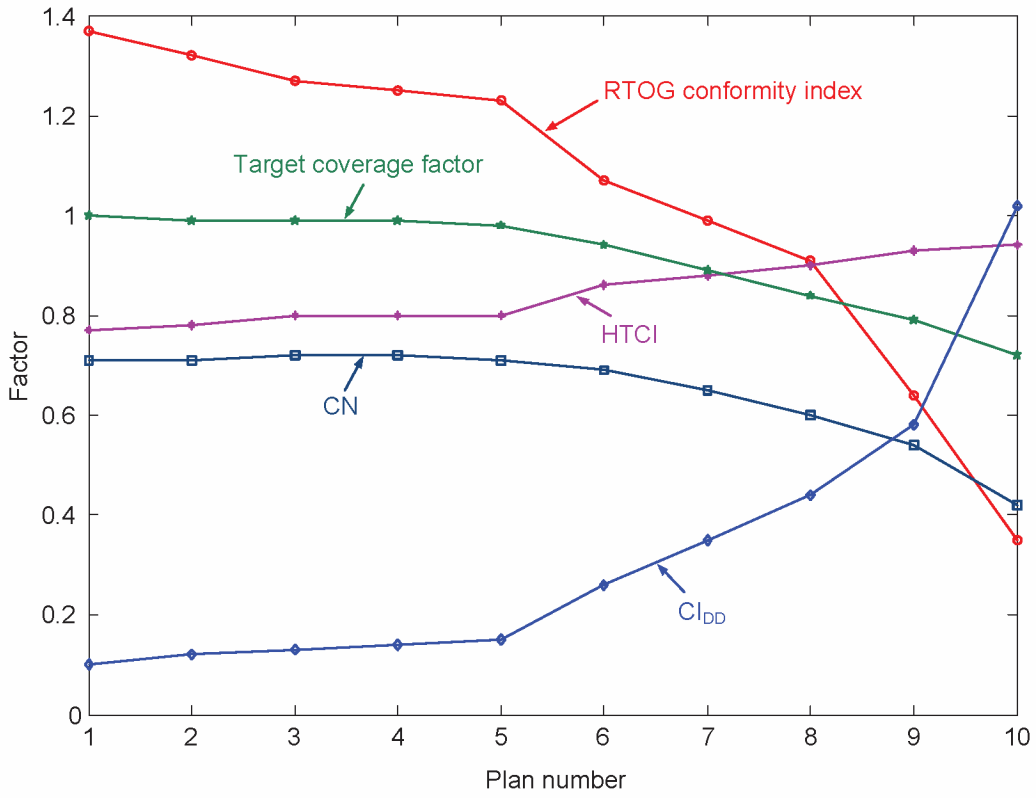

Figure 6.1. Graph showing the trend of different physical indices among 10 IMRT plans for the first NPC patient.

As an indirect measure of the irradiation of normal tissues, healthy tissues conformity index proposed by Lomax and Scheib (HTCI) was defined as the ratio of target volume covered by the reference dose to the total reference isodose volume. Higher HTCI corresponds to better normal tissue sparing. By definition,

HTCI of less than 0.6 is objectively considered to be non-conformal. As illustrated in Figure 6.1, applying the HTCI alone could lead to the conclusion that plan 10 was the most superior. However, clinical judgment showed the opposite. In this case, the HTCI values of larger than 0.7 were typically attainable for all IMRT plans. Major drawbacks of HTCI are that it takes into account exclusively the irradiation of healthy tissues and does not address the issue of target dose conformity. Obviously, an oversimplification could be made when ranking solely based on the HTCI.

Conformation number (CN) postulated by Van't Riet (1997) allowed quantitative evaluation of the tradeoffs between target coverage and critical organ sparing. As either the target underdosage or normal tissue overdosage occurs, the CN value decreases to avoid false positive results. However, no acceptable limit for CN was defined. For the first NPC patient, the CN values were relatively constant for the first 5 plans (Figure 6.1). The shortcoming of this index was that multiple plans with vastly differing clinical outcomes could give the same CN value. Like the CN, deviation from unity could be attributed to either insufficient target coverage or inadequate organ sparing.

Target coverage factor by Leung et al. (2007) evaluated the compliance with treatment protocol by taking all PTV check point doses into account. With a similar pattern to the CN, comparatively subtle variation in target coverage factor was observed among the 10 IMRT plans (Figure 6.1). It is obvious that the target coverage factor fails to account properly for the relative position of cold spots with respect to the GTV. In other words, large target coverage factor is no

guarantee for a good plan. Clearly, vigilance is required when evaluating treatment plans based on one specific index.

The ICRU Report 50 (1993) recommended a range of –5% and +7% of the prescribed dose for target dose homogeneity. However, it is widely recognized that this is a difficult goal to achieve in complex IMRT dose distribution. At present, there are some variations in IMRT dose prescription and reporting. It is more common to use either 95% or 98% coverage of the PTV for stating prescription dose, permitting as much as 5% of the PTV to be underdosed. The danger of cold spots could be avoided if the minimum dose delivered to the target is also stated as part of the prescription. It is an accepted norm that all of the target volume must lie within the 95% isodose line whenever the PTVs does not encroach upon the sensitive critical organs. Furthermore, Tomé and Fowler (2002) proposed the employment of EUD constraint to avoid the deep cold spots in target DVH. Later, the concept of tail EUD was introduced as an indicator of target cold spots (Bortfeld et al., 2008). It is hoped that introduction of the CI_{DD} scoring system into routine plan evaluation and reporting processes could continue the efforts of keeping an eye on undesirable deep cold spots.

Feuvret et al. (2006) emphasized that a single index may not be a good indicator as it might lead to omission of essential information. Both target coverage factor and EUD of PTVs were criticized for their insensitivity to the spatial location of the cold spots. Their averaging effect could lead to an underestimation of the risk of locoregional tumor relapse due to GTV underdosage. In this study, the CI_{DD} scoring system containing 4 discrete factors was specially designed to address these issues. By taking the spatial dose distribution into account, the relative

importance of each cold spot within the PTVs could be distinguished using 4 discrete factors. The CI_{DD} scoring system could provide more comprehensive information on overall target coverage, thereby reducing the risks of reaching false conclusions. With the greatest coefficient of variance in comparison with other existing indices, the CI_{DD} scoring system could improve the plan quality discerning power and help planners select a plan with a preferable spatial dose distribution.

All in all, the use of physical and radiobiological indices is only indicative figures. It is important to emphasize that clinical judgment and experience remain fundamental in making a final decision for the best interest of the patient. The CI_{DD} scoring system was successfully developed to incorporate patient-specific spatial dose information and provide a geometry-based physical index for plan evaluation. Apart from the dose penalty factor, a distance based exponential function was employed to vary the penalty weight associated with the location of cold spots within the PTVs. It is expected that the plan quality and consistency could be guaranteed by the use of the CI_{DD} scoring system.

6.3 Limitations of the study

There are five noteworthy limitations of this study. Firstly, the CI_{DD} scoring system was only evaluated based on the dosimetric data but not on the clinical outcomes such as follow-up data. It is worth doing further research by exploring the correlation between the CI_{DD} scoring system and the treatment outcome.

Secondly, Gaussian function was applied to penalize the underdose regions

similar to that described in Miften's study (2004). Nevertheless, empirical evidence in this regard was rather scanty. Further radiobiological research is expected to provide a closer look at the effect of cold spots on tumor control.

Thirdly, equal weights were assigned to four discrete factors namely GTV coverage factor, GTV underdose factor, PTV minus GTV coverage factor and PTV minus GTV underdose and distance factor. It was assumed that equal factor has relatively equal clinical importance. However, the differential weighting effect should also be examined in order to have a complete picture.

Fourthly, the CI_{DD} scoring system might not be the best representation of the plan quality since it did not account for the biological impact of the dose deficit. Although the tumor cell and radiobiology parameters carry large uncertainties, they could provide an additional guideline for selection of plan and estimation of therapeutic outcomes.

Lastly, the sample size was relatively small in this study. As a result, the samples might not be a good representation of the larger population making it harder to draw an unbiased conclusion. Future work should increase the sample size and, consequently, increase the statistical power.

6.4 Recommendations and future research

In the internet era, mobile telemedicine systems flourish. The growth and development of information technology in medical imaging and informatics has led to wide application of an electronic patient record system. Utilizing the

electronic patient record as a web-based platform, this CAE system can be a tool integrated to the electronic patient record to allow automatic IMRT plan evaluation in any web browser.

Based on the follow-up data on patients receiving IMRT, cases with early local relapse could be selected in future study. Large-scale correlation analysis between outcome of radiotherapy and the CI_{DD} scores could be done for these patients. The acceptable range of CI_{DD} values for routine clinical practice would be determined in future studies.

Further refinements of the CI_{DD} model are necessary. Firstly, it would be better to reverse the CI_{DD} model so that a better plan could yield higher score. For example, CI_{DD} could be calculated as the mean of four discrete factors. Secondly, differential weights should be assigned to each discrete factor according to their clinical importance. For example, higher weighting factor for GTV coverage factor and GTV underdose factor could be applied in the CI_{DD} calculation.

Recognizing the importance of subjective quality assessment, user satisfaction survey should be conducted amongst oncologists, physicists and dosimetrists in the future study offering extensive feedback for future program improvement.

As a further refinement of the CAE system, a graphical presentation summarizing the degree of sparing of organs at risk (OARs) and CI_{DD} score could be included for plan evaluation. One major benefit is its ability to simultaneously compare multiple plans and multiple critical structures, clearly depicting the tradeoffs between target coverage and OARs sparing.

Taking advantage of open architecture, the DICOM-based CAE system with CI_{DD} could hold promise for a wide range of applications. In order to fully explore the potentials of the new CAE system, various radiotherapy plans in other treatment sites using different treatment techniques could be selected for CAE system evaluation.

After accumulating sufficient reliable radiobiological data, robust TCP and NTCP models are expected to play an increasing role in IMRT planning. To give more accurate tumor control prediction using the CI_{DD}, the Gaussian function could be further modified to penalize the effect of cold spot. In the future, it might be worth designing a hybrid index that could combine the CI_{DD} scoring system with these biological factors for comprehensive plan evaluation.

6.5 Conclusion

DICOM RT has become the de facto standard storing the information pertaining to radiotherapy. However, the wealth of data is often underutilized for knowledge discovery. This study demonstrated the potential applications of DICOM RT objects in data mining. Taking advantages of open DICOM RT standard, the CAE system with the CI_{DD} could precisely retrieve relevant data from the DICOM RT objects and derive valuable information to facilitate automatic evaluation of IMRT plans for head-and-neck cancer. As a powerful data mining tool, the CAE system allowed intelligent navigation of harvested data on an independent platform. With prompt problem detection features, the direct relationships between the DVH data to the corresponding dose distribution superimposed on the CT images could be visualized. The CAE system could

improve the planners' efficiency and accuracy in evaluating an IMRT plan and identifying all underdose and overdose regions on each CT slice.

Supporting DICOM standard enabled seamless interoperability, greater flexibility and easy integration in workflow environment. The DICOM-based CAE system with CI_{DD} offered a vendor-neutral platform for retrieval and evaluation of all IMRT plans. Since IMRT plan evaluation process is particularly challenging, tireless attention to every single detail is required. As an extension of existing quality assurance programs, the use of CAE system with CI_{DD} could provide an effective means of benchmarking performance, reducing treatment plan variability and advancing the quality of current IMRT planning.

Recognizing the lack of individualized target conformity index in routine IMRT reporting, the CI_{DD} scoring system that considered spatial importance of each voxel within the PTV was uniquely designed and integrated into the CAE system. By taking individual target volume and shape variability into account, the spatial information related to the locations of cold spot within the PTV was incorporated into the CI_{DD} model. The CI_{DD} scoring system was capable of ranking treatment plans with similar DVHs but different distribution of underdosed regions. Compared with other existing quantitative indices, the tailor-made CI_{DD} scoring system resulted in the largest coefficient of variance, suggesting that its power to differentiate rival plans was the greatest. By considering both the extent and location of dose inhomogeneity on an individual patient basis, the CAE system with CI_{DD} made personalized medicine a reality.

As a simple addition to the CAE system, the CI_{DD} could have important

implications in IMRT plan evaluation. The planners could make a more informed choice of the optimal plan, allowing evaluation of complex IMRT plans more efficient. The evaluation time was significantly reduced using the CAE along with the CI_{DD} for both inexperienced and experienced planners. The CAE system could serve as a useful teaching tool which helps the novice planners to improve their plan evaluation skills and efficiency. Proper education and training on the use of CAE system should have a positive effect on user performance.

In summary, the significance of this thesis are:

1. To demonstrate the feasibility and good applicability of DICOM RT standard in data mining through the successful development of the DICOM-based CAE system with CI_{DD}.
2. To eliminate human errors and automate tedious, time-consuming tasks by developing the CAE system for automatic evaluation of IMRT plans for head-and- neck cancer.
3. To improve plan quality and consistency of practice by designing a personalized CI_{DD} scoring system for quantitative comparison of IMRT plans.

With such promising evaluation results, the DICOM-based CAE system along with the CI_{DD} scoring system could represent a major breakthrough in the routine IMRT planning workflow by eliminating all tedious manual evaluation steps, introducing remote plan evaluation and providing better treatment plan consistency. As an effective quality control measure for evaluation of IMRT plans, the CAE system with CI_{DD} could be adopted in the evaluation of plans other than IMRT.

References

1. Ågren A., Brahme A., and Turesson I., Optimization of uncomplicated control for head and neck tumors. *Int J Radiat Oncol Biol Phys*, 1990, 19(4), 1077-85.

2. Amosson, C.M., Teh, B.S., Van, T.J., Uy, N., Huang, E., Mai, W.Y., Frolov, A., Woo, S.Y., Chiu, J.K., Carpenter, L.S., Lu, H.H., Grant, W.H., 3rd, and Butler, E.B., Dosimetric predictors of xerostomia for head-and-neck cancer patients treated with the smart (simultaneous modulated accelerated radiation therapy) boost technique. *Int J Radiat Oncol Biol Phys*, 2003, 56(1), 136-44.

3. Arbea, L., Ramos, L.I., Martinez-Monge, R., Moreno, M., and Aristu, J., Intensity-modulated radiation therapy (IMRT) vs. 3D conformal radiotherapy (3DCRT) in locally advanced rectal cancer (LARC): dosimetric comparison and clinical implications. *Radiat Oncol*, 2010, 5, 17.

4. Astner, S.T., Shi, K., Vaupel, P., and Molls, M., Imaging of tumor physiology: impacts on clinical radiation oncology. *Exp Oncol*, 2010, 32(3), 149-52.

5. Baltas, D., Kolotas, C., Geramani, K., Mould, R.F., Ioannidis, G., Kekchidi, M., and Zamboglou, N., A conformal index (COIN) to evaluate implant quality and dose specification in brachytherapy. *Int J Radiat Oncol Biol Phys*, 1998, 40(2), 515-24.

6. Bettinardi, V., Picchio, M., Di Muzio, N., Gianolli, L., Gilardi, M.C., and Messa, C., Detection and compensation of organ/lesion motion using 4D-PET/CT respiratory gated acquisition techniques. *Radiother Oncol*, 2010, 96(3), 311-6.

7. Bidgood, W.D., Jr. and Horii, S.C., Introduction to the ACR-NEMA DICOM standard. *Radiographics*, 1992, 12(2), 345-55.

8. Blessing, M., Stsepankou, D., Wertz, H., Arns, A., Lohr, F., Hesser, J., and Wenz, F., Breath-hold target localization with simultaneous kilovoltage/megavoltage cone-beam computed tomography and fast reconstruction. *Int J Radiat Oncol Biol Phys*, 2010, 78(4), 1219-26.

9. Boehm, B., Unifying software engineering and systems engineering. *Computer*, 2000, 33(3), 114-116.

10. Boehm, B.W., A spiral model of software development and enhancement. *Computer*, 1988, 21(5):61-72.

11. Bortfeld, T., Craft, D., Dempsey, J.F., Halabi, T., and Romeijn, H.E., Evaluating target cold spots by the use of tail EUDs. *Int J Radiat Oncol Biol Phys*, 2008, 71(3), 880-9.

12. Bratengeier, K., Meyer, J., Schwab, F., Vordermark, D., and Flentje, M., Steep dose gradients for simultaneous integrated boost IMRT. *Z Med Phys*, 2009, 19(2), 129-35.

13. Breen, S.L. and Zhang, B., Audit of an automated checklist for quality control of radiotherapy treatment plans. *Radiother Oncol*, 2010, 97(3), 579-84.

14. Brenner, R.J., Ulissey, M.J., and Wilt, R.M., Computer-aided detection as evidence in the courtroom: potential implications of an appellate court's ruling. *AJR Am J Roentgenol*, 2006, 186(1), 48-51.

15. Brewster, L., Mohan, R., Mageras, G., Burman, C., Leibel, S., and Fuks, Z., Three dimensional conformal treatment planning with multileaf collimators. *Int J Radiat Oncol Biol Phys*, 1995, 33(5), 1081-9.

16. Broderick, M., Leech, M., and Coffey, M., Direct aperture optimization as a means of reducing the complexity of Intensity Modulated Radiation Therapy plans. *Radiat Oncol*, 2009, 4, 8.

17. Brown, M.S., Shah, S.K., Pais, R.C., Lee, Y.Z., McNitt-Gray, M.F., Goldin, J.G., Cardenas, A.F., and Aberle, D.R., Database design and implementation for quantitative image analysis research. *IEEE Trans Inf Technol Biomed*, 2005, 9(1), 99-108.

18. Bruzzaniti, V., Abate, A., Pedrini, M., Benassi, M., and Strigari, L., IsoBED: a tool for automatic calculation of biologically equivalent fractionation schedules in radiotherapy using IMRT with a simultaneous integrated boost (SIB) technique. *J Exp Clin Cancer Res*, 2011, 30, 52.

19. Bueno, G., Deniz, O., Salido, J., Carrascosa, C., and Delgado, J.M., A geodesic deformable model for automatic segmentation of image sequences applied to radiation therapy. *Int J Comput Assist Radiol Surg*, 2011, 6(3), 341-50.

20. Castadot, P., Geets, X., Lee, J.A., Christian, N., and Gregoire, V., Assessment by a deformable registration method of the volumetric and positional changes of target volumes and organs at risk in pharyngo-laryngeal tumors treated with concomitant chemo-radiation. *Radiother Oncol*, 2010, 95(2), 209-17.

21. Cendales, R., Schiappacasse, L., Schnitman, F., Garcia, G., and Marsiglia, H., Helical tomotherapy in patients with breast cancer and complex treatment volumes. *Clin Transl Oncol*, 2011, 13(4), 268-74.

22. Chao, K.S., Ozyigit, G., Blanco, A.L., Thorstad, W.L., Deasy, J.O., Haughey, B.H., Spector, G.J., and Sessions, D.G., Intensity-modulated radiation therapy for oropharyngeal carcinoma: impact of tumor volume. *Int J Radiat Oncol Biol Phys*, 2004, 59(1), 43-50.

23. Chau, R.M., Teo, P.M., Kam, M.K., Leung, S.F., Cheung, K.Y., and Chan, A.T., Dosimetric comparison between 2-dimensional radiation therapy and intensity modulated radiation therapy in treatment of advanced T-stage nasopharyngeal carcinoma: to treat less or more in the planning organ-at-risk volume of the brainstem and spinal cord. *Med Dosim*, 2007, 32(4), 263-70.

24. Chen, A.M., Cheng, S., Farwell, D.G., Luu, Q., Donald, P.J., Boggan, J., Franklin, S., and Purdy, J.A., Utility of daily image guidance with intensity-modulated radiotherapy for tumors of the base of skull. *Head Neck*, 2011.

25. Chen, A.M., Farwell, D.G., Luu, Q., Donald, P.J., Perks, J., and Purdy, J.A., Evaluation of the planning target volume in the treatment of head and neck cancer with intensity-modulated radiotherapy: what is the appropriate expansion margin in the setting of daily image guidance? *Int J Radiat Oncol Biol Phys*, 2011, 81(4), 943-9.

26. Chen, S.K., Integration of the digital imaging and communications in medicine standard into an oral and maxillofacial image management and communication system. *Oral Surg Oral Med Oral Pathol Oral Radiol Endod*, 2001, 91(2), 235-8.

27. Cheng, C.W. and Das, I.J., Treatment plan evaluation using dose-volume histogram (DVH) and spatial dose-volume histogram (*z*DVH). *Int J Radiat Oncol Biol Phys*, 1999, 43(5), 1143-50.

28. Chernak, E.S., Rodriguez-Antunez, A., Jelden, G.L., Dhaliwal, R.S., and Lavik, P.S., The use of computed tomography for radiation therapy treatment planning. *Radiology*, 1975, 117(3 Pt 1), 613-4.

29. Chiti, A., Kirienko, M., and Gregoire, V., Clinical use of PET-CT data for radiotherapy planning: what are we looking for? *Radiother Oncol*, 2010, 96(3), 277-9.

30. Clunie DA, Carrino JA. DICOM. In: Dreyer KJ, Mehta A, Thrall JH, eds. *PACS: A guide to the digital revolution*. New York, NY: Springer; 2002.

31. Cook, J.T., Tobler, M., Leavitt, D.D., and Watson, G., IMRT fluence map editing to control hot and cold spots. *Med Dosim*, 2005, 30(4), 201-4.

32. Craft, D. and Monz, M., Simultaneous navigation of multiple Pareto surfaces, with an application to multicriteria IMRT planning with multiple beam angle configurations. *Med Phys*, 2010, 37(2), 736-41.

33. Craft, D.L., Hong, T.S., Shih, H.A., and Bortfeld, T.R., Improved planning time and plan quality through multicriteria optimization for intensity-modulated radiotherapy. *Int J Radiat Oncol Biol Phys*, 2012, 82(1), e83-90.

34. Das, I.J., Cheng, C.W., Chopra, K.L., Mitra, R.K., Srivastava, S.P., and Glatstein, E., Intensity-modulated radiation therapy dose prescription, recording, and delivery: patterns of variability among institutions and treatment planning systems. *J Natl Cancer Inst*, 2008, 100(5), 300-7.

35. Das, S., A role for biological optimization within the current treatment planning paradigm. *Med Phys*, 2009, 36(10), 4672-82.

36. de Crevoisier, R., Isambert, A., Lisbona, A., Bodez, V., Marguet, M., Lafay, F., Remonnay, R., and Lagrange, J.L., Image-guided radiotherapy. *Cancer Radiother*, 2007, 11(6-7), 296-304.

37. Deasy, J.O., Comments on the use of the Lyman-Kutcher-Burman model to describe tissue response to nonuniform irradiation. *Int J Radiat Oncol Biol Phys*, 2000, 47(5), 1458-60.

38. Degardin-Capon, N., Bricon-Souf, N., Beuscart-Zephir, M.C., and Beuscart, R., Group decision support system applied to the medical pluri-disciplinary decision group: usability and efficacy. *Stud Health Technol Inform*, 2008, 136, 413-418.

39. Ding, M., Newman, F., Chen, C., Stuhr, K., and Gaspar, L.E., Dosimetric comparison between 3DCRT and IMRT using different multileaf collimators in the treatment of brain tumors. *Med Dosim*, 2009, 34(1), 1-8.

40. Dirscherl, T., Alvarez-Moret, J., and Bogner, L., Advantage of biological over physical optimization in prostate cancer? *Z Med Phys*, 2011, 21(3), 228-35.

41. Doi, K., MacMahon, H., Katsuragawa, S., Nishikawa, R.M., and Jiang, Y., Computer-aided diagnosis in radiology: potential and pitfalls. *Eur J Radiol*, 1999, 31(2), 97-109.

42. Doi, K., Overview on research and development of computer-aided diagnostic schemes. *Semin Ultrasound CT MR*, 2004, 25(5), 404-10.

43. Doi, K., Computer-aided diagnosis in medical imaging: historical review, current status and future potential. *Comput Med Imaging Graph*, 2007, 31(4-5), 198-211.

44. Drzymala, R.E., Mohan, R., Brewster, L., Chu, J., Goitein, M., Harms, W., and Urie, M., Dose-volume histograms. *Int J Radiat Oncol Biol Phys*, 1991, 21(1), 71-8.

45. Duchateau, M., Tournel, K., Verellen, D., Van de Vondel, I., Reynders, T., Linthout, N., Gevaert, T., de Coninck, P., Depuydt, T., and Storme, G., The effect of tomotherapy imaging beam output instabilities on dose calculation. *Phys Med Biol*, 2010, 55(11), N329-36.

46. Ebert, M.A., Haworth, A., Kearvell, R., Hooton, B., Hug, B., Spry, N.A., Bydder, S.A., and Joseph, D.J., Comparison of DVH data from multiple radiotherapy treatment planning systems. *Phys Med Biol*, 2010, 55(11), N337-46.

47. Eitner, S., Holst, S., Wichmann, M., Karl, M., Nkenke, E., and Schlegel, A., Comparative study on interactive computer-aided-learning and computer-aided-testing in patient-based dental training in maxillofacial surgery. *Eur J Dent Educ*, 2008, 12(1), 35-40.

48. Ernst, R.D., Baumgartner, B.R., Tamm, E.P., and Torres, W.E., Development of a teaching file by using a DICOM database. *Radiographics*, 2002, 22(1), 217-21.

49. Farman, A.G., Applying DICOM to dentistry. *J Digit Imaging*, 2005, 18(1), 23-7.

50. Ferlay, J., Shin, H.R., Bray, F., Forman, D., Mathers, C., and Parkin, D.M., Estimates of worldwide burden of cancer in 2008: GLOBOCAN 2008. *Int J Cancer*, 2010, 127(12), 2893-917.

51. Feuvret, L., Noel, G., Mazeron, J.J., and Bey, P., Conformity index: a review. *Int J Radiat Oncol Biol Phys*, 2006, 64(2), 333-42.

52. Foord, K., Year 2000: status of picture archiving and digital imaging in European hospitals. *Eur Radiol*, 2001, 11(3), 513-24.

53. Frommelt, P.C., Whitstone, E.N., and Frommelt, M.A., Experience with a DICOM-compatible digital pediatric echocardiography laboratory. *Pediatr Cardiol*, 2002, 23(1), 53-7.

54. Fuss, M., Salter, B.J., Cheek, D., Sadeghi, A., Hevezi, J.M., and Herman, T.S., Repositioning accuracy of a commercially available thermoplastic mask system. *Radiother Oncol*, 2004, 71(3), 339-45.

55. Gale, M.E. and Gale, D.R., DICOM modality worklist: an essential component in a PACS environment. *J Digit Imaging*, 2000, 13(3), 101-8.

56. Galvin, J.M., Smith, A.R., Moeller, R.D., Goodman, R.L., Powlis, W.D., Rubenstein, J., Solin, L.J., Michael, B., Needham, M., and Huntzinger, C.J., Evaluation of multileaf collimator design for a photon beam. *Int J Radiat Oncol Biol Phys*, 1992, 23(4), 789-801.

57. Gay, H.A., and Niemierko, A., A free program for calculating EUD-based NTCP and TCP in external beam radiotherapy. *Phys Med*, 2007, 23(3), 115-125.

58. Geise, R.A. and McCullough, E.C., The use of CT scanners in megavoltage photon-beam therapy planning. *Radiology*, 1977, 124(1), 133-41.

59. Gendrin, C., Markelj, P., Pawiro, S.A., Spoerk, J., Bloch, C., Weber, C., Figl, M., Bergmann, H., Birkfellner, W., Likar, B., and Pernus, F., Validation for 2D/3D registration. II: The comparison of intensity- and gradient-based merit functions using a new gold standard data set. *Med Phys*, 2011, 38(3), 1491-502.

60. Gentili, A., Chung, C.B., and Hughes, T., Informatics in radiology: use of the MIRC DICOM service for clinical trials to automatically create teaching file cases from PACS. *Radiographics*, 2007, 27(1), 269-75.

61. Gérard, J.P., Thariat, J., Giraud, P., and Cosset, J.M., Past, present and near future of techniques in radiation oncology. *Bull Cancer*, 2010, 97(7),

743-51.

62. Gertych, A., Zhang, A., Sayre, J., Pospiech-Kurkowska, S., and Huang, H.K., Bone age assessment of children using a digital hand atlas. *Comput Med Imaging Graph*, 2007, 31(4-5), 322-31.

63. Goitein, M., Limitations of two-dimensional treatment planning programs. *Med Phys*, 1982, 9(4), 580-6.

64. Gossman, M.S. and Bank, M.I., Dose-volume histogram quality assurance for linac-based treatment planning systems. *J Med Phys*, 2010, 35(4), 197-201.

65. Graf, R., Wust, P., Budach, V., and Boehmer, D., Potentials of on-line repositioning based on implanted fiducial markers and electronic portal imaging in prostate cancer radiotherapy. *Radiat Oncol*, 2009, 4, 13.

66. Graves, E.E., Quon, A., and Loo, B.W., Jr., RT_Image: an open-source tool for investigating PET in radiation oncology. *Technol Cancer Res Treat*, 2007, 6(2), 111-21.

67. Hanin, L.G., Iterated birth and death process as a model of radiation cell survival. *Math Biosci*, 2001, 169(1), 89-107.

68. Hartmann, M. and Bogner, L., Investigation of intensity-modulated radiotherapy optimization with gEUD-based objectives by means of simulated annealing. *Med Phys*, 2008, 35(5), 2041-9.

69. Hauser, D.L., Wessinger, S.J., Condon, R.T., Golladay, G.J., Hoeffel, D.P., Gillis, D.J., Merrill, D.R., Chaisson, D., Freiberg, A.A., Estok, D.M., Rubash, H.E., Malchau, H., and Harris, W.H., An electronic database for outcome studies that includes digital radiographs. *J Arthroplasty*, 2001, 16(8 Suppl 1), 71-5.

70. Henríquez, F.C. and Castrillon, S.V., A novel method for the evaluation of uncertainty in dose-volume histogram computation. *Int J Radiat Oncol Biol Phys*, 2008, 70(4), 1263-71.

71. Hong, T.S., Craft, D.L., Carlsson, F., and Bortfeld, T.R., Multicriteria optimization in intensity-modulated radiation therapy treatment planning for locally advanced cancer of the pancreatic head. *Int J Radiat Oncol Biol Phys*, 2008, 72(4), 1208-14.

72. Hsiao, C.H., Hsu, T.C., Chang, J.N., Yang, S.J., Young, S.T., and Chu, W.C., Developing a medical image content repository for e-learning. *J Digit Imaging*, 2006, 19(3), 207-15.

73. Hsiao, C.H., Kao, T., Fang, Y.H., Wang, J.K., Guo, W.Y., Chao, L.H., and Yen, S.H., System integration and DICOM image creation for PET-MR fusion. *J Digit Imaging*, 2005, 18(1), 28-36.

74. Huang, H.K., Industrial Standards (HL7 and DICOM) and Intergrating the Healthcare Enterprise (IHE). In: *PACS and Imaging Informatics: Basic Principles and Applications*, 2nd ed. Wiley-Blackwell, USA, 2010.

75. Huang, H.K., Mankovich, N.J., Taira, R.K., Cho, P.S., Stewart, B.K., Ho, B.K., Chan, K.K., and Ishimitsu, Y., Picture archiving and communication systems (PACS) for radiological images: state of the art. *Crit Rev Diagn Imaging*, 1988, 28(4), 383-427.

76. Huang, Y., Joiner, M., Zhao, B., Liao, Y., and Burmeister, J., Dose convolution filter: incorporating spatial dose information into tissue response modeling. *Med Phys*, 2010, 37(3), 1068-74.

77. International Commission on Radiation Units and Measurement (ICRU), ICRU Report No. 50. Prescribing, recording and reporting photon beam therapy. Washington, DC: ICRU, 1993.

78. International Commission on Radiation Units and Measurement (ICRU), ICRU Report No. 62. Prescribing, recording and reporting photon beam therapy. Washington, DC: ICRU, 1999.

79. International Commission on Radiation Units and Measurement (ICRU), ICRU Report No. 83. Prescribing, recording and reporting photon beam therapy. Washington, DC: ICRU, 2010.

80. Jacobs, C., Sanchez, C.I., Saur, S.C., Twellmann, T., de Jong, P.A., and van Ginneken, B., Computer-aided detection of ground glass nodules in thoracic CT images using shape, intensity and context features. *Med Image Comput Comput Assist Interv*, 2011, 14(Pt 3), 207-14.

81. Jaganathan, A., Tiwari, M., Phansekar, R., Panta, R., and Huilgol, N., Intensity-modulated radiation to spare neural stem cells in brain tumors: a computational platform for evaluation of physical and biological dose metrics. *J Cancer Res Ther*, 2011, 7(1), 58-63.

82. Jemal, A., Bray, F., Center, M.M., Ferlay, J., Ward, E., and Forman, D., Global cancer statistics. *CA Cancer J Clin*, 2011, 61(2), 69-90.

83. Johnston, H., Hilts, M., Beckham, W., and Berthelet, E., 3D ultrasound for prostate localization in radiation therapy: a comparison with implanted fiducial markers. *Med Phys*, 2008, 35(6), 2403-13.

84. Jonsson, J.H., Brynolfsson, P., Garpebring, A., Karlsson, M., Soderstrom, K., and Nyholm, T., Registration accuracy for MR images of the prostate using a subvolume based registration protocol. *Radiat Oncol*, 2011, 6, 73.

85. Kabachinski, J., DICOM: key concepts – part I. *Biomed Instrum Technol*, 2005, 39(3), 214-6.

86. Kamauu, A.W., DuVall, S.L., Robison, R.J., Liimatta, A.P., Wiggins, R.H., 3rd, and Avrin, D.E., Informatics in radiology (infoRAD): Vendor-neutral

case input into a server-based digital teaching file system. *Radiographics*, 2006, 26(6), 1877-85.

87. Kao, C.H., Hsieh, T.C., Yu, C.Y., Yen, K.Y., Yang, S.N., Wang, Y.C., Liang, J.A., Chien, C.R., and Chen, S.W., 18F-FDG PET/CT-based gross tumor volume definition for radiotherapy in head and neck cancer: a correlation study between suitable uptake value threshold and tumor parameters. *Radiat Oncol*, 2010, 5, 76.

88. Kahn, C.E., Jr., Carrino, J.A., Flynn, M.J., Peck, D.J., and Horii, S.C., DICOM and radiology: past, present, and future. *J Am Coll Radiol*, 2007, 4(9), 652-7.

89. Kessler, M.L., Ten Haken, R.K., Fraass, B.A., and McShan, D.L., Expanding the use and effectiveness of dose-volume histograms for 3-D treatment planning. I: Integration of 3-D dose-display. *Int J Radiat Oncol Biol Phys*, 1994, 29(5), 1125-31.

90. Kelley, K., Sample size planning for the coefficient of variation from the accuracy in parameter estimation approach. *Behav Res Methods*, 2007, 39(4), 755-766.

91. Kim, Y. and Tomé, W.A., Dose-painting IMRT optimization using biological parameters. *Acta Oncol*, 2010, 49(8), 1374-84.

92. Kjaer-Kristoffersen, F., Ohlhues, L., Medin, J., and Korreman, S., RapidArc volumetric modulated therapy planning for prostate cancer patients. *Acta Oncol*, 2009, 48(2), 227-32.

93. Knöös, T., Kristensen, I., and Nilsson, P., Volumetric and dosimetric evaluation of radiation treatment plans: radiation conformity index. *Int J Radiat Oncol Biol Phys*, 1998, 42(5), 1169-76.

94. Koutkias, V., Kilintzis, V., Stalidis, G., Lazou, K., Collyda, C., Chazard, E., McNair, P., Beuscart, R., and Maglaveras, N., Constructing Clinical Decision Support Systems for Adverse Drug Event Prevention: A Knowledge-based Approach. *AMIA Annu Symp Proc*, 2010, 2010, 402-6.

95. Kuo, H.C., Mah, D., Chuang, K.S., Wu, A., Hong, L., Yaparpalvi, R., Spierer, M., and Kalnicki, S., A method incorporating 4DCT data for evaluating the dosimetric effects of respiratory motion in single-arc IMAT. *Phys Med Biol*, 2010, 55(12), 3479-97.

96. Kupelian, P. and Langen, K., Helical tomotherapy: image-guided and adaptive radiotherapy. *Front Radiat Ther Oncol*, 2011, 43, 165-80.

97. Kutcher, G.J. and Burman, C., Calculation of complication probability factors for non-uniform normal tissue irradiation: the effective volume method. *Int J Radiat Oncol Biol Phys*, 1989, 16(6), 1623-30.

98. Kuzmak, P.M. and Dayhoff, R.E., The use of digital imaging and communications in medicine (DICOM) in the integration of imaging into the electronic patient record at the Department of Veterans Affairs. *J Digit Imaging*, 2000, 13(2 Suppl 1), 133-7.

99. Langen, K.M., Meeks, S.L., Poole, D.O., Wagner, T.H., Willoughby, T.R., Kupelian, P.A., Ruchala, K.J., Haimerl, J., and Olivera, G.H., The use of megavoltage CT (MVCT) images for dose recomputations. *Phys Med Biol*, 2005, 50(18), 4259-76.

100. Langer, S.G., A Flexible Database Architecture for Mining DICOM Objects: the DICOM Data Warehouse. *J Digit Imaging*, 2011.

101. Law, M.Y., A model of DICOM-based electronic patient record in radiation therapy. *Comput Med Imaging Graph*, 2005, 29(2-3), 125-36.

102. Law, M.Y. and Huang, H.K., Concept of a PACS and imaging informatics-based server for radiation therapy. *Comput Med Imaging Graph*, 2003, 27(1), 1-9.

103. Law, M.Y. and Liu, B., Informatics in radiology: DICOM-RT and its utilization in radiation therapy. *Radiographics*, 2009, 29(3), 655-67.

104. Law, M.Y., Liu, B., and Chan, L.W., Informatics in radiology: DICOM-RT-based electronic patient record information system for radiation therapy. *Radiographics*, 2009, 29(4), 961-72.

105. Le, A.H., Liu, B., Schulte, R., and Huang, H.K., Intelligent ePR system for evidence-based research in radiotherapy: proton therapy for prostate cancer. *Int J Comput Assist Radiol Surg*, 2011, 6(6), 769-84.

106. Lee, K.W., Wu, J.K., Jeng, S.C., Hsueh Liu, Y.W., and Cheng, J.C., Skin dose impact from vacuum immobilization device and carbon fiber couch in intensity modulated radiation therapy for prostate cancer. *Med Dosim*, 2009, 34(3), 228-32.

107. Lee, T.F., Ting, H.M., Chao, P.J., and Fang, F.M., Dual Arc Volumetric-modulated Arc Radiotherapy (VMAT) of Nasopharyngeal Carcinomas: A Simultaneous Integrated Boost Treatment Plan Comparison with Intensity-modulated Radiotherapies and Single Arc VMAT. *Clin Oncol (R Coll Radiol)*, 2011.

108. Lee, W.J., Yang, C.Y., Liu, K.L., Liu, H.M., Ching, Y.T., and Chen, S.J., Establishing a Web-based DICOM teaching file authoring tool using open-source public software. *J Digit Imaging*, 2005, 18(3), 169-75.

109. Lee, Y., Chae, Y., and Jeon, S., Integration and Evaluation of Clinical Decision Support Systems for Diagnosis Idopathics Pulmonary Fibrosis (IPF). *Healthc Inform Res*, 2010, 16(4), 260-72.

110. Lefkopoulos, D., Grandjean, P., and Platoni, K., Progress in optimizing dosimetry plans in stereotactic radiotherapy in the Salt Group (Saint-Anne-Lariboisiere-Tenon). *Cancer Radiother*, 1998, 2(2), 127-38.

111. Lei, J. and Li, Y., An approaching genetic algorithm for automatic beam angle selection in IMRT planning. *Comput Methods Programs Biomed*, 2009, 93(3), 257-65.

112. Leong, T., Everitt, C., Yuen, K., Condron, S., Hui, A., Ngan, S.Y., Pitman, A., Lau, E.W., MacManus, M., Binns, D., Ackerly, T., and Hicks, R.J., A prospective study to evaluate the impact of FDG-PET on CT-based radiotherapy treatment planning for oesophageal cancer. *Radiother Oncol*, 2006, 78(3), 254-61.

113. Leung, L.H., Kan, M.W., Cheng, A.C., Wong, W.K., and Yau, C.C., A new dose-volume-based Plan Quality Index for IMRT plan comparison. *Radiother Oncol*, 2007, 85(3), 407-17.

114. Levman, J.E. and Martel, A.L., A margin sharpness measurement for the diagnosis of breast cancer from magnetic resonance imaging examinations. *Acad Radiol*, 2011, 18(12), 1577-81.

115. Li, F., Engelmann, R., Doi, K., and Macmahon, H., True detection versus "accidental" detection of small lung cancer by a computer-aided detection (CAD) program on chest radiographs. *J Digit Imaging*, 2010, 23(1), 66-72.

116. Li, F., Engelmann, R., Metz, C.E., Doi, K., and MacMahon, H., Lung cancers missed on chest radiographs: results obtained with a commercial computer-aided detection program. *Radiology*, 2008, 246(1), 273-80.

117. Li, L., Zheng, Y., Zhang, L., and Clark, R.A., False-positive reduction in CAD mass detection using a competitive classification strategy. *Med Phys*, 2001, 28(2), 250-8.

118. Liang, Y., Xu, H., Yao, J., Li, Z., and Chen, W., Four-dimensional intensity-modulated radiotherapy planning for dynamic multileaf collimator tracking radiotherapy. *Int J Radiat Oncol Biol Phys*, 2009, 74(1), 266-74.

119. Lim, C.C., Yang, G.L., Nowinski, W.L., and Hui, F., Medical Image Resource Center – making electronic teaching files from PACS. *J Digit Imaging*, 2003, 16(4), 331-6.

120. Liu, B.J., A knowledge-based imaging informatics approach for managing proton beam therapy of cancer patients. *Technol Cancer Res Treat*, 2007, 6(4 Suppl), 77-84.

121. Loane, M. and Wootton, R., A review of guidelines and standards for telemedicine. *J Telemed Telecare*, 2002, 8(2), 63-71.

122. Locke, C. and Zavgorodni, S., Vega library for processing DICOM data required in Monte Carlo verification of radiotherapy treatment plans. *Australas Phys Eng Sci Med*, 2008, 31(4), 290-9.

123. Lomax, N.J. and Scheib, S.G., Quantifying the degree of conformity in radiosurgery treatment planning. *Int J Radiat Oncol Biol Phys*, 2003, 55(5), 1409-19.

124. Luan, S., Wang, C., Chen, D.Z., Hu, X.S., Naqvi, S.A., Yu, C.X., and Lee, C.L., A new MLC segmentation algorithm/software for step-and-shoot IMRT delivery. *Med Phys*, 2004, 31(4), 695-707.

125. Lyman, J.T., Complication probability as assessed from dose-volume histograms. *Radiat Res Suppl*, 1985, 8, S13-9.

126. Mackie, T.R., History of tomotherapy. *Phys Med Biol*, 2006, 51(13), R427-53.

127. Majewski, W., Wesolowska, I., Urbanczyk, H., Hawrylewicz, L., Schwierczok, B., and Miszczyk, L., Dose distribution in bladder and surrounding normal tissues in relation to bladder volume in conformal radiotherapy for bladder cancer. *Int J Radiat Oncol Biol Phys*, 2009, 75(5), 1371-8.

128. Manens, J.P., Exchange of medical imaging and data information in radiotherapy: needs, methods and current limits. *Cancer Radiother*, 1997, 1(5), 524-31.

129. Mao, W., Hsu, A., Riaz, N., Lee, L., Wiersma, R., Luxton, G., King, C., Xing, L., and Solberg, T., Image-guided radiotherapy in near real time with intensity-modulated radiotherapy megavoltage treatment beam imaging. *Int J Radiat Oncol Biol Phys*, 2009, 75(2), 603-10.

130. Margalit, D.N., Chen, Y.H., Catalano, P.J., Heckman, K., Vivenzio, T., Nissen, K., Wolfsberger, L.D., Cormack, R.A., Mauch, P., and Ng, A.K., Technological advancements and error rates in radiation therapy delivery. *Int J Radiat Oncol Biol Phys*, 2011, 81(4), e673-9.

131. McClelland, J.R., Hughes, S., Modat, M., Qureshi, A., Ahmad, S., Landau, D.B., Ourselin, S., and Hawkes, D.J., Inter-fraction variations in respiratory motion models. *Phys Med Biol*, 2011, 56(1), 251-72.

132. McGarry, C.K., Chinneck, C.D., O'Toole, M.M., O'Sullivan, J.M., Prise, K.M., and Hounsell, A.R., Assessing software upgrades, plan properties and patient geometry using intensity modulated radiation therapy (IMRT) complexity metrics. *Med Phys*, 2011, 38(4), 2027-34.

133. McNair, H.A., Adams, E.J., Clark, C.H., Miles, E.A., and Nutting, C.M., Implementation of IMRT in the radiotherapy department. *Br J Radiol*, 2003, 76(912), 850-6.

134. Men, C., Romeijn, H.E., Taskin, Z.C., and Dempsey, J.F., An exact approach to direct aperture optimization in IMRT treatment planning. *Phys Med Biol*, 2007, 52(24), 7333-52.

135. Menhel, J., Levin, D., Alezra, D., Symon, Z., and Pfeffer, R., Assessing the quality of conformal treatment planning: a new tool for quantitative comparison. *Phys Med Biol*, 2006, 51(20), 5363-75.

136. Miften, M.M., Das, S.K., Su, M., and Marks, L.B., A dose-volume-based tool for evaluating and ranking IMRT treatment plans. *J Appl Clin Med Phys*, 2004, 5(4), 1-14.

137. Mildenberger, P., Eichelberg, M., and Martin, E., Introduction to the DICOM standard. *Eur Radiol*, 2002, 12(4), 920-7.

138. Miles, E.A., Clark, C.H., Urbano, M.T., Bidmead, M., Dearnaley, D.P., Harrington, K.J., A'Hern, R., and Nutting, C.M., The impact of introducing intensity modulated radiotherapy into routine clinical practice. *Radiother Oncol*, 2005, 77(3), 241-6.

139. Milette, M.P. and Otto, K., Maximizing the potential of direct aperture optimization through collimator rotation. *Med Phys*, 2007, 34(4), 1431-8.

140. Mongkolwat, P., Bhalodia, P., Gehl, J.A., and Channin, D.S., Validating DICOM content in a remote storage model. *J Digit Imaging*, 2005, 18(1), 37-41.

141. Montejo, M.E., Shrieve, D.C., Bentz, B.G., Hunt, J.P., Buchman, L.O., Agarwal, N., and Hitchcock, Y.J., IMRT With Simultaneous Integrated Boost and Concurrent Chemotherapy for Locoregionally Advanced Squamous Cell Carcinoma of the Head and Neck. *Int J Radiat Oncol Biol Phys*, 2011, 81(5), e845-52.

142. Muller, H., Michoux, N., Bandon, D., and Geissbuhler, A., A review of content-based image retrieval systems in medical applications-clinical benefits and future directions. *Int J Med Inform*, 2004, 73(1), 1-23.

143. Murthy, V., Master, Z., Adurkar, P., Mallick, I., Mahantshetty, U., Bakshi, G., Tongaonkar, H., and Shrivastava, S., 'Plan of the day' adaptive radiotherapy for bladder cancer using helical tomotherapy. *Radiother Oncol*, 2011, 99(1), 55-60.

144. Mutaf, Y.D., Scicutella, C.J., Michalski, D., Fallon, K., Brandner, E.D., Bednarz, G., and Huq, M.S., A simulation study of irregular respiratory motion and its dosimetric impact on lung tumors. *Phys Med Biol*, 2011, 56(3), 845-59.

145. Nakayama, R., Watanabe, R., Namba, K., Takeda, K., Yamamoto, K., Katsuragawa, S., and Doi, K., An improved computer-aided diagnosis scheme using the nearest neighbor criterion for determining histological classification of clustered microcalcifications. *Methods Inf Med*, 2007, 46(6), 716-22.

146. Narasingarao, M.R., Manda, R., Sridhar, G.R., Madhu, K., and Rao, A.A., A clinical decision support system using multilayer perceptron neural network to assess well being in diabetes. *J Assoc Physicians India*, 2009, 57, 127-33.

147. Nelson, C., Balter, P., Morice, R.C., Bucci, K., Dong, L., Tucker, S., Vedam, S., Chang, J.Y., and Starkschall, G., Evaluation of tumor position and PTV margins using image guidance and respiratory gating. *Int J Radiat Oncol Biol Phys*, 2010, 76(5), 1578-85.

148. Nelson, C., Balter, P., Morice, R.C., Choi, B., Kudchadker, R.J., Bucci, K., Chang, J.Y., Dong, L., Tucker, S., Vedam, S., Briere, T., and Starkschall, G., A technique for reducing patient setup uncertainties by aligning and verifying daily positioning of a moving tumor using implanted fiducials. *J Appl Clin Med Phys*, 2008, 9(4), 2766.

149. Neumann, M., DICOM – current status and future developments for radiotherapy. *Z Med Phys*, 2002, 12(3), 171-6.

150. Ng, W.T., Lee, M.C., Hung, W.M., Choi, C.W., Lee, K.C., Chan, O.S., and Lee, A.W., Clinical outcomes and patterns of failure after intensity-modulated radiotherapy for nasopharyngeal carcinoma. *Int J Radiat Oncol Biol Phys*, 2011, 79(2), 420-8.

151. Nicolini, G., Fogliata, A., and Cozzi, L., IMRT with the sliding window: comparison of the static and dynamic methods. Dosimetric and spectral analysis. *Radiother Oncol*, 2005, 75(1), 112-9.

152. Niemierko, A., Reporting and analyzing dose distributions: a concept of equivalent uniform dose. *Med Phys*, 1997, 24(1), 103-10.

153. Oliver, M., Gagne, I., Bush, K., Zavgorodni, S., Ansbacher, W., and Beckham, W., Clinical significance of multi-leaf collimator positional errors for volumetric modulated arc therapy. *Radiother Oncol*, 2010, 97(3), 554-60.

154. Olson, A.C., Wegner, R.E., Scicutella, C., Heron, D.E., Greenberger, J.S., Huq, M.S., Bednarz, G., and Flickinger, J.C., Quality assurance analysis of a large multicenter practice: does increased complexity of intensity-modulated radiotherapy lead to increased error frequency? *Int J Radiat Oncol Biol Phys*, 2012, 82(1), e77-82.

155. Ozyigit, G., Cengiz, M., Yazici, G., Yildiz, F., Gurkaynak, M., Zorlu, F., Yildiz, D., Hosal, S., Gullu, I., and Akyol, F., A retrospective comparison of robotic stereotactic body radiotherapy and three-dimensional conformal radiotherapy for the reirradiation of locally recurrent nasopharyngeal carcinoma. *Int J Radiat Oncol Biol Phys*, 2011, 81(4), e263-8.

156. Ozyigit, G., Yang, T., and Chao, K.S., Intensity-modulated radiation therapy for head and neck cancer. *Curr Treat Options Oncol*, 2004, 5(1), 3-9.

157. Paddick, I., A simple scoring ratio to index the conformity of radiosurgical treatment plans. Technical note. *J Neurosurg*, 2000, 93 Suppl 3, 219-22.

158. Palma, D., Vollans, E., James, K., Nakano, S., Moiseenko, V., Shaffer, R., McKenzie, M., Morris, J., and Otto, K., Volumetric modulated arc therapy for delivery of prostate radiotherapy: comparison with intensity-modulated radiotherapy and three-dimensional conformal radiotherapy. *Int J Radiat Oncol Biol Phys*, 2008, 72(4), 996-1001.

159. Papamichail, K.N. and French, S., Decision support in nuclear emergencies. *J Hazard Mater*, 2000, 71(1-3), 321-42.

160. Park, Y., Kitahara, T., Takagi, R., and Kato, R., Current status of therapy for breast cancer worldwide and in Japan. *World J Clin Oncol*, 2011, 2(2), 125-34.

161. Partridge, M., Yamamoto, T., Grau, C., Hoyer, M., and Muren, L.P., Imaging of normal lung, liver and parotid gland function for radiotherapy. *Acta Oncol*, 2010, 49(7), 997-1011.

162. Pawlicki, T. and Mundt, A.J., Quality in radiation oncology. *Med Phys*, 2007, 34(5), 1529-34.

163. Pietka, E., Pospiech-Kurkowska, S.,Gertych, A., and Cao, F., Integration of computer assisted bone age assessment with clinical PACS. *Comput Med Imaging Graph*, 2003, 27(2), 217-228.

164. Pirzkall, A., Carol, M., Lohr, F., Hoss, A., Wannenmacher, M., and Debus, J., Comparison of intensity-modulated radiotherapy with conventional conformal radiotherapy for complex-shaped tumors. *Int J Radiat Oncol Biol Phys*, 2000, 48(5), 1371-80.

165. Prior, F.W., Specifying DICOM compliance for modality interfaces. *Radiographics*, 1993, 13(6), 1381-8.

166. Purdy, J.A., Current ICRU definitions of volumes: limitations and future directions. *Semin Radiat Oncol*, 2004, 14(1), 27-40.

167. Pyakuryal, A., Myint, W.K., Gopalakrishnan, M., Jang, S., Logemann, J.A., and Mittal, B.B., A computational tool for the efficient analysis of dose-volume histograms from radiation therapy treatment plans. *J Appl Clin Med Phys*, 2010, 11(1), 3013.

168. Qi, X.S., Semenenko, V.A., and Li, X.A., Improved critical structure sparing with biologically based IMRT optimization. *Med Phys*, 2009, 36(5), 1790-9.

169. Rao, M., Yang, W., Chen, F., Sheng, K., Ye, J., Mehta, V., Shepard, D., and Cao, D., Comparison of Elekta VMAT with helical tomotherapy and fixed field IMRT: plan quality, delivery efficiency and accuracy. *Med Phys*, 2010, 37(3), 1350-9.

170. Reddy, N.M., Nori, D., Sartin, W., Maiorano, S., Modena, J., Mazur, A., Osian, A., Sood, B., Ravi, A., Sampath, S., and Lange, C.S., Influence of volumes of prostate, rectum, and bladder on treatment planning CT on interfraction prostate shifts during ultrasound image-guided IMRT. *Med Phys*, 2009, 36(12), 5604-11.

171. Riddle, W.R. and Pickens, D.R., Extracting data from a DICOM file. *Med Phys*, 2005, 32(6), 1537-41.

172. Roberson, G.H. and Shieh, Y.Y., Radiology information systems, picture archiving and communication systems, teleradiology – overview and design criteria. *J Digit Imaging*, 1998, 11(4 Suppl 2), 2-7.

173. Romero, C., Almenar, A., Pinto, J.M., Varela, C., Munoz, E., and Botella, M., Impact on breast cancer diagnosis in a multidisciplinary unit after the incorporation of mammography digitalization and computer-aided detection systems. *AJR Am J Roentgenol*, 2011, 197(6), 1492-7.

174. Rong, Y. and Welsh, J.S., Dosimetric and clinical review of helical tomotherapy. *Expert Rev Anticancer Ther*, 2011, 11(2), 309-20.

175. Rosset, A., Ratib, O., Geissbuhler, A., and Vallee, J.P., Integration of a multimedia teaching and reference database in a PACS environment. *Radiographics*, 2002, 22(6), 1567-77.

176. Rotondo, R.L., Sultanem, K., Lavoie, I., Skelly, J., and Raymond, L., Comparison of repositioning accuracy of two commercially available immobilization systems for treatment of head-and-neck tumors using simulation computed tomography imaging. *Int J Radiat Oncol Biol Phys*, 2008, 70(5), 1389-96.

177. Salari, E., Men, C., and Romeijn, H.E., Accounting for the tongue-and-groove effect using a robust direct aperture optimization approach. *Med Phys*, 2011, 38(3), 1266-79.

178. Samuelsson, A. and Johansson, K.A., Intensity modulated radiotherapy treatment planning for dynamic multileaf collimator delivery: influence of different parameters on dose distributions. *Radiother Oncol*, 2003, 66(1), 19-28.

179. Sanchez-Nieto, B. and Nahum, A.E., BIOPLAN: software for the biological evaluation of. Radiotherapy treatment plans. *Med Dosim*, 2000, 25(2), 71-6.

180. Sandwell, D.T., Biharmonic spline interpolation of GEOS-3 and SEASAT altimeter data. *Geophys. Res. Lett*, 1987, 14, 139-142.

181. Saw, C.B., Yakoob, R., Enke, C.A., Lau, T.P., and Ayyangar, K.M., Immobilization devices for intensity-modulated radiation therapy (IMRT). *Med Dosim*, 2001, 26(1), 71-7.

182. Seco, J., Evans, P.M., and Webb, S., Analysis of the effects of the delivery technique on an IMRT plan: comparison for multiple static field, dynamic and NOMOS MIMiC collimation. *Phys Med Biol*, 2001, 46(12), 3073-87.

183. Semenenko, V.A., Reitz, B., Day, E., Qi, X.S., Miften, M., and Li, X.A., Evaluation of a commercial biologically based IMRT treatment planning system. *Med Phys*, 2008, 35(12), 5851-60.

184. Sheng, K., Jeraj, R., Shaw, R., Mackie, T.R., and Paliwal, B.R., Imaging dose management using multi-resolution in CT-guided radiation therapy. *Phys Med Biol*, 2005, 50(6), 1205-19.

185. Shepard, D.M. and Cao, D., Clinical implementation of intensity-modulated arc therapy. *Front Radiat Ther Oncol*, 2011, 43, 80-98.

186. Shiraishi, J., Li, Q., Appelbaum, D., and Doi, K., Computer-aided diagnosis and artificial intelligence in clinical imaging. *Semin Nucl Med*, 2011, 41(6), 449-62.

187. Shiraishi, J., Sugimoto, K., Moriyasu, F., Kamiyama, N., and Doi, K., Computer-aided diagnosis for the classification of focal liver lesions by use of contrast-enhanced ultrasonography. *Med Phys*, 2008, 35(5), 1734-46.

188. Skrzyński, W., Zielińska-Dabrowska, S., Wachowicz, M., Slusarczyk-Kacprzyk, W., Kukolowicz, P.F., and Bulski, W., Computed tomography as a source of electron density information for radiation treatment planning. *Strahlenther Onkol*, 2010, 186(6), 327-33.

189. Smeenk, R.J., Teh, B.S., Butler, E.B., van Lin, E.N., and Kaanders, J.H., Is there a role for endorectal balloons in prostate radiotherapy? A systematic review. *Radiother Oncol*, 2010, 95(3), 277-82.

190. Sontag, M.R. and Cunningham, J.R., Clinical application of a CT based treatment planning system. *Comput Tomogr*, 1978, 2(2), 117-30.

191. Speight, R., Sykes, J., Lindsay, R., Franks, K., and Thwaites, D., The evaluation of a deformable image registration segmentation technique for semi-automating internal target volume (ITV) production from 4DCT images of lung stereotactic body radiotherapy (SBRT) patients. *Radiother Oncol*, 2011, 98(2), 277-83.

192. Spezi, E., Lewis, D.G., and Smith, C.W., A DICOM-RT-based toolbox for the evaluation and verification of radiotherapy plans. *Phys Med Biol*, 2002, 47(23), 4223-32.

193. Stewart, B.K., Kanal, K.M., Perdue, J.R., and Mann, F.A., Computed radiography dose data mining and surveillance as an ongoing quality assurance improvement process. *AJR Am J Roentgenol*, 2007, 189(1), 7-11.

194. Sung, Y.S., Kwon, H.J., Park, B.W., Cho, G., Lee, C.K., Cho, K.S., and Kim, J.K., Prostate cancer detection on dynamic contrast-enhanced MRI: computer-aided diagnosis versus single perfusion parameter maps. *AJR Am J Roentgenol*, 2011, 197(5), 1122-9.

195. Tacke, M.B., Nill, S., Krauss, A., and Oelfke, U., Real-time tumor tracking: automatic compensation of target motion using the Siemens 160 MLC. *Med Phys*, 2010, 37(2), 753-61.

196. Tang, F.H. and Law, Y.Y., A scalable automatic bone age assessment system using the cloud computing technology for integration with PACS. *18th Asian Australasian Congress of Radiological Technologists,* 26-27 Mar, 2011.

197. Tanyi, J.A., He, T., Summers, P.A., Mburu, R.G., Kato, C.M., Rhodes, S.M., Hung, A.Y., and Fuss, M., Assessment of planning target volume margins for intensity-modulated radiotherapy of the prostate gland: role of daily inter- and intrafraction motion. *Int J Radiat Oncol Biol Phys*, 2010, 78(5), 1579-85.

198. Teicher, B.A. and Chari, R.V., Antibody conjugate therapeutics: challenges and potential. *Clin Cancer Res*, 2011, 17(20), 6389-97.

199. Thoeny, H.C., Diffusion-weighted MRI in head and neck radiology: applications in oncology. *Cancer Imaging*, 2011, 10(1), 209-14.

200. Tomé, W.A. and Fowler, J.F., On cold spots in tumor subvolumes. *Med Phys*, 2002, 29(7), 1590-8.

201. Tu, X., LaVallee, T., and Lechleider, R., CD22 as a target for cancer therapy. *J Exp Ther Oncol*, 2011, 9(3), 241-8.

202. Tucker, S.L., Thames, H.D., and Taylor, J.M., How well is the probability of tumor cure after fractionated irradiation described by Poisson statistics? *Radiat Res*, 1990, 124(3), 273-82.

203. Tuikkala, J., Elo, L.L., Nevalainen, O.S., and Aittokallio, T., Missing value imputation improves clustering and interpretation of gene expression microarray data. *BMC Bioinformatics*, 2008, 18(9), 202.

204. Tyng, C.J., Chojniak, R., Pinto, P.N., Borba, M.A., Bitencourt, A.G., Fogaroli, R.C., Castro, D.G., and Novaes, P.E., Conformal radiotherapy for lung cancer: interobservers' variability in the definition of gross tumor volume between radiologists and radiotherapists. *Radiat Oncol*, 2009, 4, 28.

205. Tzikas, A., Karaiskos, P., Papanikolaou, N., Sandilos, P., Koutsouveli, E., Lavdas, E., Scarleas, C., Dardoufas, K., Lind, B.K., and Mavroidis, P., Investigating the clinical aspects of using CT vs. CT-MRI images during organ delineation and treatment planning in prostate cancer radiotherapy. *Technol Cancer Res Treat*, 2011, 10(3), 231-42.

206. Van Belle, V., Pelckmans, K., Van Huffel, S., and Suykens, J.A., Support vector methods for survival analysis: a comparison between ranking and regression approaches. *Artif Intell Med*, 2011, 53(2), 107-18.

207. Van't Riet, A., Mak, A.C., Moerland, M.A., Elders, L.H., and van der Zee, W., A conformation number to quantify the degree of conformality in brachytherapy and external beam irradiation: application to the prostate. *Int J Radiat Oncol Biol Phys*, 1997, 37(3), 731-6.

208. Velec, M., Waldron, J.N., O'Sullivan, B., Bayley, A., Cummings, B., Kim, J.J., Ringash, J., Breen, S.L., Lockwood, G.A., and Dawson, L.A., Cone-beam CT assessment of interfraction and intrafraction setup error of two head-and-neck cancer thermoplastic masks. *Int J Radiat Oncol Biol Phys*, 2010, 76(3), 949-55.

209. Verbakel, W.F., Cuijpers, J.P., Hoffmans, D., Bieker, M., Slotman, B.J., and Senan, S., Volumetric intensity-modulated arc therapy vs. conventional IMRT in head-and-neck cancer: a comparative planning and dosimetric study. *Int J Radiat Oncol Biol Phys*, 2009, 74(1), 252-9.

210. Vieillot, S., Azria, D., Lemanski, C., Moscardo, C.L., Gourgou, S., Dubois, J.B., Ailleres, N., and Fenoglietto, P., Plan comparison of volumetric-modulated arc therapy (RapidArc) and conventional intensity-modulated radiation therapy (IMRT) in anal canal cancer. *Radiat Oncol*, 2010, 5, 92.

211. Vieira, S.C., Dirkx, M.L., Pasma, K.L., and Heijmen, B.J., Dosimetric verification of x-ray fields with steep dose gradients using an electronic portal imaging device. *Phys Med Biol*, 2003, 48(2), 157-66.

212. Wang, H., Garden, A.S., Zhang, L., Wei, X., Ahamad, A., Kuban, D.A., Komaki, R., O'Daniel, J., Zhang, Y., Mohan, R., and Dong, L., Performance evaluation of automatic anatomy segmentation algorithm on repeat or four-dimensional computed tomography images using deformable image registration method. *Int J Radiat Oncol Biol Phys*, 2008, 72(1), 210-9.

213. Wang, S., Pavlicek, W., Roberts, C.C., Langer, S.G., Zhang, M., Hu, M., Morin, R.L., Schueler, B.A., Wellnitz, C.V., and Wu, T., An automated DICOM database capable of arbitrary data mining (including radiation dose indicators) for quality monitoring. *J Digit Imaging*, 2011, 24(2), 223-33.

214. Watson, D.E., *Contouring: A Guide to the Analysis and Display of Spatial Data*. Tarrytown, NY: Pergamon (Elsevier Science, Inc.), 1992.

215. Webb, S., Combatting cancer in the third millennium – the contribution of medical physics. *Phys Med*, 2008, 24(2), 42-8.

216. Webb, S. and Nahum, A.E., A model for calculating tumour control probability in radiotherapy including the effects of inhomogeneous distributions of dose and clonogenic cell density. *Phys Med Biol*, 1993, 38(6), 653-66.

217. Welsh, J.S., Lock, M., Harari, P.M., Tome, W.A., Fowler, J., Mackie, T.R., Ritter, M., Kapatoes, J., Forrest, L., Chappell, R., Paliwal, B., and Mehta, M.P., Clinical implementation of adaptive helical tomotherapy: a unique approach to image-guided intensity modulated radiotherapy. *Technol Cancer Res Treat*, 2006, 5(5), 465-79.

218. Wiezorek, T., Brachwitz, T., Georg, D., Blank, E., Fotina, I., Habl, G., Kretschmer, M., Lutters, G., Salz, H., Schubert, K., Wagner, D., and Wendt, T.G., Rotational IMRT techniques compared to fixed gantry IMRT and tomotherapy: multi-institutional planning study for head-and-neck cases. *Radiat Oncol*, 2011, 6, 20.

219. Withers, H.R., Biological aspects of conformal therapy. *Acta Oncol*, 2000, 39(5), 569-77.

220. Wu, B., Ricchetti, F., Sanguineti, G., Kazhdan, M., Simari, P., Chuang, M., Taylor, R., Jacques, R., and McNutt, T., Patient geometry-driven information retrieval for IMRT treatment plan quality control. *Med Phys*, 2009, 36(12), 5497-505.

221. Wu, Q.J., Yin, F.F., McMahon, R., Zhu, X., and Das, S.K., Similarities between static and rotational intensity-modulated plans. *Phys Med Biol*, 2010, 55(1), 33-43

222. Wu, V.W., Law, M.Y., Star-Lack, J., Cheung, F.W., and Ling, C.C., Technologies of image guidance and the development of advanced linear accelerator systems for radiotherapy. *Front Radiat Ther Oncol*, 2011, 43, 132-64.

223. Yakovlev, A., Comments on the distribution of clonogens in irradiated tumors. *Radiat Res*, 1993, 134(1), 117-22.

224. Yang, D., Brame, S., El Naga, I., Aditya, A., Wu, Y., Goddu, S.M., Mutic, S., Deasy, J.O., and Low, D.A., Technical note: DIRART – a software suite for deformable image registration and adaptive radiotherapy research. *Med Phys*, 2011, 38(1), 67-77.

225. Yu, C.X., Li, X.A., Ma, L., Chen, D., Naqvi, S., Shepard, D., Sarfaraz, M., Holmes, T.W., Suntharalingam, M., and Mansfield, C.M., Clinical implementation of intensity-modulated arc therapy. *Int J Radiat Oncol Biol Phys*, 2002, 53(2), 453-63.

226. Zaider, M. and Minerbo, G.N., Tumour control probability: a formulation applicable to any temporal protocol of dose delivery. *Phys Med Biol*, 2000, 45(2), 279-93.

227. Zhang, G., Jiang, Z., Shepard, D., Earl, M., and Yu, C., Effect of beamlet step-size on IMRT plan quality. *Med Phys*, 2005, 32(11), 3448-54.

228. Zhang, J., Sun, J., Yang, Y., Chen, X., Meng, L., and Lian, P., Web-based electronic patient records for collaborative medical applications. *Comput Med Imaging Graph*, 2005, 29(2-3), 115-24.

229. Zhang, X., Li, X., Quan, E.M., Pan, X., and Li, Y., A methodology for automatic intensity-modulated radiation treatment planning for lung cancer. *Phys Med Biol*, 2011, 56(13), 3873-93.

230. Zhao, B., Joiner, M.C., Orton, C.G., and Burmeister, J., "SABER": A new software tool for radiotherapy treatment plan evaluation. *Med Phys*, 2010, 37(11), 5586-92.

231. Zheng, X.K., Chen, L.H., Wang, Q.S., and Wu, F.B., Influence of [18F] fluorodeoxyglucose positron emission tomography on salvage treatment decision making for locally persistent nasopharyngeal carcinoma. *Int J Radiat Oncol Biol Phys*, 2006, 65(4), 1020-5.

232. Zhu, X., Ge, Y., Li, T., Thongphiew, D., Yin, F.F., and Wu, Q.J., A planning quality evaluation tool for prostate adaptive IMRT based on machine learning. *Med Phys*, 2011, 38(2), 719-26.

Appendix

Appendix 1. Detailed normalized root-mean-square deviation (NRMSD) results for all organs at risk.

	brainstem		Left Lens		Right Lens		optic chiasm		spinal cord	
Plan	Manual	CAE	Manual	CAE	Manual	CAE	Manual	CAE	Manual	CAE
1	52.31	52.30	2.31	2.29	5.68	5.69	50.58	50.59	40.85	40.82
2	50.82	50.84	3.86	3.88	4.58	4.57	52.48	52.47	43.79	43.76
3	53.70	53.69	4.85	4.87	5.85	5.87	51.74	51.75	41.87	41.89
4	50.13	50.13	3.00	2.98	5.14	5.13	50.50	50.46	44.80	44.77
5	52.10	52.08	0.95	0.94	2.07	2.05	53.69	53.68	43.22	43.20
6	52.94	52.92	2.33	2.32	1.14	1.13	52.66	52.65	40.91	40.90
7	51.21	51.21	2.00	1.98	3.69	3.66	51.03	51.00	41.91	41.89
8	51.64	51.61	1.84	1.84	4.11	4.11	50.93	50.92	40.01	39.97
9	52.63	52.61	4.73	4.69	5.14	5.09	52.45	52.43	41.19	41.18
10	53.56	53.54	4.15	4.14	4.60	4.57	50.41	50.41	41.17	41.16
11	51.46	51.43	5.06	5.04	4.31	4.28	51.82	51.77	39.15	39.14
12	51.99	51.98	0.57	0.57	5.55	5.50	51.53	51.50	38.21	38.18
13	50.76	50.75	4.73	4.72	4.29	4.27	52.82	52.80	43.93	43.92
14	53.13	53.11	5.10	5.07	1.51	1.50	52.91	52.86	43.23	43.20
15	52.01	51.97	2.03	2.02	3.95	3.94	51.31	51.26	41.84	41.81
16	53.47	53.46	2.28	2.27	5.72	5.71	52.90	52.86	44.08	44.04
17	52.97	52.94	0.89	0.89	2.68	2.67	53.41	53.40	40.03	40.02
18	52.83	52.83	4.46	4.42	1.58	1.57	50.29	50.26	40.03	40.01
19	53.64	53.64	5.01	4.97	1.13	1.12	51.77	51.73	41.03	41.00
20	50.09	50.09	1.48	1.47	5.72	5.71	50.27	50.24	41.30	41.27
21	52.34	52.29	2.29	2.27	3.29	3.27	53.42	53.38	39.33	39.30
22	51.16	51.14	0.71	0.70	1.84	1.83	52.58	52.58	42.87	42.85
23	52.46	52.45	4.97	4.93	1.43	1.42	52.86	52.81	42.70	42.69
24	50.06	50.02	3.48	3.47	1.96	1.95	52.68	52.64	39.79	39.79
25	51.91	51.90	5.00	4.96	2.03	2.03	52.84	52.82	39.30	39.27
26	53.47	53.45	5.77	5.72	3.27	3.25	53.61	53.58	41.55	41.51
27	50.12	50.08	5.79	5.78	3.69	3.66	51.09	51.07	40.98	40.98
28	52.83	52.79	2.79	2.77	2.61	2.59	52.32	52.29	43.20	43.20
29	50.15	50.10	3.34	3.33	5.40	5.35	53.39	53.38	41.96	41.93
30	51.09	51.08	3.91	3.90	3.44	3.43	52.08	52.05	42.20	42.20
NRMSD (%)	0.0164		0.010		0.011		0.0258		0.009	

	mandible		left temporal lobe		right temporal lobe		brainstem + 0.3cm	
Plan	**Manual**	**CAE**	**Manual**	**CAE**	**Manual**	**CAE**	**Manual**	**CAE**
1	62.53	62.55	68.53	68.57	66.47	66.51	57.84	57.84
2	65.77	65.78	62.71	62.72	54.42	54.45	55.30	55.30
3	66.26	66.27	55.84	55.85	57.87	57.88	59.70	59.70
4	60.88	60.89	68.21	68.22	59.13	59.13	55.90	55.90
5	60.04	60.06	60.50	60.51	62.15	62.16	55.94	55.94
6	68.57	68.62	60.76	60.77	63.71	63.75	54.41	54.41
7	69.81	69.84	70.82	70.86	58.42	58.43	57.38	57.37
8	60.86	60.86	63.62	63.66	67.79	67.81	56.11	56.11
9	60.53	60.55	60.79	60.81	70.42	70.42	54.95	54.95
10	59.75	59.77	66.52	66.54	62.61	62.65	56.06	56.06
11	61.02	61.04	56.44	56.47	63.36	63.39	57.23	57.23
12	70.38	70.43	57.14	57.18	64.73	64.77	56.10	56.10
13	69.48	69.49	55.48	55.52	69.82	69.87	58.33	58.33
14	70.41	70.45	59.17	59.17	68.03	68.06	59.14	59.14
15	62.54	62.59	69.69	69.70	59.83	59.84	59.31	59.31
16	63.26	63.29	57.70	57.73	51.24	51.28	55.46	55.46
17	62.06	62.08	58.24	58.25	52.19	52.21	59.89	59.88
18	71.30	71.31	54.13	54.14	54.71	54.72	59.55	59.54
19	61.40	61.41	58.10	58.14	63.48	63.51	58.16	58.15
20	58.47	58.51	58.89	58.90	52.31	52.32	57.47	57.47
21	65.22	65.24	53.71	53.71	63.78	63.78	55.77	55.77
22	63.16	63.16	53.18	53.19	66.62	66.66	57.10	57.10
23	60.48	60.53	62.77	62.78	58.26	58.30	57.49	57.49
24	67.05	67.08	66.76	66.81	54.02	54.06	56.41	56.41
25	69.72	69.74	61.49	61.51	66.95	66.96	59.33	59.33
26	71.65	71.66	58.11	58.15	60.17	60.21	58.03	58.03
27	69.32	69.36	54.22	54.23	57.53	57.54	57.77	57.77
28	65.38	65.40	63.59	63.61	70.07	70.09	55.73	55.73
29	63.02	63.02	71.62	71.66	60.37	60.40	57.08	57.08
30	70.31	70.35	70.22	70.26	60.53	60.58	56.76	56.76
NRMSD (%)	0.006		0.004		0.005		0.000	

	right optic nerve+ 0.3cm		left eye		left eye + 0.3cm		right eye	
Plan	**Manual**	**CAE**	**Manual**	**CAE**	**Manual**	**CAE**	**Manual**	**CAE**
1	57.04	57.05	50.82	50.82	57.80	57.82	51.89	51.91
2	57.24	57.24	50.47	50.47	55.54	55.55	51.80	51.82
3	55.97	55.97	51.25	51.27	55.53	55.53	50.63	50.64
4	55.39	55.40	51.06	51.08	55.33	55.32	53.32	53.34
5	57.52	57.53	51.05	51.06	54.25	54.27	53.54	53.56
6	57.70	57.71	52.29	52.31	54.34	54.35	50.47	50.47
7	59.06	59.07	50.96	50.98	55.32	55.33	53.51	53.51
8	56.18	56.18	50.51	50.53	54.19	54.20	51.09	51.10
9	58.76	58.78	53.51	53.52	56.64	56.64	53.31	53.32
10	55.78	55.80	52.56	52.58	55.13	55.15	51.82	51.82
11	55.16	55.18	50.39	50.41	59.31	59.32	51.70	51.70
12	58.84	58.84	53.66	53.67	54.65	54.67	51.47	51.47
13	59.22	59.22	52.10	52.10	57.69	57.69	51.60	51.61
14	54.20	54.20	50.38	50.39	58.81	58.82	53.09	53.09
15	55.70	55.71	53.32	53.33	59.23	59.25	50.66	50.67
16	58.27	58.29	50.30	50.30	57.85	57.86	51.72	51.73
17	55.77	55.78	53.01	53.01	56.93	56.95	53.11	53.11
18	58.95	58.96	53.66	53.66	57.03	57.03	50.56	50.56
19	58.92	58.92	51.23	51.23	57.41	57.43	53.00	53.02
20	57.31	57.33	50.24	50.25	56.93	56.94	52.47	52.47
21	59.79	59.79	50.79	50.81	59.33	59.33	53.38	53.40
22	58.32	58.33	52.90	52.90	54.21	54.23	51.63	51.65
23	56.39	56.41	51.29	51.29	55.25	55.25	50.12	50.13
24	58.52	58.53	50.17	50.19	54.03	54.05	50.82	50.82
25	57.95	57.95	51.14	51.16	55.12	55.13	53.16	53.17
26	56.41	56.41	52.93	52.93	58.26	58.26	50.87	50.88
27	58.02	58.04	51.61	51.61	57.80	57.81	50.75	50.75
28	54.39	54.41	53.01	53.03	55.91	55.93	50.99	50.99
29	54.89	54.89	51.02	51.03	55.49	55.51	52.32	52.32
30	55.55	55.56	53.54	53.55	58.26	58.27	50.19	50.19
NRMSD (%)	0.003		0.005		0.004		0.004	

	right eye + 0.3cm		spinal cord + 0.5cm		left parotid		right parotid	
Plan	**Manual**	**CAE**	**Manual**	**CAE**	**Manual**	**CAE**	**Manual**	**CAE**
1	55.00	55.01	47.58	47.59	34.90	34.90	49.18	49.19
2	54.25	54.25	44.44	44.44	24.60	24.60	36.53	36.53
3	57.40	57.41	42.66	42.67	36.83	36.83	30.02	30.03
4	55.81	55.81	45.44	45.44	49.25	49.28	24.16	24.16
5	56.48	56.49	49.80	49.81	41.29	41.31	39.57	39.57
6	56.33	56.34	44.21	44.22	26.31	26.32	24.76	24.77
7	59.67	59.68	43.46	43.46	40.05	40.05	33.12	33.12
8	55.75	55.77	45.77	45.77	33.91	33.93	39.31	39.31
9	58.32	58.34	44.07	44.09	24.32	24.34	24.03	24.03
10	55.82	55.83	48.86	48.88	48.83	48.87	25.91	25.92
11	54.73	54.73	43.30	43.31	25.97	25.98	48.67	48.70
12	57.40	57.40	44.73	44.73	29.10	29.12	30.31	30.31
13	54.26	54.28	48.14	48.16	41.55	41.55	42.10	42.10
14	54.28	54.29	44.56	44.57	39.99	40.02	26.54	26.54
15	59.47	59.47	43.34	43.34	32.09	32.11	36.37	36.39
16	58.37	58.38	45.68	45.68	34.48	34.49	44.19	44.19
17	55.15	55.17	48.09	48.11	44.54	44.54	47.87	47.89
18	57.12	57.14	48.88	48.90	42.89	42.89	39.33	39.34
19	56.64	56.65	49.05	49.06	48.93	48.95	28.63	28.64
20	59.53	59.54	42.13	42.14	30.87	30.88	25.23	25.24
21	59.39	59.39	44.82	44.84	28.25	28.27	25.40	25.42
22	54.02	54.03	44.79	44.81	39.32	39.35	36.77	36.79
23	55.59	55.61	42.65	42.66	33.09	33.11	44.04	44.06
24	56.56	56.57	48.30	48.31	36.54	36.56	38.49	38.52
25	59.59	59.60	49.42	49.43	38.56	38.56	31.87	31.88
26	58.12	58.13	44.97	44.98	36.19	36.20	29.94	29.94
27	59.76	59.76	48.93	48.95	30.73	30.73	28.19	28.20
28	56.08	56.08	43.03	43.04	25.38	25.40	47.17	47.20
29	57.65	57.66	47.54	47.54	47.40	47.42	37.36	37.39
30	55.00	55.01	48.28	48.28	31.19	31.21	48.51	48.54
NRMSD (%)	0.002		0.002		0.001		0.001	

	left auditory structure		right auditory structure		larynx	
Plan	**Manual**	**CAE**	**Manual**	**CAE**	**Manual**	**CAE**
1	43.79	43.81	54.51	54.51	51.10	51.12
2	46.74	46.78	47.54	47.56	42.13	42.14
3	46.59	46.60	48.90	48.92	42.86	42.89
4	50.49	50.49	46.23	46.25	49.66	49.66
5	53.48	53.49	48.74	48.74	51.37	51.38
6	45.79	45.82	52.14	52.15	50.21	50.25
7	44.45	44.48	45.03	45.07	47.26	47.27
8	48.07	48.08	41.46	41.46	42.34	42.36
9	45.52	45.52	44.65	44.67	52.90	52.93
10	47.90	47.91	42.56	42.58	40.66	40.69
11	46.42	46.42	40.88	40.91	54.82	54.85
12	46.40	46.40	40.93	40.94	43.45	43.45
13	54.53	54.56	40.37	40.38	40.03	40.04
14	51.13	51.17	54.15	54.16	45.55	45.56
15	54.19	54.22	47.49	47.50	49.57	49.60
16	40.12	40.15	44.69	44.69	46.58	46.61
17	40.04	40.07	48.20	48.20	42.56	42.57
18	41.13	41.15	47.83	47.83	43.11	43.13
19	45.59	45.60	43.42	43.44	41.73	41.75
20	52.62	52.66	54.41	54.45	46.51	46.53
21	46.70	46.74	53.33	53.35	40.78	40.78
22	40.93	40.94	47.97	47.99	49.87	49.88
23	52.92	52.95	44.20	44.21	47.67	47.67
24	48.39	48.43	48.52	48.55	50.86	50.86
25	51.11	51.14	41.37	41.38	42.48	42.49
26	54.35	54.38	49.11	49.11	53.23	53.27
27	54.71	54.75	54.12	54.12	50.95	50.97
28	50.23	50.26	40.39	40.41	44.71	44.74
29	46.38	46.40	54.52	54.52	54.92	54.92
30	42.14	42.15	53.70	53.70	49.97	50.01
NRMSD (%)	0.005		0.002		0.003	